UNIVERSITY COLLEGE LONDON

Magnetic Properties of the Intermetallic Compounds PrNiSn and NdNiSn

A Thesis submitted to
the University of London
in the Faculty of Science
for the Degree
of Doctor of Philosophy

By

Eamonn Beirne

September 2002

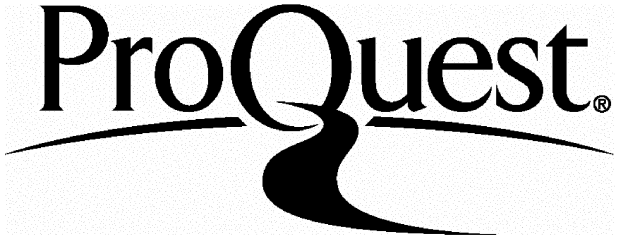

Acknowledgements

I must begin by thanking my supervisor, Keith McEwen, and Stan Zochowski my second supervisor. I am very grateful for the help, advice and encouragement from both of them over the course of my PhD. I also have to thank Mark Ellerby for all the help in the laboratory, on experiments, during physics discussions, and as a friend.

I am grateful to the Rutherford Appleton Laboratory (RAL), the Institut Laue-Langevin (ILL) and the Hahn Meitner Institute (HMI) for the use of their facilities and beam time. In particular I would like to mention Klaus Habicht, Martin Bull, Bachir Ouladdiaf, Rob Bewley and Roger Eccleston. A special thank you goes to Devashibhai Adroja for all his help with my inelastic experiment analysis and discussions.

Thank you to everyone else at UCL, especially Jon Allen for his program and help with my work, Simon Armitage for going through exactly the same steps as myself and being a good friend, Shusaku Hayama for all his help, and Helen Thompson, Louise Affleck, Jonathan Wasse, Chris Howard, and Gary Martin for all their support and friendship. And to all for keeping life at UCL interesting, and my pool skills up to a decent level.

Thank you also to Tony Harker for his support, and Neal Skipper for the use of his laptop.

A huge Thank You to my parents for all their support, both financially and otherwise, not only over the past 4 years, but throughout my 8 years at University. And of course my sister Geraldine, who always makes me laugh.

And lastly, but by no means least, Hayley. She was my principal editor, personal motivator, and the best coffee break partner a man can ask for.

Abstract

Inelastic neutron scattering has been used to determine the crystalline electric field (CEF) excitations in the intermetallic compound PrNiSn. Polycrystalline samples of PrNiSn are found to have 7 excitations up to 30 meV, with strong low-lying modes at 2.0, 3.5, and 5.1 meV. The site symmetry of Pr^{3+} in this system is such that the degeneracy of the 9 levels in the J = 4 ground state multiplet is removed completely by the crystal field. From fitting this data, it is clear that the ground state is a singlet that couples to each of the other 8 excited states. The wavefunctions of the levels are determined and a level scheme proposed for this material.

Inelastic scattering results are also presented for a single crystal of PrNiSn. The dispersion of the low-lying E = 3.5 meV CEF excitation is documented, showing 4 distinct modes corresponding to the 4 Pr ions in the unit cell.

Susceptibility and magnetisation results for PrNiSn and NdNiSn are presented. From these measurements it is clear that the PrNiSn does not order magnetically down to 2K, whereas NdNiSn has an antiferromagnetic transition at T_N = 3.1K. Resistivity measurements on PrNiSn also show no evidence of a magnetic transition, but there are gradient changes at around 4.5K and 12K. This corresponds to a local maximum at 12K and local minimum at 4.5K along the b-axis in this compound. Measurements on single crystals of these compounds show strong anisotropy in both cases, attributed to CEF effects. From the proposed CEF level scheme, the bulk properties such as the susceptibility can be modelled.

Neutron powder diffraction measurements on both PrNiSn and NdNiSn confirm that there is no magnetic transition down to 1.6K in PrNiSn, and T_N is confirmed for NdNiSn. Structural Rietveld fitting confirms the room temperature orthorhombic structure in both systems down to low temperature, but the magnetic structure of NdNiSn can not be determined. This is due to the magnetic peaks below T_N doubling up, indicating a very complicated magnetic structure. It is clear a diffraction experiment on a single crystal of NdNiSn is needed to resolve the magnetic structure.

Finally, these results and conclusions are put into context by comparisons with other RNiSn compounds, notably CeNiSn, and with UNiSn.

Contents

Acknowledgements iii

Abstract iv

List of Figures viii

List of Tables xvii

1. Introduction

1.1. Magnetism. 1

1.2. Crystalline electric field. 2

1.3. Experimental techniques. 4

1.3.1. SQUID. 4

1.3.2. Resistance and dilatometry measurements. 5

1.3.3. Neutron Scattering Instruments. 7

1.3.3.1. HET. 9

1.3.3.2. V2 FLEX. 10

1.3.3.3. D20. 11

1.4. Sample preparation. 12

2. UNiSn & CeNiSn

2.1. UNiSn. 15

2.1.1. Inelastic neutron scattering (HET, ISIS). 18

2.1.2. Field dependent neutron powder diffraction (ROTAX, ISIS). 21

2.2. CeNiSn. 24

3. Literature Survey

3.1. RNiSn 33

3.2. PrTSn & NdTSn, and PrNiX & NdNiX 38

4. PrNiSn

4.1. Neutron powder diffraction. 41

4.1.1. Experimental procedure. 42

4.1.2. Results. 43

4.2. Polycrystalline powder inelastic neutron scattering (HET, ISIS). 47

4.2.1. Experimental procedure. 47

4.2.2. CEF excitation results. 47

4.2.2.1. CEF peak fitting summary. 59

4.2.3. Intermultiplet results. 62

4.2.4. FOCUS fit. 64

4.2.5. FOCUS analysis and results. 64

4.2.5.1. Analysis from YbNiSn CEF parameters. 66

4.2.5.2. Analysis based on the point charge model and molecular field theory. 70

4.2.6. Conclusion. 74

4.3. Single crystal inelastic neutron scattering. 75

4.3.1. Experimental procedure. 75

4.3.2. Results at T = 6 K. 76

4.3.2.1. [00q] 76

4.3.2.2. [q00] 82

4.3.3. Results at T = 2 K. 87

4.3.4. Further Investigation at T = 2 K 90

4.3.5. Conclusions 91

4.4. Magnetic susceptibility and magnetisation. 92

4.4.1. Polycrystalline results. 93

4.4.2. Single crystal results. 94

4.5. Resistivity. 100

4.6. Magnetic Susceptibility Calculation 101

4.6.1. Method 102

5. NdNiSn

5.1. Neutron powder diffraction. 107

5.1.1. Experimental procedure 108

5.1.2. Results 108

5.2. Polycrystalline powder inelastic neutron scattering (HET, ISIS). 113

5.2.1. Experimental procedure. 113

5.2.2. CEF excitation results. 113

5.3. Susceptibility and magnetisation. 123

5.3.1. Polycrystalline results. 123

5.3.2. Single crystal results. 125

5.3.2.1. Magnetic susceptibility. 125

5.3.2.1.1. Low temperature magnetic susceptibility. 127

5.3.2.2. Magnetisation. 128

6. Conclusions and Further work

6.1. Summary 132

6.2. Further Work on PrNiSn and NdNiSn 135

6.3. Further Work in General 137

References 138

List of Figures

1. Chapter 1

1.1. Schematic of a simple dc SQUID.

1.2. The raising and lowering of the sample through the sensor coil loop induces a current measured by the SQUID.

1.3. Schematic of the Capacitance cell used in dialometry and magnetoresistance experiments.

1.4. Pin layout for resistivity measurement.

1.5. Schematic of a typical inelastic chopper spectrometer, such as HET at ISIS.

1.6. Schematic of V2 FLEX, the triple axis spectrometer at HMI, Berlin.

1.7. Experimental set up of the D20 instrument at ILL, France.

1.8. The PrNiSn single crystal, mounted on a goniometer, just before the SQUID sample is cut.

2. Chapter 2

2.1. MgAgAs crystalline structure of UNiSn, the arrows indicating type I antiferromagnetic state with single **k**, alongside a plot showing the tetragonal splitting below T_N.

2.2. $\rho(T)$ curve for UNiSn.

2.3. Specific heat, magnetisation and resistivity change with temperature for UNiSn.

2.4. Crystal field level scheme, proposed by Aoki *et al,* assuming the U^{4+} ion has a $5f^2$ configuration, developed from specific heat and magnetic susceptibility measurements.

2.5. Raw HET data for UNiSn showing the 10meV excitation, using an incident energy of 20meV. ThNiSn is also shown, clearly demonstrating the excitation is magnetic in origin.

2.6. Lorentzian fit of the $E_i \sim 10$meV excitation taken at HET, ISIS.

2.7. Diffraction data for UNiSn at T = 5K & 65K.

2.8. Ratio of magnetic peaks to crystalline peaks taken from diffraction data, fitted to an inverse exponential equation to determine T_N.
2.9. The magnetic field dependence of the magnetic peaks from 0T to 7T.
2.10. The orthorhombic TiNiSi-type structure of CeNiSn
2.11. Electrical resistivity v T for single crystal CeNiSn (a) and the low temperature part on a larger scale (b).
2.12. Magnetic susceptibility v T for single crystal CeNiSn
2.13. Inelastic neutron scattering data for Q = (0, k, 0,), with k = 2, 2.5 and 4 clearly visible are the low-lying phonon peaks below 30 meV (a). The high energy results are enlarged in (b) which shows the broad peak at 40 meV.
2.14. Inelastic neutron scattering data for Q = (0, 0, l,), with k = 3.2, 4 and 6 clearly visible are the low-lying phonon peaks below 30 meV (a). The high energy results are enlarged in (b) which shows the broad peak at 40 meV.
2.15. Inelastic neutron scattering data for Q = (0, 2, 2,) and (0, 4, 4). Clearly visible are the low-lying phonon peaks below 30 meV (a). The high energy results are enlarged in (b) which shows the broad peak at 40 meV.

3. Chapter 3

3.1. Temperature dependence of the magnetisation of NdNiSn measured in an applied field of 0.05 T, where T_N is indicated by the arrow. The inset shows the field dependence at 2 K of the magnetisation.
3.2. The magnetisation curves along the **a**, **b** and **c** axes for the single crystals of DyNiSn and TbNiSn at T = 1.6 K.
3.3. The dependence of the Neél temperature as a deGeens function for RNiSn, scaled to GdNiSn.
3.4. Neutron diffraction patterns of PrPdSn at (a) 5 k paramagnetic phase and (b) 1.5 K magnetic phase. The inset to (b) depicts the temperature dependence of the (0 ½ ½) peak.

3.5. Neutron diffraction patterns of NdPdSn at (a) 5 k paramagnetic phase and (b) 1.5 K magnetic phase. The inset to (b) depicts the temperature dependence of the magnetic (000) and (011) peaks.

4. Chapter 4

4.1. PrNiSn shown in the TiNiSi-type structure configuration, with the different atoms indicated.

4.2. 1.7 K powder diffraction pattern with Rietveld refinement obtained using FullProf98.

4.3. 35 K powder diffraction pattern with Rietveld refinement obtained using FullProf98.

4.4. Comparison of the difference plots between the 1.7 K & 6 K data and the 6 K & 35 K data.

4.5. Inelastic neutron scattering on powder LaNiSn with E_i = 23 meV at T = 10 K. The graphs show the raw data for both 2.5 and 4m bank, with the estimated phonon background from the high angle detector banks.

4.6. Inelastic neutron scattering on powder LaNiSn with E_i = 60 meV at T = 10 K. The graphs show the raw data for both 2.5 and 4m bank, with the estimated phonon background from the high angle detector banks.

4.7. Inelastic neutron scattering on powder PrNiSn with E_i = 23 meV at T = 10 K and 25 K.

4.8. Gaussian fit to the 5 lowest excitations seen in the 23 meV incident energy spectrum at 10 K and 25 K. The parameters for each fit are shown in the inserts. The fits are to the raw 2.5m bank data minus the phonon contribution estimated from w8/5.

4.9. 4m bank data showing the lowest 5 excitations seen with incident energy E_i = 23 meV at 10 K.

4.10. Inelastic neutron scattering from the 2.5 bank, with incident energy of 35 meV at T = 10 K and 100 K.

4.11. Gaussian fit to the 3 highest excitations seen in the 2.5m and 4m banks E_i = 35 meV spectra minus the phonon contribution. The parameters for each peak are shown in the inserts.
4.12. The 3 excitations seen in the 35 meV spectrum are also clearly evident at 60 meV incident energy.
4.13. Gaussian fit to the 3 highest excitations seen in the 2m 60meV incident energy spectrum. The parameters for each peak are shown in the insert.
4.14. The 4m bank corrected data for the E_i = 60 meV, which suggests there are 3 excitations visible.
4.15. Resolution curves for the incident energies of 23 meV and 60 meV. These curves allow us to compare CEF excitation widths to the instrument resolution.
4.16. Inelastic scattering with an incident energy of 800 meV shows 2 intermultiplet transitions and a well-known anomalous peak at 367 meV. The lines are fit to Gaussian function, with the parameters given in the inset to the first spectrum.
4.17. CEF FOCUS fit to the 23 meV energy transfer data at T = 10 K. There are 5 CEF excitations shown, at approximately 2, 3.5, 5, 7.5 and 17.5 meV. The inset shows the low energy data in detail.
4.18. Proposed level scheme as predicted by a FOCUS fit to the 23 meV HET data of PrNiSn at 10 K. The arrows indicate possible transitions, with the thickness of each arrow an indication to the relative intensities of each transition. These are detailed in the table. Also shown is the proposed wavefunctions for each CEF level.
4.19. Using the calculated CEF parameters at T = 10 K, the fit to the T = 25K data is shown. The only parameters allowed to change are related to the elastic peak and background.
4.20. CEF FOCUS fit to the 23 meV energy transfer data at T = 10 K using the molecular field method. The inset shows the energy data in detail.

4.21. Proposed level scheme as predicted by a FOCUS fit to the 23 meV HET data of PrNiSn at T = 10 K. The arrows indicate possible transitions, with the thickness of each arrow an indication to the relative intensities of each transition. These are detailed in the table. Also shown is the proposed wavefunctions for each CEF level.

4.22. Using the calculated CEF parameters at T = 10 K, the fit to the T = 25K data is shown. The only parameters allowed to change are related to the elastic peak and background.

4.23. PrNiSn single crystal mounted on the **a*-c*** face, perpendicular to the **b** axis. The crystal is attached to the mount with a resin based hardener. Scattering from the adhesive is prevented by wrapping the base of the crystal with vanadium, as shown. The principal axes are demonstrated.

4.24. Inelastic scattering of T = 6 K for the wave vector (001). The lines are fits to Gaussian functions. Each point is taken over a counting time of approximately 8 minutes.

4.25. Inelastic scattering at T = 6 K for a series of wave vectors between (001) and (003). Each data s offset by 70 counts (for 1E6 monitor counts) for clarity and the lines are fits to Gaussian functions.

4.26. Dispersion of the two modes around 3.5 meV, between (001) and (003). The lines represent a fit to the functions described in the text.

4.27. Inelastic scattering at T = 6 K for the wave vectors (001) and (003). Each excitation is fitted with a Gaussian function.

4.28. Inelastic scattering at T = 6 K for the wave vector (100). Note the 2.4 meV mode seen at (001) is barely evident and the 3.5 meV mode has shifted slightly to 3.75 meV. The 0.5 meV mode is also still evident.

4.29. Inelastic scattering at T = 6 K for a series of wave vectors between (100) and (300). Each set is offset by 100 counts (1E6 monitor counts) for clarity and the lines are fits to Gaussian functions.

4.30. Dispersion of the 2 (q00) modes around 3.75 meV. Note the lower mode fits to the equation specified in the text, but the upper mode shows a different form to the upper mode along (q00). The blue line is a fit to the data, and the yellow line, a theoretical curve, both of which are specified in the text.

4.31. Inelastic scattering at T = 6 K for the wave vector (2.2 0 0). The graph shows 2 fits to the same data. The top curve is a single Gaussian fit (offset by 100 counts), allowing all the available parameters to freely move. The bottom curve is the results of a 2 Gaussian fit, where the second Gaussian has been fixed at an energy of 3.54 meV as predicted by the theoretical curve given in figure 4.30.

4.32. Inelastic scattering at T = 2 K & 6 K for the wave vector (001).

4.33. Temperature dependency of the Positron and Area of the 0.5 meV (T = 6 K) mode at the wave vector (001). There appears to be a transition of some description at T = 4.5 K.

4.34. Data taken at the wave vectors (001) and (003) at T = 2 K.

4.35. Inelastic scattering at T = 2K and 6 K for the wave vector (001). Each excitation is fitted with a Gaussian function, and the fit parameters described in the inserts.

4.36. Inelastic scattering at T = 1.6 K for the wave vectors (001) and (003). Each excitation is fitted with a Gaussian function and the resulting parameters shown in the inserts.

4.37. The inverse susceptibility per formula unit of polycrystalline PrNiSn, showing Curie Weiss behaviour down to 40 K. The inset demonstrates the susceptibility at low temperature, illustrating the change in gradient seen at T = 4.5 K.

4.38. Low temperature susceptibility per formula unit for each principle axis in PrNiSn. Note the c-axis data have been multiplied by 2 for clarity. The local maximum at T = 12 K and minimum at T = 4.5 K along the b-axis is clearly illustrated. Each measurement is in an applied field of H = 300 O_e.

4.39. Inverse magnetic susceptibility per formula unit for each principle axis. Curie-Weiss behaviour is evident above T = 50 K.
4.40. b-axis susceptibility at 3 different applied fields: 0.03 T, 1 T & 2 T. Note the reversibility at H = 0.03 T.
4.41. The field dependence along a-axis at T = 2 K, 5 K and 11 K for PrNiSn
4.42. The field dependence along b-axis at T = 2 K, 5 K and 11 K for PrNiSn
4.43. The field dependence along c-axis at T = 2 K, 5 K and 11 K for PrNiSn
4.44. The resistivity v temperature for polycrystalline PrNiSn, taken at UCL and Spain. The insert shows the low temperature resistivity and the derivative with temperature.
4.45. The proposed level schemes compared to the excitation data from HET. Note only 8 levels are shown for method 2. The 9th level is at 47.9 meV, but is not shown so that the lower levels are clearer.
4.46. The experimental data for the single crystal PrNiSn and the CEF calculated inverse magnetic susceptibility for Method 1 and Method 2, between the temperatures 2 K – 300 K, at the applied field H = 300 G.
4.47. The experimental data for the single crystal PrNiSn and the CEF calculated inverse magnetic susceptibility for Method 1 and Method 2, between the temperatures 2 K – 100 K, at the applied field H = 300 G.

5. Chapter 5

5.1. T = 30 K powder diffraction with Rietveld refinement obtained using Fullprof98.
5.2. T = 2 K powder diffraction pattern with Rietveld refinement obtained using Fullprof98. The first picture shows the fit and difference plot. The second picture depicts low angle data showing antiferromagnetic peaks that have not been fitted.
5.3. Difference plot between the antiferromagnetic regime (T=2 K) and the paramagnetic phase (T= 8 K). Note that all the peaks consist of 2 or more individual peaks.
5.4. A plot of T v A for the antiferromagnetic peak at $\theta = 58^{\circ}$.

5.5. Proposed CEF level from the fits **[Figures 4,5,7,-11]** to the T = 4.5 K and E_i = 23, 25 and 60 meV.

5.6. Gaussian fit to the proposed 3 lowest CEF peaks seen in the 2.5m and 4m banks Ei = 23 meV, T = 2 K spectra, minus the phonon contribution. Aside from these 3 CEF peaks the blue arrows indicate other possible excitations. Parameters for each peak are shown in the inserts.

5.7. Gaussian fit to the proposed 3 lowest CEF peaks seen in the 2.5m and 4m banks Ei = 23 meV, T = 4.5 K spectra, minus the phonon contribution. Again other peaks are clearly visible (dotted blue fit). Parameters for each peak are shown in the inserts.

5.8. Gaussian fit to the proposed 3 lowest CEF peaks seen in the 2.5m and 4m banks Ei = 23 meV, T = 25 K spectra, minus the phonon contribution. Dotted blue lines again show other smaller peaks. Parameters for each peak are shown in the inserts.

5.9. Gaussian fit to the proposed 3 lowest CEF peaks seen in the 2.5m and 4m banks Ei = 35 meV, T = 4.5 K spectra, minus the phonon contribution. Dotted blue lines again show the other smaller peaks, but they are now harder to fit. Parameters for each peak are shown in the inserts.

5.10. Gaussian fit to the proposed 3 lowest CEF peaks seen in the 2.5m and 4m banks Ei = 60 meV, T = 4.5 K spectra, minus the phonon contribution. Note that the smaller peaks seen at lower incident energies cannot be seen. Parameters for each peak are shown in the inserts.

5.11. Temperature dependence of the inverse susceptibility of polycrystalline NdNiSn in an applied field of 300G, with the red line a Curie Weiss fit down to 50 K. the inset shows the low temperature susceptibility at the same applied field. The AF transition is clearly visible at T_N = 3.0 K.

5.12. Field dependence of the magnetisation of polycrystalline NdNiSn at 4 different temperatures. The inset shows the M v H data at T = 2 K (in AF state) more clearly.

5.13. Temperature dependence of the inverse susceptibility of NdNiSn single crystal, measured along the main axis in a field of 300G. The inset shows the low temperature susceptibility for each axis at the same applied field. The AF transition is clearly visible at T_N = 3.0 K in all axes.
5.14. The transition T_N = 3 K at different applied fields along the **a** axis.
5.15. The transition T_N = 3 K at different applied fields along the **b** axis.
5.16. Field dependence of the magnetisation of polycrystalline NdNiSn along the **a** axis at 4 different temperatures. The inset shows the M v H data at T = 2 K (in AF state) more clearly, with the red arrow indicating the possible transition at 1.5 K.
5.17. Field dependence of the magnetisation of a polycrystalline NdNiSn along the **b** axis at 4 different temperatures. In the AF state (T = 2 K) a spin flop transition is seen at 0.85 T.
5.18. Field dependence of the magnetisation of polycrystalline NdNiSn along the **c** axis at 4 different temperatures. Note the small change between 4 T and 5 T that causes the 2 K data to cross the 3 K.
5.19. Field dependence of the magnetisation of polycrystalline NdNiSn along each principle axis at T = 2 K(AF state). The spin-flip transition in the **b**-axis (o.85 T), and the steps at 1.5 T (a-axis) and 4.5 T (c-axis) are clearly seen.

6. Chapter 6

6.1. The proposed level scheme and wave functions for each level for PrNiSn proposed by Method 2.
6.2. The proposed level scheme for NdNiSn, with approximate intensities depicted by arrow width. The scheme is proposed from the excitations observed in the HET experiment.
6.3. Proposed specific heat v temperature for PrNiSn, using the Fortran program written by J. Allen, to be published. The y axis is in arbitrary units.

List of Tables

1. Chapter 1

1.1. Amounts of raw materials used in the melting of polycrystalline PrNiSn in the arc furnace. Note the extra Sn added to account for any mass loss during the melt.

2. Chapter 2

3. Chapter 3

3.1. Crystal data and some of the properties of the RNiSn alloys.

3.2. Crystal data and some properties of the PrTSn and NdTSn alloys.

3.3. Crystal data and some properties of the PrNiX and NdNiX alloys.

4. Chapter 4

4.1. Lattice parameters and atomic positions for PrNiSn obtained from Rietveld fitting to the Pnma space group (TiNiSi-type structure).

4.2. Specifications of the data runs for PrNiSn on HET, showing the incident energy E_i, μAhrs, chopper frequency and the average temperature of the CCR head and sample.

4.3. The average angle of the detector bank workspaces on HET at the time of the experiment.

4.4. Energy, FWHM and Area of the peak calculated from the Gaussian fits to the excitations in the E_i = 23, 35 and 60 meV 2m and 4m bank data at T = 10 K.

4.5. Experimental energies (meV) of intermultiplet transitions for the Pr free ion, Pr metal and PrNiSn.

4.6. Stevens factors for rare earth ions.

4.7. CEF parameters in meV, for T = 10 K, produced by the fitting program FOCUS, using the analysis from YbNiSn parameter method.

4.8. CEF parameters in meV, for T = 10 K, produced by the fitting program FOCUS, using the analysis of the single crystal magnetic susceptibility data based on the point charge model and molecular field theory.
4.9. Comparisons of each method and the weighted fits to the raw data.
4.10. Area under the curve, FWHM and energy positions for the 2 modes around 3.5 meV along the (00q) direction, fitted to Gaussian curves.
4.11. Dispersion coefficients of the equations detailed in the text.
4.12. Intensity, FWHM and energy positions for the 2 modes around 3.75 meV along the (q00) direction, fitted to Gaussian curves.
4.13. Dispersion coefficients of the equations detailed in the text for (q00).
4.14. Summary of the values for the Curie Weiss temperatures and effective moments, calculated from the susceptibility data.

5. Chapter 5

5.1. Lattice Parameters and atomic positions for NdNiSn obtained from the Rietveld fitting to the Pnma space group (TiNiSi-type structure)
5.2. Specifications of the data runs for NdNiSn on HET, showing the incident energy E_i, μAhrs, chopper frequency, and the average temperature of the CCR head and sample.
5.3. Gaussian fits to the 3 excitations observed in the E_i = 23 meV spectra, at T = 2 K, 4.5 K and 25 K. Also shown is the average difference between each temperature of the peak centres for each of the excitations.
5.4. Peak positions, widths and intensities, for each excitation for each of the scans, at T = 4.5 K and the average energy position of the CEF excitation at this temperature.
5.5. Summary of the values for the Curie Weiss temperatures and effective moments calculated from the magnetic susceptibility data.
5.6. The susceptibility at Tn for different fields along the 3 principal axes, taken from the data shown in Figure 5.10, 5.11 and 5.12.

CHAPTER 1

Introduction

1.1 Magnetism

In all the compounds studied, you can picture the system as a group of atoms, each with their own magnetic moment, interacting with each other and the surrounding electronic potential. These interactions give rise to the diversity of magnetic properties seen in such systems. In rare earth and actinide metals the magnetism has its origins in the angular momentum of the $4f$ electrons in the atoms. Because the $4f$ electron wavefunctions do not extend beyond the $5d$ and $6s$ states, the $4f$ electrons are localised for the majority of the rare earth elements. Intrinsic to understanding the magnetic properties in these elements and compounds is the magnetic exchange between these isolated magnetic ions. This is commonly described by the RKKY interaction, a model proposed by Ruderman and Kittel (1954), Kasuya (1956) and Yosida (1957) to explain these effects. The model relies on the magnetisation of the conduction ions in the vicinity of the magnetic ion, which in turn is perceived by the next ion. Therefore the $4f$ electron spins are coupled by the induced magnetisation in the conduction electrons. Thus, the Hamiltonian of such as system is given by

$$H = -\frac{1}{2}\sum_{ij} J_{ij} J_i \cdot J_j + g_J \mu_B B \cdot \sum_i J_i + H_{CEF}$$

Equation 1.1

with the summations covering all magnetic ions within the system. The first term is the Heisenberg exchange due to the RKKY interaction, where $\mathbf{J_{ii}}$ is the Fourier transform of the q dependent exchange integral **J(q)**. The second term is the Zeeman interaction of each ion, and the final term is the Crystal Field Hamiltonian, detailed below.

1.2 The Crystalline Electric Field.

A magnetic ion surrounded by a periodic metal lattice experiences an electrostatic potential due to the regular array of neighbouring charges. This is called the crystalline electric field, which raises the degeneracy of the ionic groundstate J multiplets and induces a splitting of the order 10-30meV in the rare earths. The splitting in transition metals is much greater. These levels can be seen in the guise of crystal field excitations, which are the modes due to transitions between the states. In the rare earths, the CEF effect is smaller than that of the spin-orbit effect, allowing us treat the effect as a small perturbation of the free-ion Hamiltonian. Essentially the perturbation produced by the CEF is the interaction of the unpaired electronic charges within the magnetic ion and the electronic charges a distance **R** away:

$$v_{cf}(\mathbf{r}) = \int \frac{q\rho(\mathbf{r})}{|\mathbf{r}-\mathbf{R}|} d\mathbf{R}$$

Equation 1.2

where $\rho(\mathbf{R})$ is the charge density of the surrounding electrons and nuclei. The sum of these interactions can be reduced with a higher order of symmetry around the ion. Therefore, as the site symmetry is reduced, the number of potential terms within the expansion increases to fully describe the perturbation. Hence any calculation of the crystal field perturbation becomes more complicated for complex structures.

The CEF potential matrix elements are proportional to those of operator equivalents, thus we can write the CEF part of Equation 1.1 as

$$H_{\mathrm{cf}} = \sum_i \sum_{lm} A_l^m \alpha_l \langle r^l \rangle \left(\frac{2l+1}{4\pi} \right)^{1/2} \tilde{O}_{lm}(\mathbf{J}_i) = \sum_i \sum_{lm} B_l^m O_l^m(\mathbf{J}_i),$$

Equation 1.3

in which the B_l^m are referred to as the crystal field parameters. As can be seen, B_l^m is also equivalent to $A_l^m \langle r^l \rangle \theta_l^m$ in which the A_l^m are also sometimes called the crystal field parameters, the expectation value $<r^l>$ is the average radius over the $4f$ electron states, and θ_n is a multiplicative factor calculated using the *Stevens factors* α_l and spherical harmonics.

The crystal field parameters may be calculated from the charge distribution in the metal, but in practice the determination is difficult. This is due to the fact that the charge density around the ion is hard to determine accurately and the approximations of the electronic structures in metals tend to be inadequate for this purpose. It is therefore necessary to resort to basic methods such as the point-charge model where an adjustable charge is placed on the lattice points.

It is possible however to determine the parameters from experiment such as specific heat, magnetic susceptibility and inelastic neutron scattering, especially on single crystals where the anisotropy due to the crystal field is observed clearly. For systems with orthorhombic symmetry, such as the RNiSn series, the Hamiltonian is expressed in the form

$$H_{cef} = B_2^0 O_2^0 + B_2^2 O_2^2 + B_4^0 O_4^2 + B_4^2 O_4^2 + B_4^4 O_4^4 + B_6^0 O_6^0 + B_6^2 O_6^2 + B_6^4 O_6^4 + B_6^6 O_6^6$$

Equation 1.4

Determination of these CEF parameters from experimental data is a non-trivial task, so a good starting point is needed. Using the known CEF parameters for one compound (i.e. CeNiSn, YbNiSn), it is possible to estimate starting numbers for similar systems (PrNiSn). This procedure is detailed in section 4.2.5.

1.3 Experimental Techniques.

1.3.1 Superconducting Quantum Interference Device (SQUID) magnetometer

Susceptibility and magnetisation studies have been made with a Quantum Design SQUID magnetometer on both polycrystalline and single crystal samples. The magnetic moment of the sample is measured by producing an output voltage proportional to the current induced by moving the sample through the centre of two sense coils.

Flux changes in a superconducting loop with two weak lines produce oscillatory variations in the supercurrent. The SQUID is a practical circuit that measures these variations to quantitatively determine the strength of the applied field. It is more accurate to call such a device a dc SQUID since it measures a slowly changing applied field. A schematic of a SQUID is shown in Figure 1.1, where the current change through the weak links is detected as a voltage change across the pair of links and then amplified by a step-up transformer. Coupling to the sample is via a second order gradiometer coil, which suppresses stray field effects and stray field gradients. Figure 1.2 shows how the sample is raised and lowered to produce the fluctuations in the SQUID.

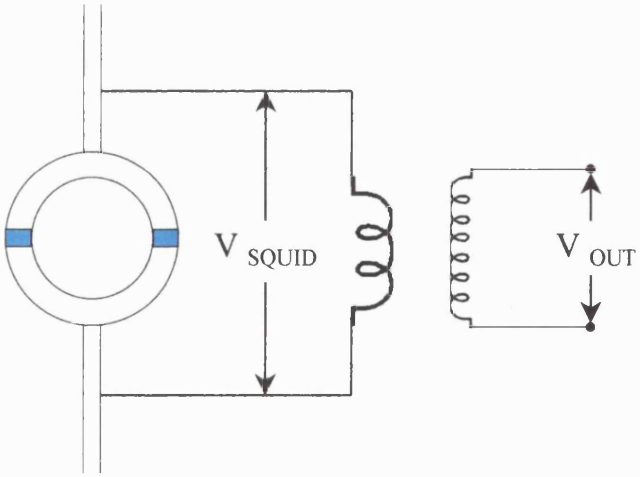

Figure 1.1: Schematic of a simple dc SQUID. The blue shaded areas show the weak links within the superconducting coil.

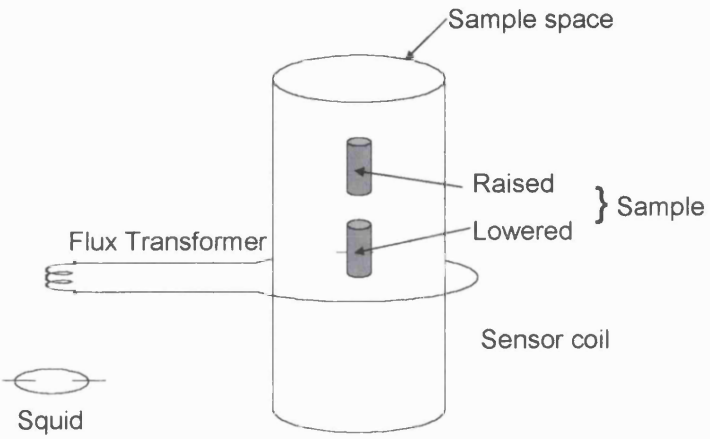

Figure 1.2: The raising and lowering of the sample through the sensor coil loop induces a current measured by the SQUID.

1.3.2 Resistance and Dilatometry measurements

Both the resistivity and the dilatometry measurements were carried out using the same Oxford Instruments Cryostat, capable of obtaining temperatures down to T = 1.7 K and an applied field of H = 7 T. The low temperature was achieved by pumping on the sample space as helium is introduced to the space by means of a needle valve. By pumping against the needle valve, the vapour pressure is reduced as is the temperature of the helium. This can be done in one of two ways; single shot, where the insert pumping pot is filled with helium, the needle valve closed and the helium pumped upon to reduce its pressure and therefore its temperature, or continuous shot, where the needle valve is cracked open with the pump running. The temperature is controlled by maintaining the pumping pressure.

Figure 1.3 depicts the dilatometry cell used in the cryostat. It consists of two plates, the top plate is fixed in position with a guard ring, and insulated by a thin layer of mylar and epoxy resin, whilst the bottom plate (also insulated) is attached to the top plate by two copper / beryllium foil springs.

The sample is mounted on a pedestal and screwed into position with the top of the sample pushing up against the bottom plate. As the sample increases/decreases in size, the bottom plate moves up / down in relation to the top plate. Two connections run from the top and bottom plates to a high precision capacitance bridge, allowing the change in capacitance with temperature (and therefore the expansion of the sample) to be measured.

The sample is mounted by setting the sample in a small blob of silver paint. This ensures that the sample is not strained by setting it in a rigid glue. Sometimes it is necessary to aid the mounting by adding a small amount of G.E. varnish to one corner, especially if the onset of magnetic ordering non-parallel to the field caused the sample to tilt. Note that dilatometry measurements can only be made in the direction of the applied field.

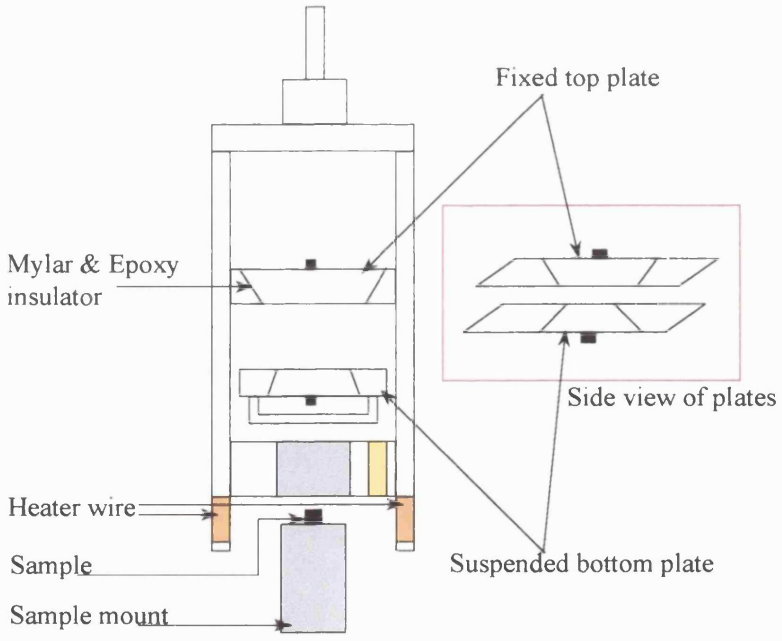

Figure 1.3: Schematic of the capacitance cell used in dilatometry and magnetostriction experiments.

Resistivity measurements were made using a 4 pin connection cell. The sample is mounted onto a flat copper cell, and 4 connections to the sample made using spot welded gold wires [Figure 1.4]. The whole cell is then wrapped in PTFE tape, to protect the sample and bind all the connections so that no contact is made to the dewer. The current to the sample is controlled by a Keithley 220 Programmable Current source, and the voltage across the sample measured by a Keithley 182 Sensitive digital voltmeter. The resistance of the sample may be determined, and from this the resistivity may be calculated from $R = \rho (l/A)$.

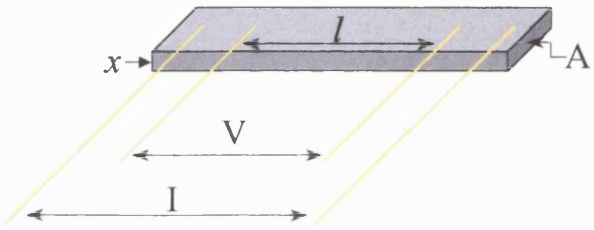

Figure 1.4: Pin layout for a resistivity measurement.

1.3.3 Neutron scattering instruments

Neutron scattering is a powerful tool for investigating the various properties of matter. This is chiefly because of 4 reasons. Firstly, the neutron mass results in the de Broglie wavelength of thermal neutrons being of the order of interatomic distances in liquids and solids. This can be used to determine the structure of the sample by interference effects. Due to the neutron also having no charge, it may penetrate further into the atom, close to the nuclei because there is no Coulomb barrier to overcome. Neutrons are therefore scattered by nuclear forces, the scattering length for some nuclides being very large. This is especially useful when the nuclide in question weakly scatters X-rays, but has a large scattering length for neutrons, such as hydrogen.

Thirdly, the neutron has a magnetic moment, which means that the neutrons will interact with unpaired electrons in a magnetic ion. Due to this effect, it is possible to determine the structure of electron spins and the density distribution of unpaired electrons.

Lastly, the energy of thermal neutrons is of the same order as the majority of excitations in solids and liquids. Because of this, when the neutron is scattered by the creation or annihilation of an excitation within a system, the change in energy of the neutron is a large fraction of the initial neutron energy. Thus it is relatively easy to observe excitations accurately.

When carrying out a neutron scattering experiment, you are essentially measuring the partial differential cross-section,

$$\frac{d^2\sigma}{d\Omega dE_f} = \frac{\left(\begin{array}{l}\text{number of neutrons scattered per second into solid angle } d\Omega \text{ in direction } \theta,\phi \\ \text{with final energy between } E_f \text{ and } E_f + dE_f\end{array}\right)}{\Phi d\Omega dE_f}$$

Equation 1.5

where σ is the scattering cross section, and Φ the flux of the incident neutrons. This can be written as

$$\frac{d^2\sigma}{d\Omega dE_f} = \frac{\sigma}{4\pi}\frac{\mathbf{k}_f}{\mathbf{k}_i} NS(\mathbf{Q},\omega)$$

Equation 1.6

where N is the number of nuclei in the scattering system, $S(\mathbf{Q},\omega)$ is the scattering function of the sample, and $\mathbf{k}_f$ and $\mathbf{k}_i$ are the final and incident wave vectors of a neutron. Note that the scattering function is a function of momentum transfer $\mathbf{Q} = \mathbf{k}_i - \mathbf{k}_f$ and energy transfer $\hbar\omega$, and it is this quantity that is measured in an inelastic experiment.

In the case of a diffraction experiment, energy analysis is not needed. Thus the quantity measured is the differential cross section $d\sigma/d\Omega$.

1.3.3.1 HET

HET is an example of a chopper spectrometer, the schematics of which is shown in Figure 1.5, and is housed at ISIS, a pulsed spallation neutron source.

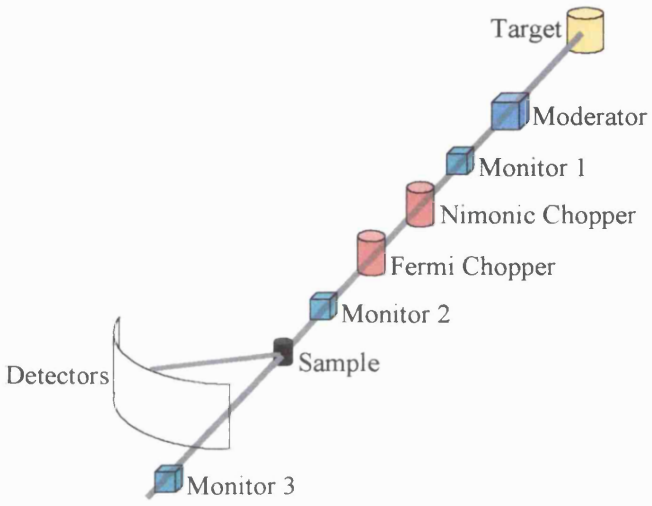

Figure 1.5: Schematic of a typical inelastic chopper spectrometer, such as HET at ISIS.

A proton pulse (frequency of 50 Hz) produced from a synchrotron is bombarded into a heavy metal target to produce a pulse of neutrons. The target at ISIS is tantalum, which, when hit by the protons, is excited into a higher state. The nuclei then decay to the ground state, emitting nucleons, mainly neutrons. Some of these neutrons leave the target, while others trigger further chain reactions within the tantalum. Current production at ISIS is approximately 15 neutrons per high energy proton. As can be seen in Figure 1.5, the emitted neutrons need to be moderated due to their high energy and velocity. Hydrogen is often used, utilising its large scattering cross section to slow the neutrons down to useable energies. Other moderators are methane, and water (the moderator seen by HET).

The Nimonic chopper is there to reduce the background created from the proton beam – target collision. This background is mostly made up of γ's, and the chopper works by effectively closing the beam tube at the moment of impact between the protons and the target.

The Fermi chopper is perhaps the most important apparatus on this kind of spectrometer. Made of highly absorbing thin sheets of boron and interleaved with aluminium (transparent to neutrons), it is housed in an aluminium drum. The drum rotates between 250–600 Hz in phase to the pulse of the neutron beam and at the position that transmits neutrons with the desired energy E_i (and therefore $\mathbf{k}_i$). It is worthwhile to note that the slits are curved to maximise transmission. At several points along the beam tube monitors are located. It is the time-of-flight between monitors 2 & 3 that are used to determine the incident energy.

The samples may be mounted in a variety of environments, such as a Closed Cycle Refrigerator (CCR) or a standard Orange cryostat. Further details of the set up for experiments detailed in this thesis are given in the relevant chapters.

1.3.3.2 V2 Flex

Flex is a triple axis spectrometer based at the Hahn-Meitner-Institut in Berlin, Germany. Although the quantity measured is the same as at HET, the method and principles of the instrument differs extensively. The neutron beam originates from a reactor source as opposed to a pulsed source and a schematic of the spectrometer is shown in Figure 1.6.

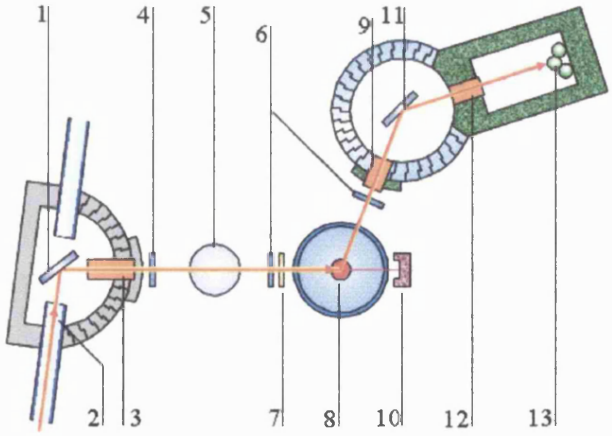

Figure 1.6: Schematic of V2 FLEX, the triple axis spectrometer at HMI, Berlin. 1) Monochromater 2) Neutron guide 3) Collimator 4) Diaphragm 5) Be or PG filter 6) Diaphragm 7) Monitor 8) Sample 9) Collimator 10) Beam stop 11) Analyser 12) Collimator 13) Detector.

The triple axis spectrometer is ideal for single crystal neutron scattering, allowing constant energy and constant **q** scans to be taken. Monochromatic neutrons are selected between the wavelength range 0.17 nm (27 meV) and 0.65 nm (1.9meV) by the vertically focusing monochromator and the horizontal focusing analyser crystal. Thus the orientation of the initial and final wave vectors allows measurements to be taken through (**q**, E) space, with one of these parameters usually fixed. To prevent second order ($\lambda/2$) contamination of the beam, a pyrolytic graphite filter (<0.4 nm) or a Be filter (>0.4 nm) is used. To limit the beam divergence and reduce background, there are 4 horizontal collimators, denoted by the numbers 3, 9 and 12. The fourth is before the beam hits the monochromator. It is the combination of the collimator angles, the monochromator angle and the analyser crystal angle that determines the resolution of the instrument. The set up for the experiment detailed in Chapter 3 is dealt with then.

1.3.3.3 D20

D20 is also based at a reactor source, and is a high-intensity two-axis diffractometer. Although it has variable resolution, its main function is for fast data acquisition such as time-resolved powder diffraction, or for diffraction experiments that require accurate high intensity measurements. Thus, D20 is equipped with a 1600 cell curved position sensitive detector (PSD) filled with a mixture of ^3He (3.1 bars) and CF_4 (0.8 bar).

The wavelength used for the experiments detailed in this thesis was $\lambda = 2.4$ Å, and with a Roots pump attached, we were able to achieve temperature down to almost 1.7K.

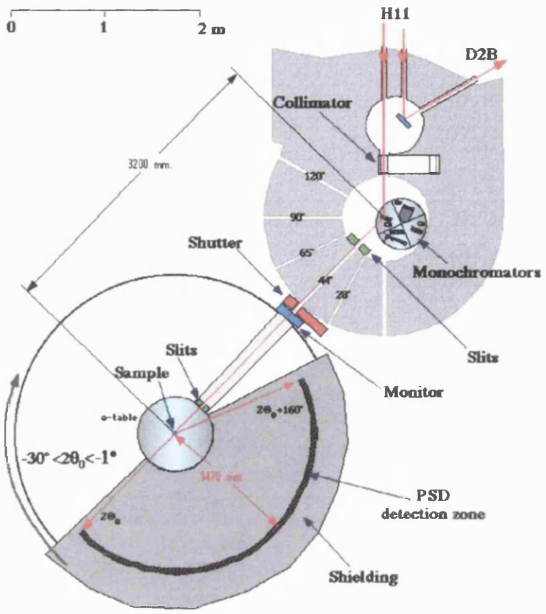

Figure 1.7: Experimental set up of the D20 instrument at ILL, France.

1.4 Sample Preparation

All the polycrystalline samples mentioned in the experimental chapters were manufactured at UCL, using a Bühler Arc furnace. All the materials used were from high purity elements. The U, Pr and Nd from Ames Laboratory (USA) are of 99.9% purity and the Ni and Sn are 99.999% pure, and in wire form. A suitable amount of U or rare earth is cut using a spark eroder, to give the total sample mass needed (Usually 5 or 10g). After cutting, the uranium is cleaned of any oxide layers by etching in a hydrochloric-nitric acid solution. The Pr and Nd are easier to etch, so a more dilute form of the mixture is used. Once the mass of each rare earth is known, the corresponding amount of Ni and Sn are cut. It is important when using Sn to add an excess of this material due to the high vapour pressure Sn has. It is usual to add between 0.1 and 0.5%. After the first melt, it is then easy to re-weigh the button to work out how much Sn has been lost during the melt and add more if necessary. Depending upon how easily the materials melt together, 3 melts are carried out to achieve homogeneity of the sample.

As an example, Table 1.1 shows the masses for each element used in the making of the PrNiSn button used in the powder experiments on HET (ISIS) and D20 (ILL) [Chapters 5.3 & 5.4]. Once the button has been made, it is wrapped in molybdenum foil and annealed in a tube furnace for 1 week at 800°C and ≈ 5 x 10^{-6} Torr. This is to allow any internal stress to relax, allowing further homogenisation to occur.

	Mass (g)
Pr	2.28752
Ni	0.95278
Sn	1.92666
Extra Sn	0.002 (0.100%)
Button mass pre-melt	5.1864
Button mass after melt	5.18454
Mass loss	0.00186

Table 1.1: Amounts of raw materials used in the melting of polycrystalline PrNiSn in the arc furnace. Note the extra Sn added to account for any mass loss during the melt.

The single crystals of PrNiSn and NdNiSn were made at the School of Metallurgy and Materials, University of Birmingham, by Dave Fort. The samples are prepared in the same way as polycrystalline buttons, but a Czochralski Tri-arc furnace is used, under ultra-high vacuum. The principle is the same as a normal arc furnace, but there are 3 arcs focused on the sample button, which has been pre-melted. The sample is mounted on a graphite-cooled copper hearth, which slowly rotates. It is clear to see the button actually rises above the hearth, due to the eddy currents induced in the sample. A probe is dipped into the molten button as it is being rotated. Over a period of a few hours, the probe is slowly raised (approximately 1cm an hour), drawing out a bullet shaped single crystal. Once the crystal has formed at a suitable length, it is allowed to cool before removing it from the furnace.

A picture of the PrNiSn single-crystal, grown by this method, is seen in Figure 1.8, mounted on a goniometer. The inset gives an idea of the bullet size.

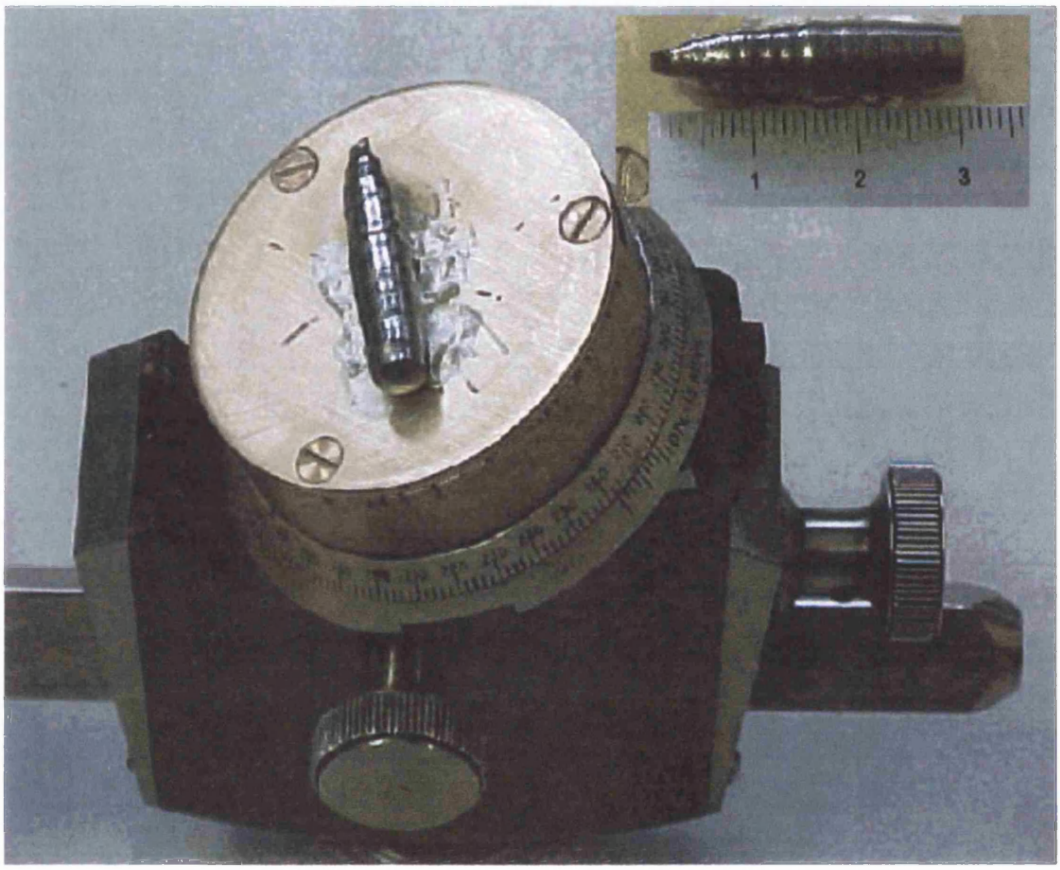

Figure 1.8: The PrNiSn single crystal, mounted on a goniometer, just before the SQUID sample is cut. The inset shows the length of the bullet, which had a mass of 6.7g. The effect of 'pulling' the bullet from the molten button, while being rotated, is evident as rings around the bullet.

CHAPTER 2

UNiSn and CeNiSn

2.1 UNiSn

The intermetallic ternary compound UNiSn has been widely studied due to its interesting and unusual magnetic and transport properties. One of the chief parameters governing the anomalous properties is the actinide-actinide (or Hill) spacing. Hill showed that if $d_{Ac} < 3.5$Å, local moments on the actinides are quenched due to the f-f overlap. He noticed that magnetism predominantly appeared at large d_{Ac} and superconductivity at low separation. For strong overlap of the f wavefunctions, an f-band forms that will not support magnetism. As the separation increases, the overlap, and hence the f-bandwidth, decreases and magnetism is stabilised. In the case of UNiSn, this separation is large: $d_{U-U} = 4.2$ Å.

At $T_N = 45$ K UNiSn has a semiconductor to metal transition. In contrast to other metal-semiconductor transitions triggered by magnetic ordering (i.e. EuO), this transition is first order. Above T_N, the compound is a paramagnetic semiconductor with a gap of $E \sim 0.105 - 0.12$ eV, with a cubic MgAgAs structure (**a** = 6.39Å),

whereas below T_N the compound exhibits an antiferromagnetic metallic behaviour, the AF being of type I and the moment $\mu \sim (1.55\pm0.1)\mu_B$, parallel to the **a** axis. The change in the structure from cubic to tetragonal can clearly be seen in Figure 2.1, alongside the room temperature structure.

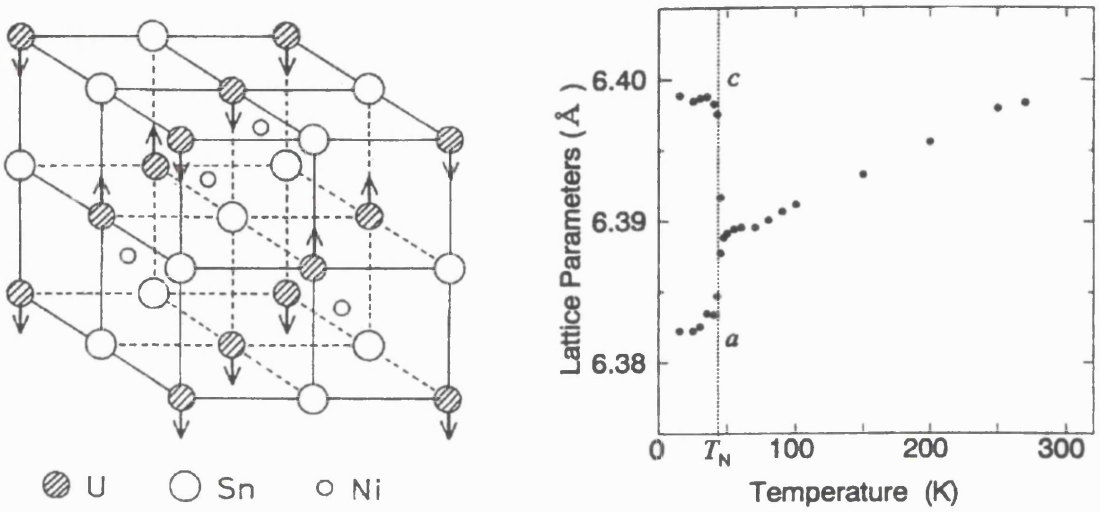

Figure 2.1: MgAgAs crystalline structure of UNiSn, the arrows indicating type I antiferromagnetic state with single **k**, alongside a plot showing the tetragonal splitting below T_N.

The bulk properties of UNiSn are well documented, with the $\rho(T)$, $\chi(T)$ and $\gamma(T)$ all showing typical heavy electron behaviour. Above T = 150K, the magnetisation of UNiSn is Curie – Weiss like, with $\mu_{eff} = 3.08\mu_B$/a.u and $\theta_{CW} = -75$K. Figures 2.2 and 2.3 clearly show this behaviour.

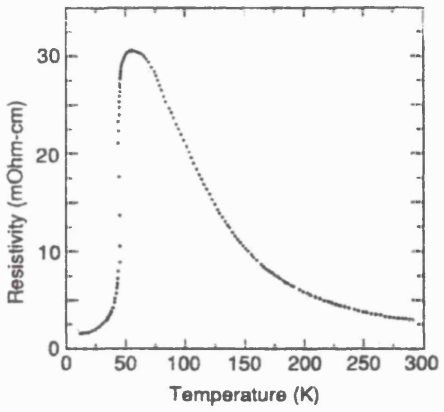

Figure 2.2: ρ(T) curve for UNiSn. The large increase in ρ(T) with decreasing temperature before the sharp decrease, indicating the onset of the metallic phase, is clear. [Yuen *et al* Phys B **171** (1991)].

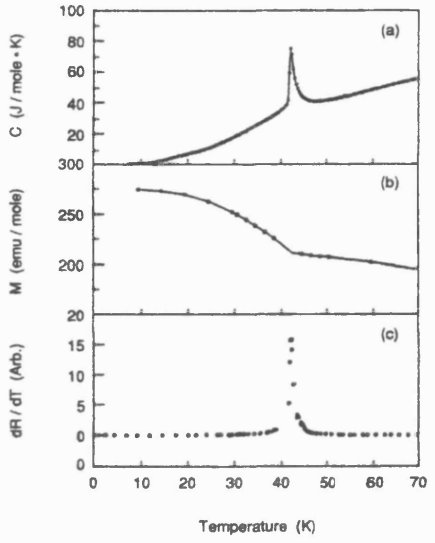

Figure 2.3: Specific heat, magnetisation and resistivity change with temperature for UNiSn. γ(T) has a sharp peak at ~44K corresponding to the AF transition. dρ(T)/dT has a sharp peak at T_N, below which ρ(T) indicates metallic behaviour. [Yuen *et al* Phys B **171** (1991)].

From their studies of these bulk properties, Akazawa *et al* (1996) proposed the existence of a quadrupolar ordered phase below T_N. Due to the U valence of 4^+, the electrons are in a $5f^2$ (J = 4) configuration. The nine fold multiplet is split by the crystal field into a singlet (Γ_1), a doublet (Γ_3) and two triplet states (Γ_4 and Γ_5). After an analysis of the heat capacity and the susceptibility of the system, Aoki *et al* (1993) proposed a crystal field level scheme [Figure 2.4].

Both these proposals lead to some crucial questions. Firstly, is the Aoki level scheme correct? If so, there should be evidence of these crystal field peaks seen in inelastic neutron scattering experiments.

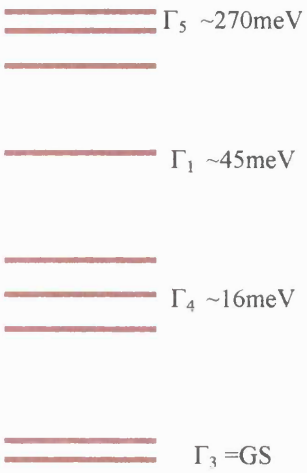

Figure 2.4: Crystal field level scheme proposed by Aoki *et al* [Phys Rev B **47** (1993)], assuming the U^{4+} ion has a $5f^2$ configuration, developed from specific heat and magnetic susceptibility measurements.

Akazawa's proposal leads to the crucial question of the order parameter within the system. Put simply, does the onset of magnetic order drive the quadrupolar order, thereby inducing the structural change and conductivity change, or does the quadrupolar order drive everything else? For a complete understanding of what is happening in this complicated system, we set about two neutron experiments, using the HET and ROTAX spectrometers at ISIS. As an observer on these experiments, I was able to observe the techniques used while developing groundwork for my own studies.

2.1.1 Inelastic experiment on HET at ISIS

The UNiSn and ThNiSn samples for both experiments were prepared by arc melting and annealing for one month at 1000K under vacuum. For the HET experiment, the 40g sample was mounted in a CCR cryostat. ThNiSn was used to estimate the phonon scattering contribution from UNiSn.

The aim of this experiment was to determine the validity of Aoki's level scheme, using the inelastic neutron scattering to search for these magnetic peaks.

Using an incident energy of 345meV we searched for evidence of the Γ_5 CEF level at around 270meV. We immediately saw no evidence of any magnetic scattering at this energy, leading us to the initial conclusion that the proposed level scheme is incorrect. Preliminary runs in the magnetic phase at T = 15K and incident energy E_i = 100meV gave evidence of magnetic scattering at E_i = 30 – 40meV and E_i = 10meV. No more excitations were seen at any energy above the 30 - 40meV band.

Detailed temperature dependence studies of the 10meV excitation were carried out at E_i = 20meV.

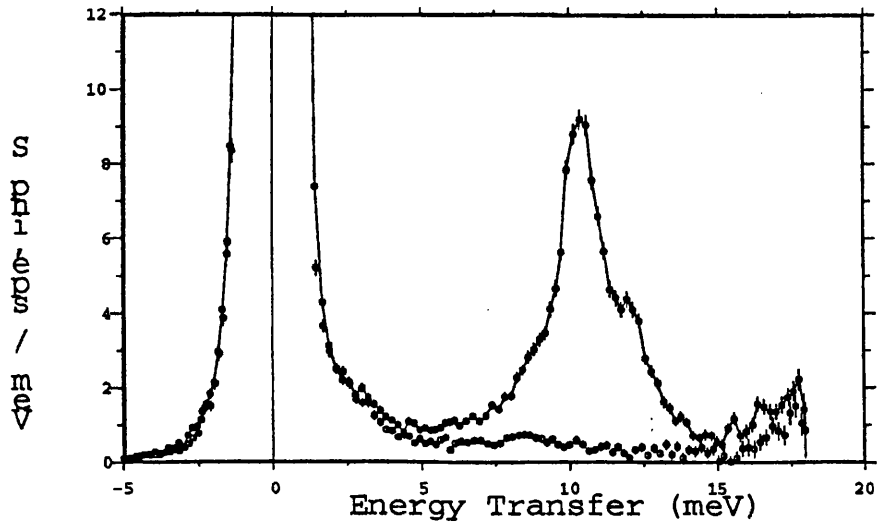

Figure 2.5: Raw HET data for UNiSn showing the 10meV excitation (open circle + line), using an incident energy of 20meV. For comparison, ThNiSn is also shown, clearly demonstrating the excitation is magnetic in origin (open circle).

It is clear from the data that the excitation is magnetic in origin [Figure 2.5] and upon close inspection the excitation is composed of three peaks [Figure 2.6]. Fitting the data to Lorentzian peaks shows three peaks at 8.30 ± 0.35, 10.29 ± 0.06 and 12.04 ± 0.20meV respectively.

As the temperature is increased, towards T_N, the three peaks merge into one, centred at E = 10.79 ± 0.19meV at the transition temperature. Above T_N the peak is still present, but has broadened considerably to a FWHM of 4.48meV at 50K, centred at 11.48 ± 0.28 meV.

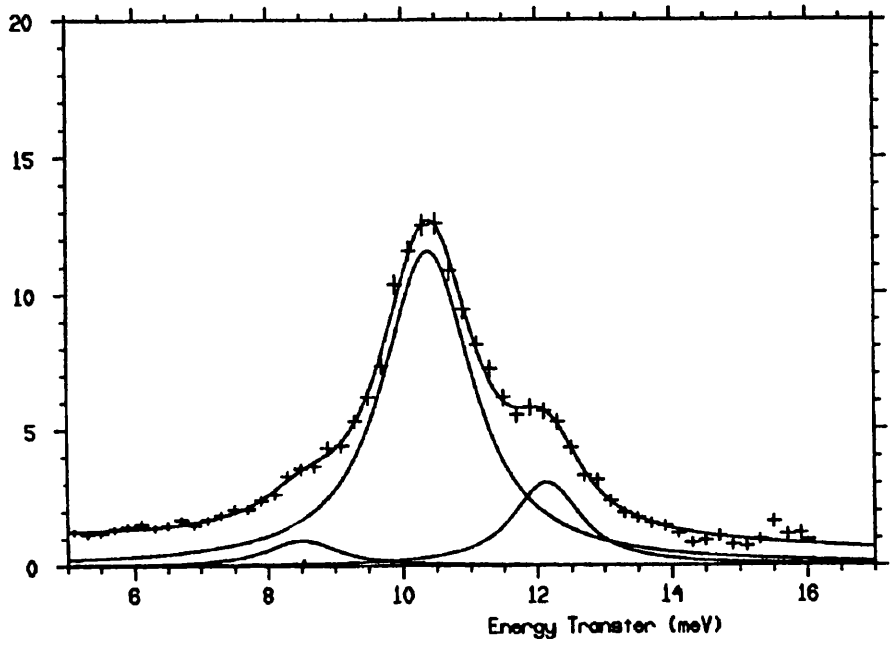

Figure 2.6: Lorenztian fit of the E_i ~ 10meV excitation taken at HET, ISIS. It is clear that three peaks are present, as detailed in the text. Note the intensity axis is in arbitrary units.

From this first experiment showing these magnetic excitations in UNiSn, it is evident that the level scheme proposed by Aoki *et al* is incorrect, the data clearly showing that the upper limit for the CEF energy level scheme is around 40meV. The splitting of the 10meV excitation is also indicative of the tetragonal distortion in the cubic structure, brought about by the strain induced from the formation of quadrupolar order in the ground state. The results from ROTAX bear out this conclusion, as discussed below.

2.1.2 Field dependent diffraction experiment on ROTAX at ISIS.

Akazawa *et al*'s (1996) proposal, that the formation of a quadrupolar ordered phase is the order parameter that drives the transition, was investigated by examining the magnetic field dependence of the superlattice peaks that appear at T_N. The polycrystalline sample was mounted in a 6T vertical field cryomagnet on the ROTAX diffractometer.

After confirming the sample was single phase, comparisons were made between the diffraction patterns at T = 65K and T = 5K. The magnetic (110) and (210) peaks are present in the magnetic phase [Figure 2.7], confirming the data previously published by Yethiraj *et al* (1989) and the tetragonal strain manifests itself in the broadening of the crystalline (200) peak below the transition temperature. Present within the sample is a second phase, $U_3Ni_3Sn_4$, also noted by Yethiraj *et al*. The crystalline peaks for this compound are seen in both Figure 2.7 and Figure 2.9. These are (310) at θ = 2.95 Å, (220) at θ = 3.31 Å, and (211) at θ = 3.82 Å. Calculating the ratio of the magnetic (110) to the crystallographic (111) peak intensities of UNiSn [Figure 2.8], we are able to confirm the transition temperature as $T_N = 45.8 \pm 0.5$K. I feel that it is interesting to note the slight discrepancies between published values for T_N. It appears that the variance of the transition temperature stems from slight differences in the sample preparation, chiefly the annealing temperature and time of annealing.

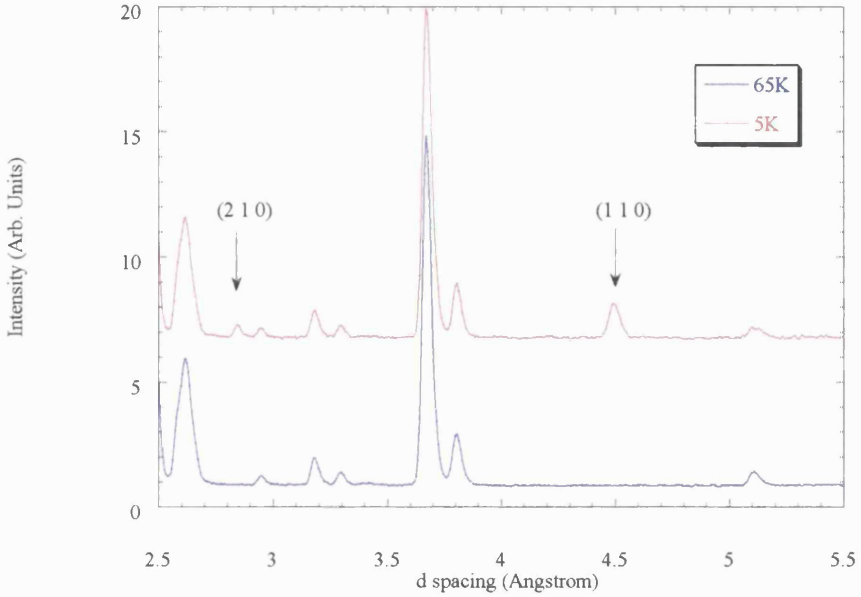

Figure 2.7: Diffraction data for UNiSn at T = 5 K & 65 K. The magnetic (110) & (210) are clearly visible in the ordered phase. The (111) peak of UNiSn is clearly seen at θ = 3.69 Å, and the (200) is observed at θ = 3.19 Å. The observed $U_3Ni_3Sn_4$ crystal peaks are as mentioned in the text.

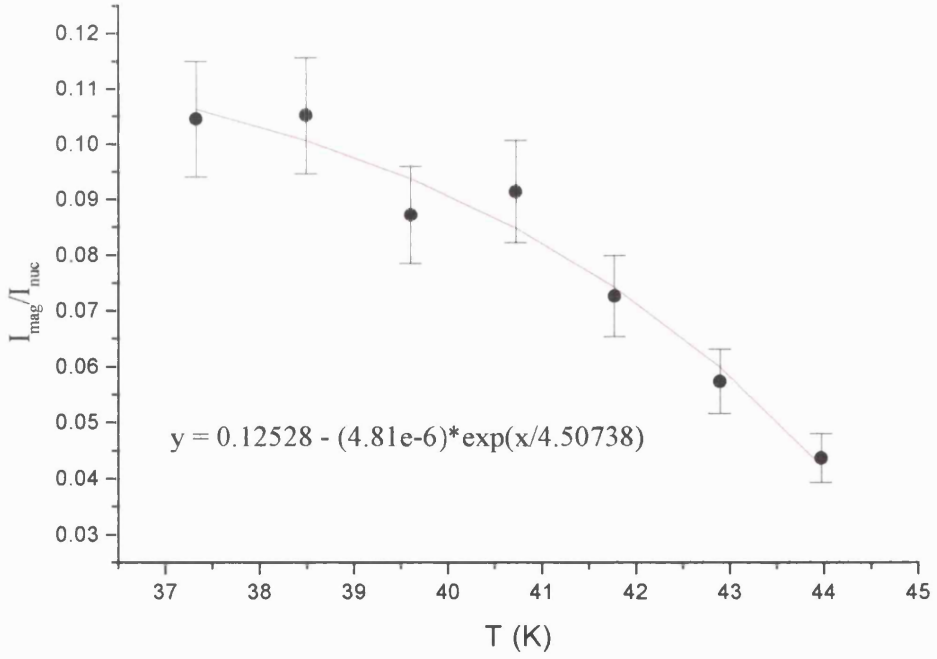

Figure 2.8: Ratio of magnetic peaks to crystalline peaks taken from the diffraction data, fitted to an inverse exponential equation to determine T_N. (See text)

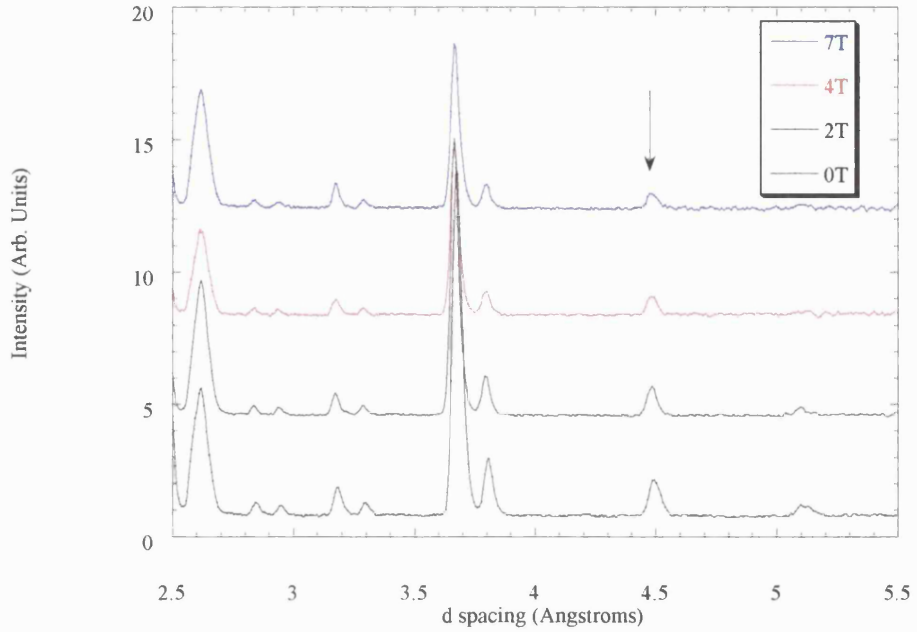

Figure 2.9: The magnetic field dependence of the magnetic peaks from 0 T to 7 T. The (110) is indicated by an arrow.

The magnetic (110) and (210) peaks demonstrate a decrease in intensity as the field is increased, indicating that the ordered moment is decreasing in magnitude with increasing applied field [Figure 2.9]. From bulk measurements carried out by Akazawa *et al* (1999), T_Q, the quadrupolar transition temperature, separates from T_N at an applied field of approximately 5T. Above B = 5T and T_N, UNiSn is a paramagnetic metal with ferroquadrupolar order. Coupled with the data from ROTAX and HET, it is clear that at T_N the antiferromagnetic order splits the CEF ground state, triggering the ferroquadrupolar order. This in turn induces tetragonal strain, seen in the change in lattice constants, all at T_N in zero field.

2.2 CeNiSn

The intermetallic compound CeNiSn has attracted a lot of attention due to its anomalous magnetic and transport properties. Since the discovery that the system has a small pseudogap in the electronic density of state at the Fermi level at low temperature, hundreds of papers have been published in an attempt to understand these properties and the origin of the gap. Like the rest of the RNiSn series, CeNiSn has the TiNiSi-type crystal structure [Figure 2.10, Y. Inada *et al* (1996)]. As noted by Takabatake *et al* (1990a), the structure may be viewed as stacks of Ce sheets parallel to the **bc** plane with two layers of Ni and Sn between. This indicates that CEF effects should play a large role in the origin of the anomalous properties. Anisotropic interactions of the (almost) localised 4*f* electrons and the delocalised conduction electrons are usually reflected in the anisotropic magnetic and transport properties of such as system as CeNiSn.

This hybridisation between the electrons may allow the energy bands near the Fermi level to be very close to the instability for gap formation. But the explanation of how the gap forms is not clear, evidenced by the large amount of material being published on this interesting compound.

Takabatake *et al* (1990a) carried out extensive resistivity measurements on a single crystal of CeNiSn and have determined the size of the psuedogap along each axis: **a** $\approx$ 2.4K, **b** $\approx$ 5.5K and **c** $\approx$ 5K at low temperature (<10K). From their resistivity [Figure 2.11] and magnetic susceptibility [Figure 2.12] measurements, it is clear that CeNiSn also has no magnetic transition down to 11mK.

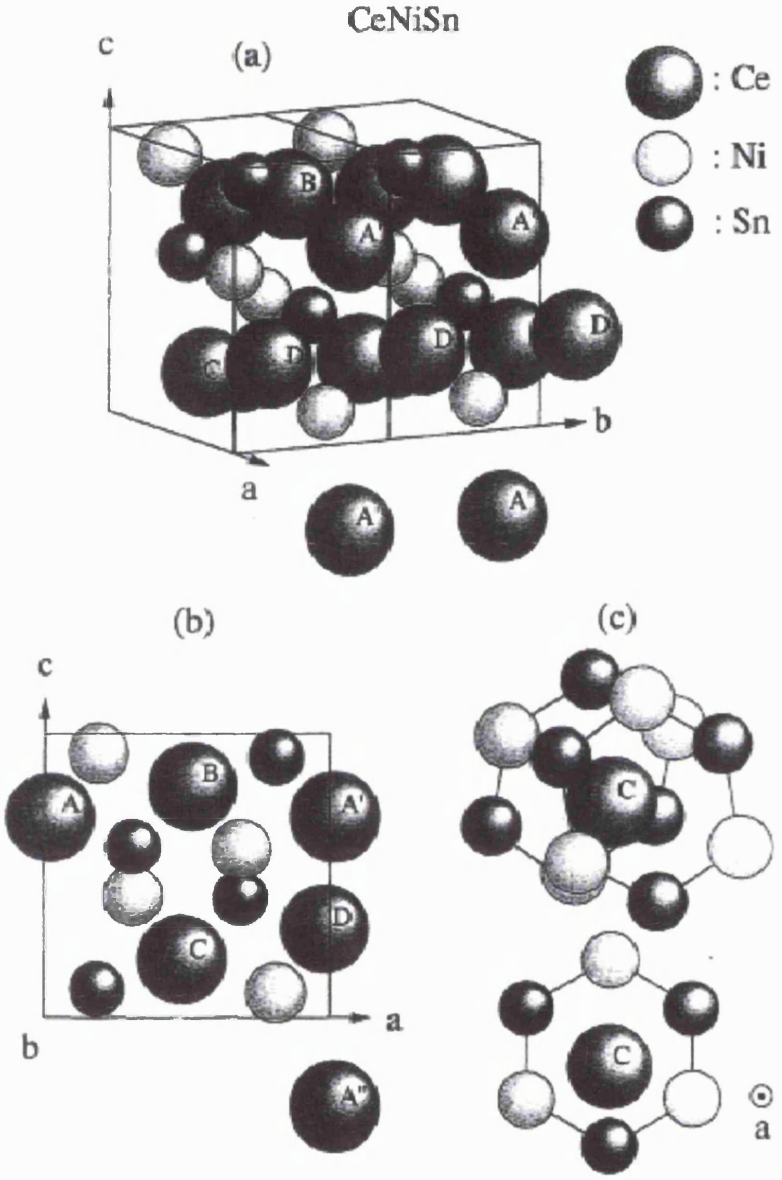

Figure 2.10: The orthorhombic TiNiSi-type structure of CeNiSn [Y. Inada *et al* (1996)].

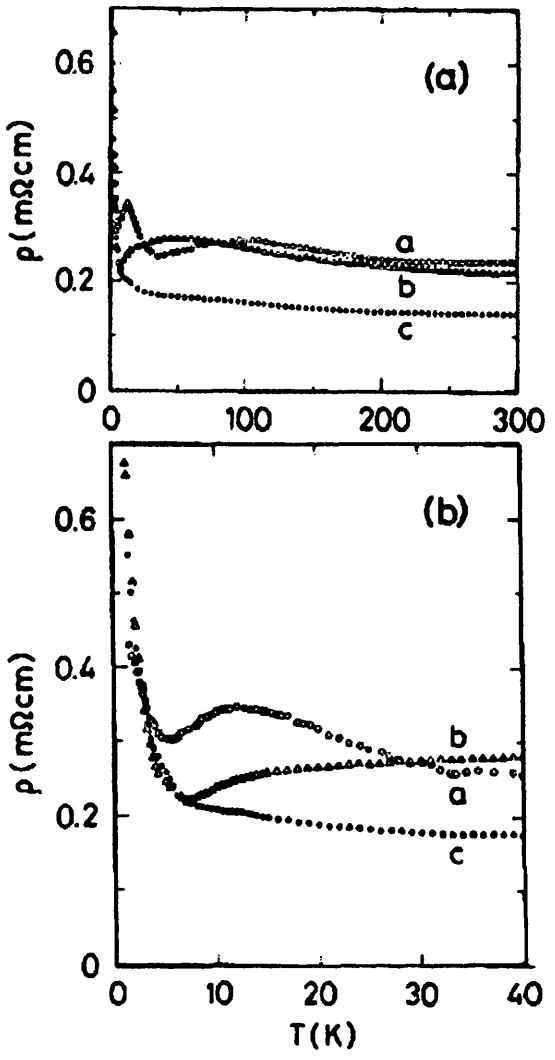

Figure 2.11: a) Electrical resistivity v T for single crystal CeNiSn; b) the low temperature part on a larger scale. [Takabatake *et al* (1990a)]

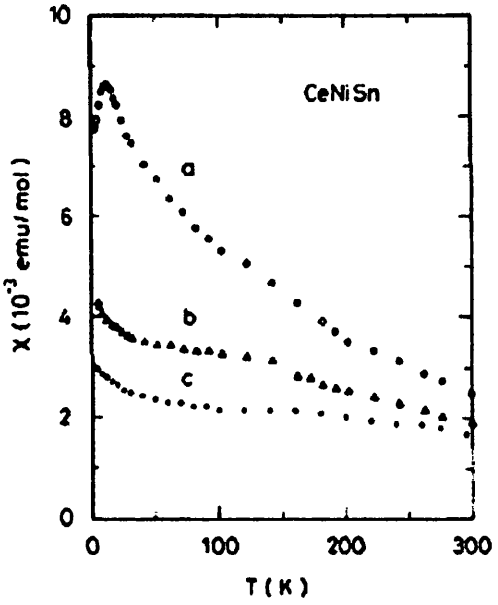

Figure 2.12: Magnetic susceptibility v T for single crystal CeNiSn [Takabatake *et al* (1990a)].

The large upturn seen in these resistivity measurements are not always observed. It is now accepted that the large increase in resistivity at low temperatures which is taken as a signature of the development of a gap, is a direct result of the quality of sample. CeNiSn samples that are better quality have a less-pronounced increase and there is evidence to show that samples with the best quality become metallic at low temperature [Takabatake *et al* (1996)]. It should be noted however, that the electronic specific heat is not sample-dependent. This suggests that the small gap contains some residual density of states.

The crystal field excitations of CeNiSn have also been investigated, in the polycrystalline state [D.T Adroja *et al* (1996)] and single crystal [J-G. Park *et al* (1998)]. Adroja *et al* found that the two well-defined crystal field excitations seen in CePtSn (a localised Ce system), become weaker with Ni doping on the Pt site. For the CePtSn, the two excitations are centred at 23.3 and 35.2 meV with line widths of 3.2 and 4.7 meV respectively, and for Ce $Pt_{0.5}Ni_{0.5}Sn$, the energies are 19.9 and 33.5 meV with line widths of 6.2 and 9.4 meV. The spectrum for CeNiSn shows no clear evidence for two distinct excitations, but rather one broad inelastic peak centred at 33.5 meV with a line width of 15.2 meV.

The absence of well defined crystal field excitations is consistent with the theory that the splitting is quenched as the 4*f*-conduction electron hybridisation increases.

J-G. Park *et al* studied the excitations described above for CeNiSn in a single crystal. Figures 2.13 – 2.15 clearly show several low-lying peaks below 30 meV and a broad peak near 40 meV, at the three wave vectors Q = (0, *k*, 0) [Figure 2.13], Q = (0, 0, *l*) [Figure 2.14] and Q = (0, *k*, *l*) [Figure 2.15]. They determined that the low-lying peaks all grew in intensity with increasing wave vector, apart from the broad peak at 40 meV. This excitation becomes weaker with increasing Q. This suggests that the low-lying peaks arise from phonon excitations, and the broad peak at 40 meV is a magnetic excitation. It is concluded that this 40 meV excitation is due to a crystal field excitation of the Ce^{3+} ion. It is expected, due to the structure and symmetry, that the Ce $4f^1$ state will be split into three doublets. Indeed, as demonstrated above, CePtSn (which has the same structure as CeNiSn) demonstrates this with two excitations seen at 24 meV and 35 meV.

It is postulated that the strengthening hybridisation with the conduction electrons gives rise to the broadening of the CEF excitations. Thus, the 35 meV peak seen in CePtSn is the broad excitation seen in CeNiSn, while the 24 meV excitation has been suppressed and is not visible, especially given the presence of a phonon peak around this energy.

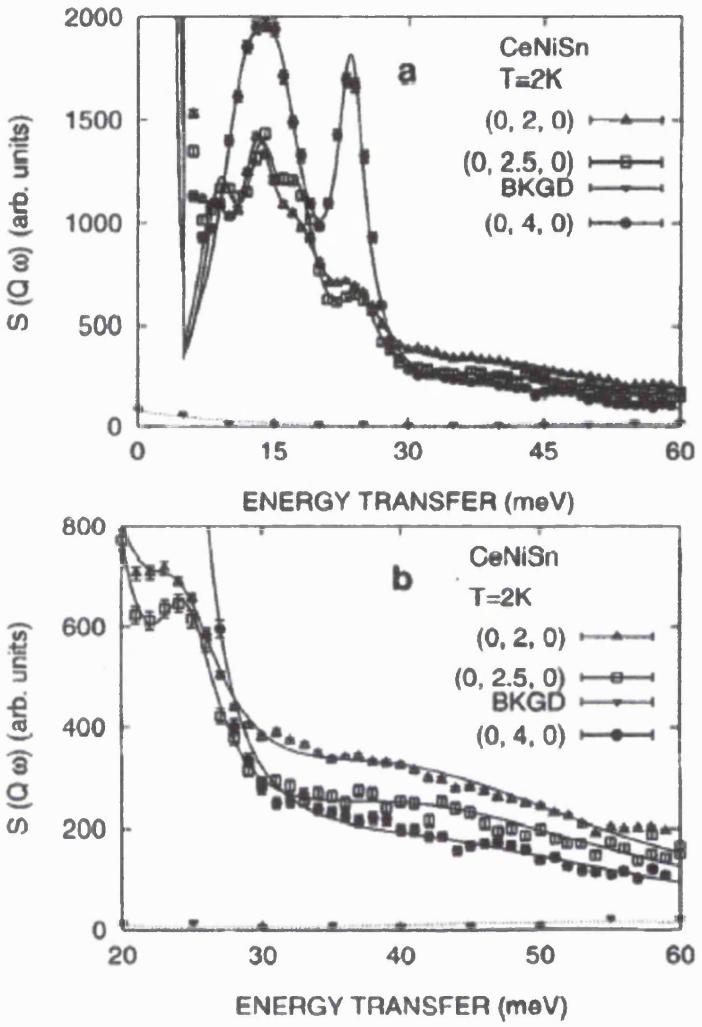

Figure 2.13: a) Inelastic neutron scattering data for Q = (0, *k*, 0), with k = 2, 2.5, and 4. Clearly visible are the low-lying phonon peaks below 30 meV. The high energy results are enlarged in (b), which shows the broad peak at about 40 meV, attributed to a CEF excitation. [Taken from J-G. Park *et al* (1998)].

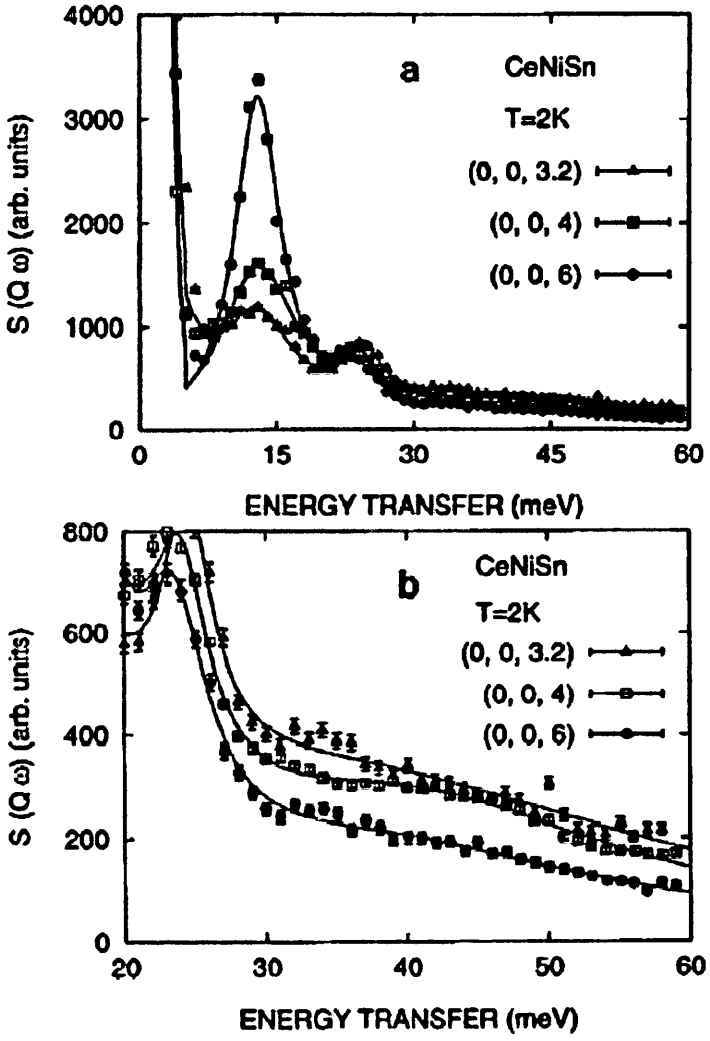

Figure 2.14: a) Inelastic neutron scattering data for Q = (0,0,*l*), with k = 3.2, 4, and 6. Clearly visible are the low-lying phonon peaks below 30 meV. The high energy results are enlarged in (b), which shows the broad peak at about 40 meV, attributed to a CEF excitation. [Taken from J-G. Park *et al* (1998)].

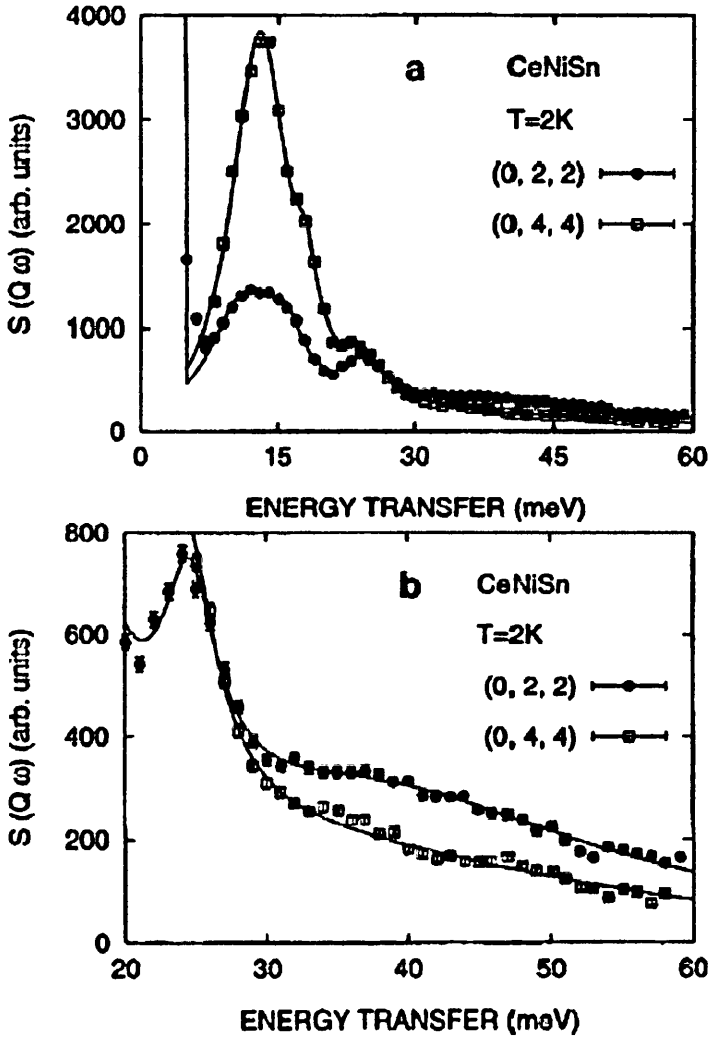

Figure 2.15: a) Inelastic neutron scattering data for Q = (0,2,2) and (0,4,4). Clearly visible are the low-lying phonon peaks below 30 meV. The high energy results are enlarged in (b), which shows the broad peak at about 40 meV, attributed to a CEF excitation. [Taken from J-G. Park *et al* (1998)].

CHAPTER 3

Literature Survey

In recent years widespread interest has been growing in intermetallic compounds which show a variety of unusual properties. Many of these properties arise from the ground state of the system, and in studying these compounds we can understand the fundamental physics governing their behaviour. The RTX group, where R is a rare earth metal, T a transition element and X a metalloid, contains a multitude of different interesting properties that have a basis in magnetism. These properties are due to the electron behaviour within the system. The $4f$ moments from the rare earths have a localised character, while the d moments are itinerant. Cataloguing all these systems is a long and arduous task, but in narrowing the search down to certain series we can attempt to isolate and investigate interesting trends.

In this chapter I have concentrated on 5 such series: RNiSn (R = Ce to Yb), PrTSn and NdTSn (T = Ni, Pd and Pt) and PrNiX and NdNiX (X = Ge, Sn and Pb). There are many papers dealing with most of these compounds, but surprisingly there are several omissions within each series. The techniques and measurements for each compound has been researched and put into the context of a series, allowing us to see the change in properties with a change in one of the elements.

3.1 RNiSn

The majority of the compounds within this series have been studied in quite some detail. All have the orthorhombic TiNiSi-type structure, but it is well known that this structure is closely related to the $CeCu_2$-type structure. It is possible to describe these ternary alloys with the $CeCu_2$-type structure by considering the nickel and tin disordered on the copper site. To convert between the two systems is quite easy. From the TiNiSi-type cell, shift the origin by (¼, ¼, ¼) and interchange the **a** and **b** axes.

As expected for a rare earth based series, the unit cell volume decreases with increasing atomic number and is demonstrated by D. Rossi *et al* (1985). Using their own work, and that of A. E. Dwight *et al* (1983), they confirmed the TiNiSi-type structure for the RNiSn and RPdSn compounds, detailing the lattice constants found from X-ray powder diffraction experiments.

The compounds in this RNiSn series have been studied to varying degrees. Of the light rare earth alloys, CeNiSn has the most literature on its properties, while PrNiSn and NdNiSn are relatively unresearched. I have dealt with CeNiSn in Chapter 2, because of the large amount of material available on this compound, along with UNiSn. CeNiSn shows behaviour not seen in the other RNiSn compounds, demonstrating a semiconductor pseudogap at low temperature, due to the 4*f* electrons being very close to the Fermi level. No measurements have been carried out below 4.2 K for PrNiSn, and only one study below this temperature has been carried out for NdNiSn. As part of their study on Nd_2Ni_2Sn, B. Chevalier *et al* (1996) carried out magnetisation and susceptibility measurements on NdNiSn, discovering the compound had a transition at T = 3.0 K [Figure 3.1]. They also determined a spin flip transition at the applied field H = 1 T [Insert, Figure 3.1].

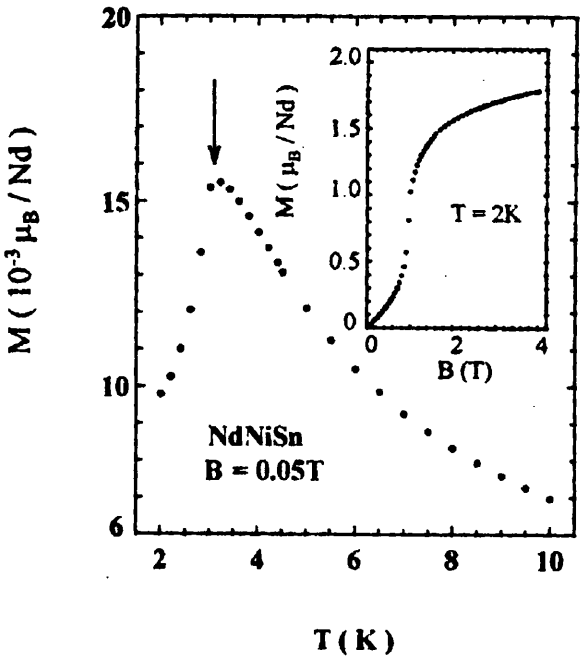

Figure 3.1: Temperature dependence of the magnetisation of NdNiSn measured in an applied field of 0.05 T, where T_N is indicated by the arrow. The inset shows the field dependence at 2 K of the magnetisation. [B. Chevalier *et al* (1996)]

Most of the papers pertaining to this series are concentrated in the heavy rare earth end of the lanthanides. The properties of all the RNiSn, where R = Gd to Yb, are well documented, both in the polycrystalline and single crystal state. It is worth noting the results of magnetisation measurements performed on single crystals of TbNiSn and DyNiSn (M. Kurisu *et al* (1994)). At low temperature (T = 1.6 K), multi-step metamagnetic processes are observed along the **b** axis for both compounds [Figure 3.2].

If the transition temperatures are plotted along the RNiSn series, it is clear that they do not follow the deGennes scaling when normalised to the Néel temperature of GdNiSn [Figure 3.3]. In the RKKY model, the ordering temperatures are proportional to $G = (g_J - 1)^2 J (J+1)$. It is therefore clear that the Crystalline Electric Field is a factor when determining the properties of this series.

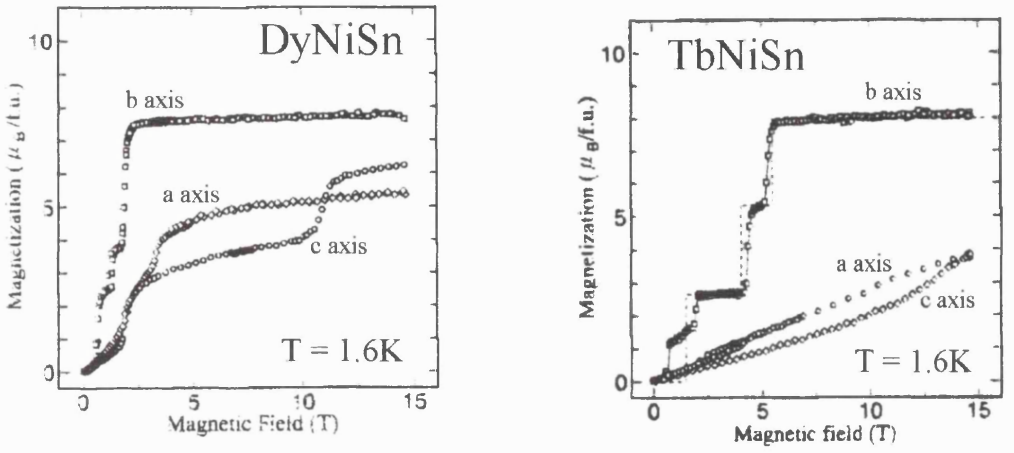

Figure 3.2: The magnetisation curves along the **a**, **b**, and **c** axes for the single crystals of DyNiSn and TbNiSn at T = 1.6 K. [M. Kurisu *et al* (1994)].

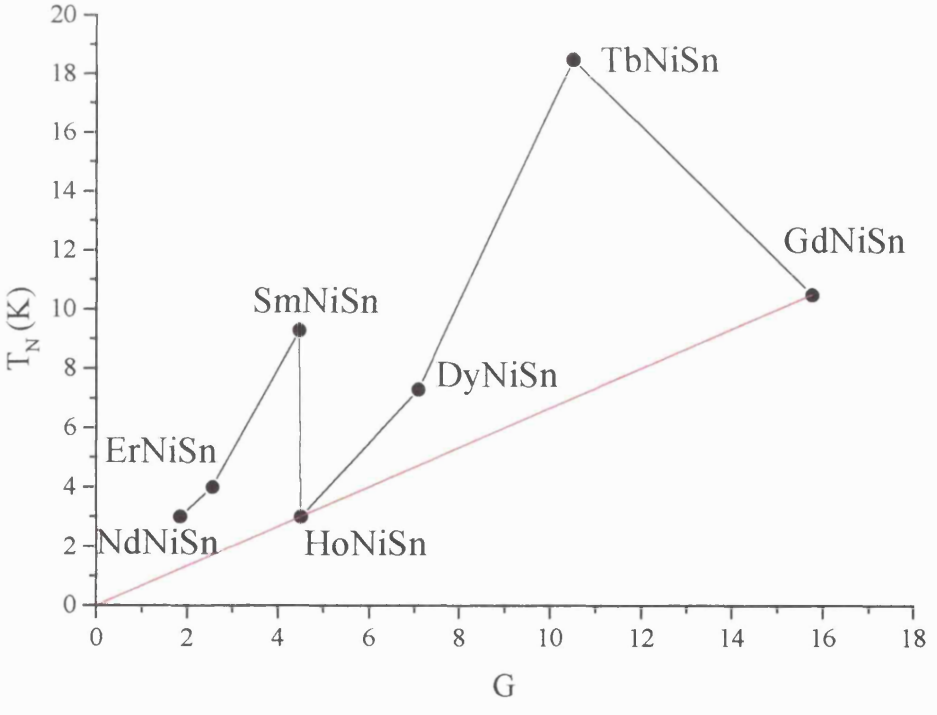

Figure 3.3: The dependence of the Néel temperature as a deGennes function for RNiSn, scaled to GdNiSn.

	a (Å)	b (Å)	c (Å)	V_{atom} (Å^3)	θ_{CW} (K)	μ_{eff} (μ_B)	T_N (K)	Easy axis	
CeNiSn					$\chi^{-1}vT^{0.3}$	-	-	A	Ch. D. Routsi *et al* (1992a)
PrNiSn	7.440	4.560	7.706	21.8	-10	3.67	-		Ch. D. Routsi *et al* (1992a)
NdNiSn	7.395	4.541	7.690	21.5	-4	4.2	-		Ch. D. Routsi *et al*
	-	-	-	-	-12	3.74	3.0		(1992a)
									B. Cheavlier *et al* (1996)
SmNiSn	7.304	4.509	7.680	21.1			9.3, 4.1		J. Sakurai *et al* (1995)
GdNiSn	7.199	4.464	7.677	20.6	-3	8.8	10.3		Ch. D. Routsi *et al*
							10.5		(1991)
						7.0	11.0	A	A. Oki *et al* (1998)
									Y. Andoh *et al* (1998)
TbNiSn	7.146	4.448	6.661	20.3	6	11.27	7.2*		Ch. D. Routsi *et al*
						9.65	6,7.6,18.5	B	(1991)
							2,6,7.6,18.5		M. Kurisu *et al* (1994)
									Y. Andoh *et al* (1997)
DyNiSn	7.112	4.439	7.656	20.1	-1	11.06	8.2		Ch. D. Routsi *et al*
							5.4,7.3	B	(1991)
							6.5		M. Kurisu *et al* (1994)
									S. Kawano *et al* (1998)
HoNiSn	7.063	4.438	7.640	20.0	-2	10.75	-		Ch. D. Routsi *et al*
						8.6	3	B	(1991)
									Y. Andoh *et al* (1998)
ErNiSn	7.016	4.425	7.629	19.7	6	9.6	-		Ch. D. Routsi *et al*
						9.0	4	A	(1991)
									Y. Andoh *et al* (1998)
TmNiSn	7.000	4.414	7.621	19.6	-4	7.65	-		Ch. D. Routsi *et al*
									(1991)
YbNiSn	6.983	4.426	7.616	19.6	57		5.5†	A	M Kasaya *et al* (1991)
							5.3†		L. D'Onofrio *et al* (1991)
	6.924	4.382	7.588			0.84	5.65†	A	P. Bonville *et al* (1992)
	6.970	4.412	7.590				5.6†		D. T. Adroja *et al* (1998)

Table 3.1: Crystal data and some properties of the RNiSn alloys. The lattice parameters and cell volume ($V_{atom} = V_{cell}/12$) are taken from A. E. Dwight (1983), the properties from various papers as indicated. † Ferromagnetic transition.

PrTSn & NdTSn

	Structure	a (Å)	b (Å)	c (Å)	V_{atom} (Å^3)	θ_{CW} (K)	μ_{eff} (μ_B)	T_N (K)	Ref.
PrNiSn	TiNiSi	7.440	4.560	7.706	21.8	-10	3.67	-	Ch. D. Routsi *et al* (1992a)
PrPdSn	TiNiSi	7.475	4.680	7.979	23.3				
	TiNiSi	7.44	4.66	7.95	23.0		3.39	4.6	M. Kolenda *et al* (1998)
PrPtSn	Fe_2P					-8	3.78	-	Ch. D. Routsi *et al* (1992b)
NdNiSn	TiNiSi	7.395	4.541	7.690	21.5	-4	4.2	-	Ch. D. Routsi *et al*
		-	-	-	-	-12	3.74	3.0	B. Chevalier *et al* (1996)
NdPdSn	TiNiSi	7.424	4.665	7.951	23.0				
	TiNiSi	7.36	4.63	7.90	22.5		1.94	3.6	M. Kolenda *et al* (1998)
NdPtSn	Fe_2P					-10		-	Ch. D. Routsi *et al* (1992b)

Table 3.2: Crystal data and some properties of the PrTSn and NdTSn alloys. The lattice parameters and cell volume ($V_{atom} = V_{cell}/12$) for PrNiSn, PrPdSn, NdNiSn and NdPdSn are taken from A. E. Dwight (1983) and D. Rossi *et al* (1985), the properties from various papers as indicated.

PrNiX & NdNiX

	Structure	a (Å)	b (Å)	c (Å)	V_{atom} (Å^3)	θ_{CW} (K)	μ_{eff} (μ_B)	T_N (K)	Ref.
PrNiGe									
PrNiSn	TiNiSi	7.440	4.560	7.706	21.8	-10	3.67	-	Ch. D. Routsi *et al* (1992a)
PrNiPb									
NdNiGe									
NdNiSn	TiNiSi	7.395	4.541	7.690	21.5	-4	4.2	-	Ch. D. Routsi *et al*
		-	-	-	-	-12	3.74	3.0	B. Chevalier *et al* (1996)
NdNiPb	TiNiSi	7.42	4.61	7.82	22.3				L.D. Gulay *et al* (2000)

Table 3.3: Crystal data and some properties of the PrNiX and NdNiX alloys. The lattice parameters and cell volume ($V_{atom} = V_{cell}/12$) for PrNiSn, PrPdSn, NdNiSn and NdPdSn are taken from A. E. Dwight (1983) and D. Rossi *et al* (1985), the properties from various papers as indicated.

3.2 PrTSn & NdTSn, and PrNiX & NdNiX

Table 3.2 shows the main properties for both these series. It is obvious, that unlike the RNiSn series, the crystal structure is different as you change the transition metal. The introduction of Pt changes the structure from TiNiSi-type to Fe_2P-type. What is also clear is that neither PrPtSn nor NdPtSn have a magnetic transition down to 4.2 K [Routsi *et al* (1992b)].

PrPdSn and NdPdSn have both been studied to a greater degree, such that the crystal structures and magnetic structures have been refined [Figures 3.4 and 3.5]. The inserts to these figures clearly show the antiferromagnetic transition at T_N = 4.6 K and 3.6 K respectively.

Out of all the series I researched, the PrNiX and NdNiX series [Table 3.3] had the least information. Apart from the results of PrNiSn and NdNiSn, which I have already discussed, the only other compound from either of these series to have been investigated is NdNiPb. Like PrNiSn and NdNiSn, NdNiPb has the TiNiSi-type structure, with the lattice parameters listed in Table 3.3. No other measurements have been carried out for this compound. It should be noted at this point that the author attempted to arc-melt a button of PrNiPb, but was unsuccessful after several attempts. It was found that the Pb did not wish to form a melt with the other two elements, and when X-ray diffraction was carried out on the button, the Pb Bragg peaks were clearly visible.

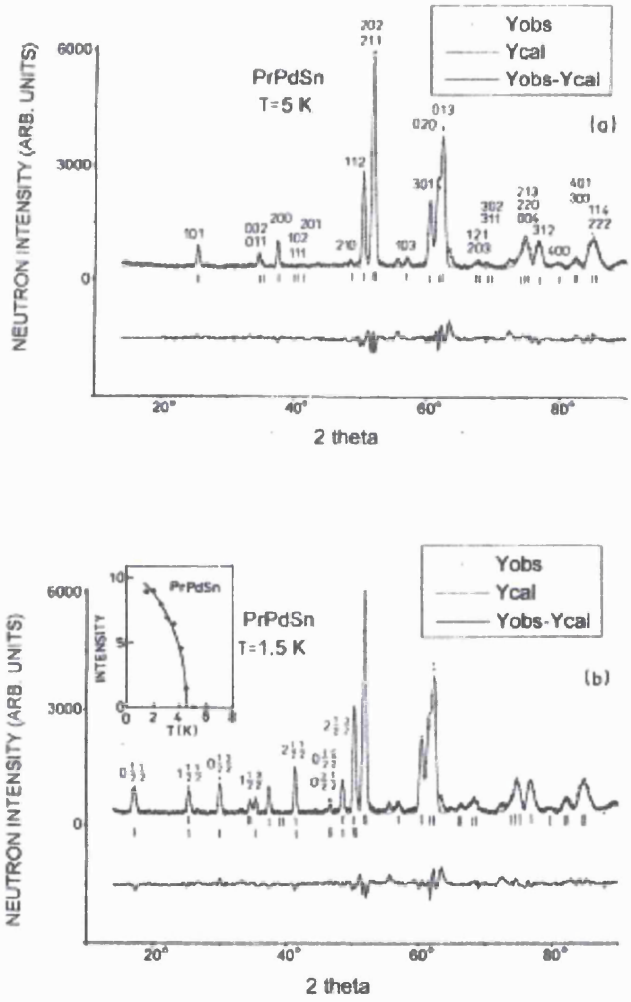

Figure 3.4: Neutron diffraction patterns of PrPdSn at (a) 5 K paramagnetic phase and (b) 1.5 K magnetic phase. The inset to (b) depicts the temperature dependence of the (0 ½ ½) peak [M. Kolenda *et al* (1998)].

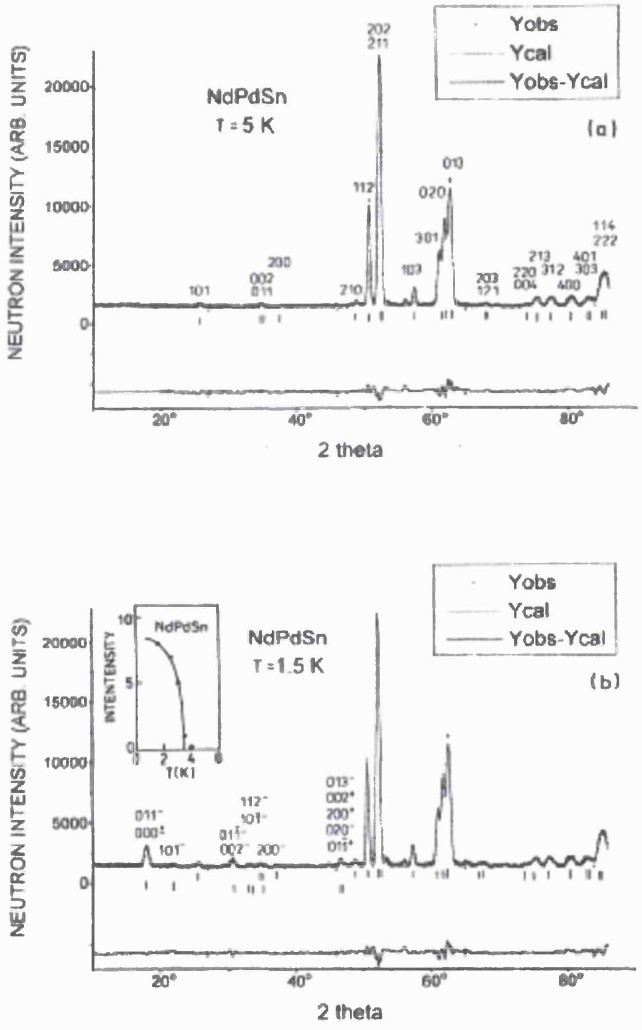

Figure 3.5: Neutron diffraction patterns of NdPdSn at (a) 5 K paramagnetic phase and (b) 1.5 K magnetic phase. The inset to (b) depicts the temperature dependence of the magnetic (0 0 0) and (0 1 1) peaks [M. Kolenda *et al* (1998)].

CHAPTER 4

PrNiSn

4.1 Neutron powder diffraction

Previous work [Rossi *et al* (1985)] on PrNiSn shows the crystal structure to be the orthorhombic TiNiSi-type. This is described by the space group *Pnma*, with the rare earth atoms located on the 4(c) site: $x,1/4,z$; $\bar{x},3/4,\bar{z}$; $1/2-x,3/4,1/2+z$; $1/2+x,1/4,1/2-z$. [Figure 4.1], where $x = 0.00$ and $z = 0.70$.

As mentioned earlier in this work, no evidence of long-range magnetic order has been detected in bulk property measurements down to 2 K, but if there is any ordering, neutron diffraction should be able to resolve it. The aims of this experiment was therefore to confirm previous X-ray data [Rossi *et al* (1985)] at room temperature, confirm no long-range magnetic order down to 1.7 K and to look for any evidence of splitting in the crystallographic peaks due to CEF effects.

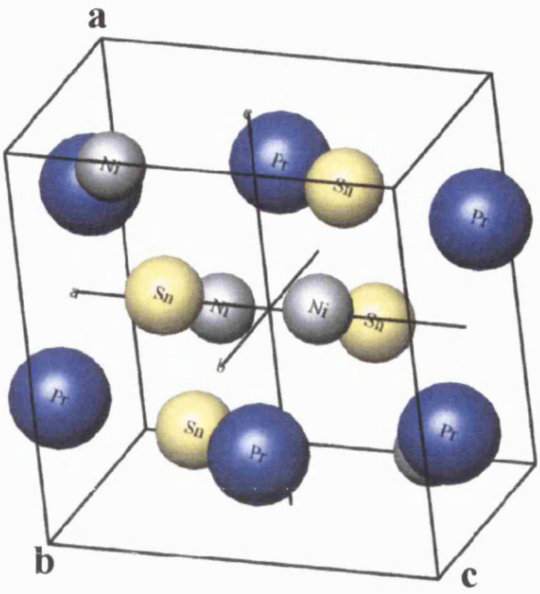

Figure 4.1: PrNiSn shown in the TiNiSi-type structure configuration, with the different atoms indicated. See text for details.

4.1.1 Experimental procedure

The sample was prepared by arc melting the constituent elements under an argon atmosphere. The purity was 99.999% for Ni and Sn and 99.9% for Pr. The mixture was melted several times to achieve homogeneity, with a small percentage (<1%) of extra Sn to account for any mass loss. The buttons were then annealed at 500°C and P ≈ 5×10^{-6} Torr for 7 days. The mass of sample used in the experiment was approximately 10g, filled in a vanadium can and mounted in an Orange cryostat. The D20 high intensity two-axis powder diffractometer provided neutrons with a wavelength of $\lambda = 2.4$ Å and with a Roots pump attached we were able to achieve temperatures of 1.7 K. The counting time for each data file is 90 minutes, with $10 \leq 2\theta \leq 160$. The data was analysed by the Rietveld method using the Fullprof98 program, which is based on a least squares refinement [H.M. Rietveld (1969)].

4.1.2 Results

Neutron powder diffraction data was taken at 35 K, 6 K and 1.7 K and at each temperature the data is indexed by assuming the system was of the TiNiSi-type. The starting parameters, such as the lattice parameters and atomic positions are taken from Rossi *et al's* paper that gave the above structure. The calculated parameters for 1.7 K and 35 K are given in Table 4.1 and the corresponding plots showing the raw data, Rietveld fit and difference are shown in Figures 4.2 and 4.3. The peaks are fitted to a pseudo-Voigt shape, which is a weighted mixture of Gaussian and Cauchy profiles.

Upon inspection of the subtraction plots from 1.7 K – 35 K and 6 K – 35 K, there is no clear evidence of splitting in the peaks. This is not wholly unexpected, due to the instrument characteristics. The neutron flux on D20 is very high, yielding data at a faster rate than normal instruments, such as D2b. Unfortunately, this high flux rate is offset by a relatively poor resolution. To investigate the possibility of splitting in the peaks, experimental time is necessary on an instrument such as D2b, which has high resolution. However, as can be seen in figure 4.4, there is a clearly a small difference between 35 K - 6 K and 1.7 K - 6 K. When the 6 K data is subtracted from the 1.7 K data, the resulting difference is small, especially when compared to the subtraction plot of 6 K – 35 K. It is perhaps most easily seen in the (1 0 1) peak at $2\theta = 26°$. The ratio of this difference is 1:2.57 in peak height. The fractional difference for this peak between 6 K and 35 K is 0.026.

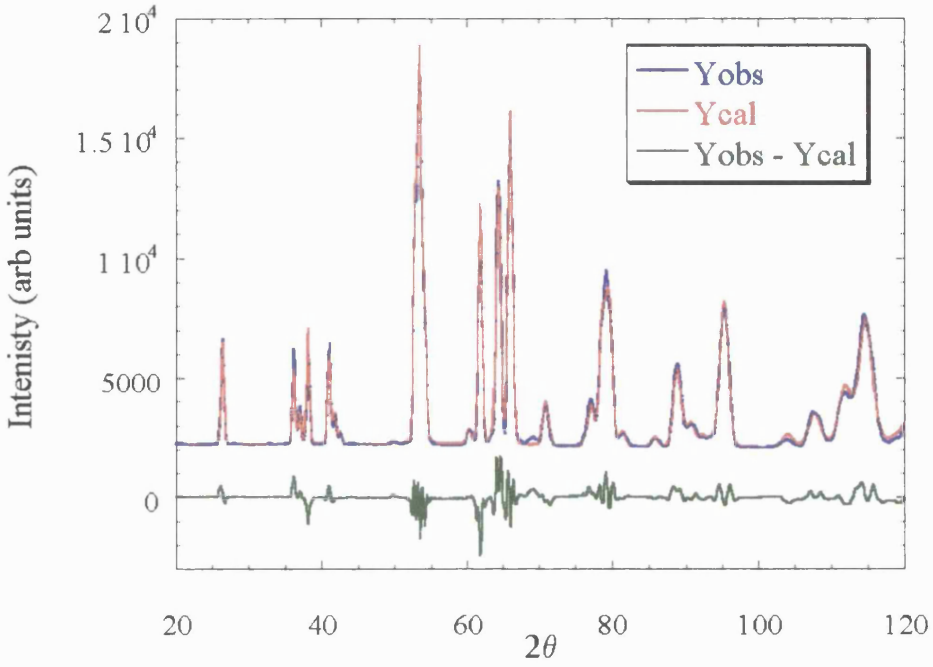

Figure 4.2: 1.7 K powder diffraction pattern with Rietveld refinement obtained using Fullprof98

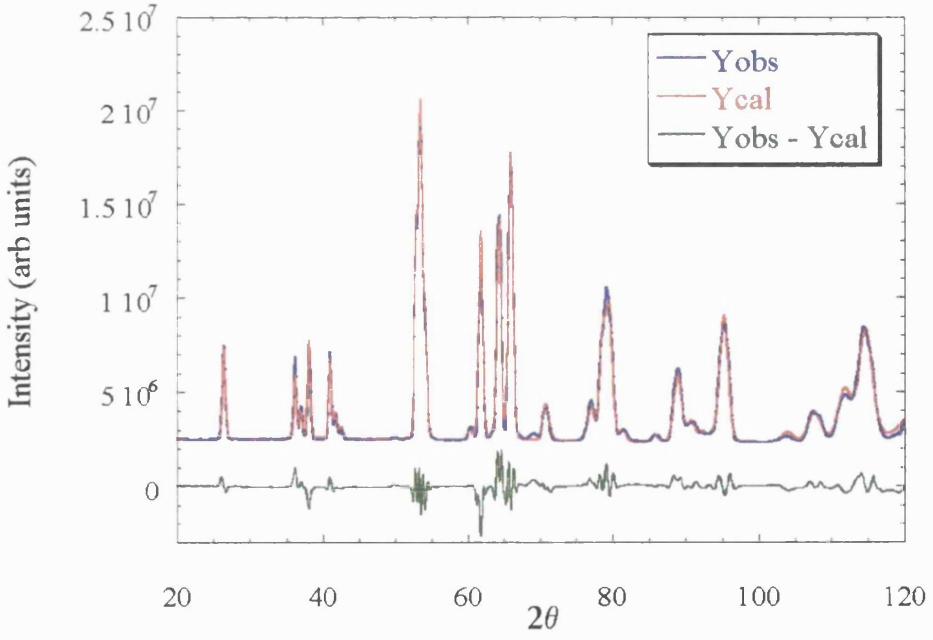

Figure 4.3: 35 K powder diffraction pattern with Rietveld refinement obtained using Fullprof98

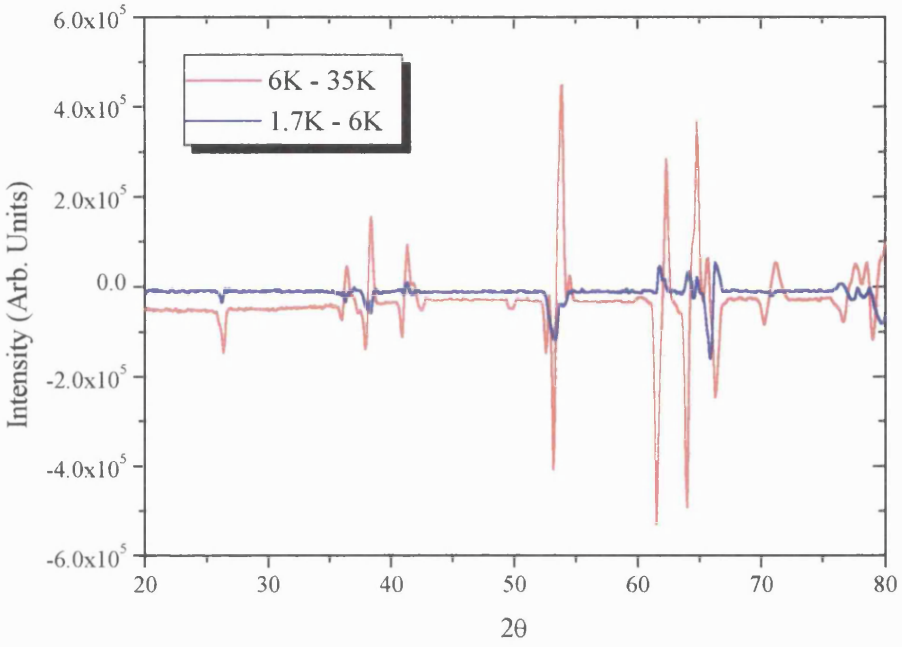

Figure 4.4: Comparison of the difference plots between the 1.7 K & 6 K data and the 6 K & 35 K data. It is clear that there is less difference at low temperature, suggesting the possibility of a structural distortion at about 6 K

The fractional changes of the lattice parameters between T = 1.7 K and 35 K are:

$$(\mathbf{a}_{35} - \mathbf{a}_{1.7}) / \mathbf{a}_{35} = 4.95 * 10^{-4}$$
$$(\mathbf{b}_{35} - \mathbf{b}_{1.7}) / \mathbf{b}_{35} = 3.27 * 10^{-4}$$
$$(\mathbf{c}_{35} - \mathbf{c}_{1.7}) / \mathbf{c}_{35} = 8.29 * 10^{-5}$$

It is clear that the largest change is along the **a** axis. The fractional change along **c** is the smallest, at approximately 6 times as small as the change along **a**. As expected, there is a very small reduction in the cell volume between 35 K and 1.7 K, from 253.8 $Å^3$ to 253.6 $Å^3$. Rossi *et al* (1985) report the cell volume to be 261 $Å^3$ at room temperature.

	35K	1.7K
a (Å)	7.38849 ± 0.00102	7.38483 ± 0.00104
b (Å)	4.52076 ± 0.00056	4.51928 ± 0.00057
c (Å)	7.59909 ± 0.00099	7.59846 ± 0.00101
V ($Å^3$)	253.822 ± 0.058	253.592 ± 0.059
Pr		
X	-0.02205(168)	-0.02137(172)
Z	0.69763(88)	0.69665(88)
Ni		
X	0.19429(60)	0.19581(57)
Z	0.08563(78)	0.08649(78)
Sn		
X	0.32034(90)	0.32131(84)
Z	0.41171(143)	0.41215(143)
R_{BRAGG}(%)	7.26	8.12

Table 4.1: Lattice parameters and atomic positions for PrNiSn obtained from the Reitveld fitting to the Pnma space group (TiNiSi-type structure).

4.2 Polycrystalline powder inelastic neutron scattering (HET, ISIS)

4.2.1 Experimental procedure.

Inelastic neutron scattering was carried out on a 20g PrNiSn powder sample on the HET chopper spectrometer at ISIS, Didcot. The powder was wrapped in an aluminium sachet, with a face approximately 4 cm by 4 cm. The sample was then mounted in a top loading Closed Cycle Refrigerator (CCR). For all measurements the sloppy chopper was used, yielding a high neutron count but a lower resolution than a fixed chopper. The different types of Fermi choppers are discussed in Section 1.3.3.1

4.2.2 CEF excitation results.

Inelastic measurements were taken at 4 different incident energies: 23, 35, 60 and 800 meV. The specifications for each run are shown in Table 4.2.

E_i (meV)	μAhr	Chopper Frequency (Hz)	T_{head} (K)	T_{sample} (K)
23	534	200	8.3±0.8	10.7±0.7
35	535	200	8.3±0.2	10.8±0.7
60	611	200	8.3±0.2	11.2±1.1
800	600	600	8.1±0.2	10.6±0.5
23	500	200	23.8±4.5	24.6±4.0
35	360	200	99.3±7.1	97.7±9.3

Table 4.2: Specifications of the data runs for PrNiSn on HET, showing the incident energy E_i, μAhrs, chopper frequency, and the average temperature of the CCR head and sample.

From the available data [Figures 4.7 - 4.13], we can see a total of 7 CEF peaks at ≈ 2, 3.5, 5, 7.5, 17.5 23 and 28 meV. With the Pr ion having J = 4, we would expect a total of 9 singlet states, giving a maximum of 8 transitions from the ground state.

Each data set must firstly be normalised to the incoherent scattering from a vanadium standard for each incident energy. Vanadium has low coherent scattering, but a large incoherent scattering cross-section. We can then determine for each detector the relative counts and account for the discrepancies between each point. Thus the data is not produced as counts, but as a scattering function $S(\varphi,\mathbf{E})$ with units $mbsr^{-1}meV^{-1}fu^{-1}$. It is possible to estimate the actual number of counts from the error on each point, assuming that the error is $\sqrt{N}$.

Another difficulty in analysing inelastic neutron scattering data is separating the magnetic response from the phonon modes of the crystal. For this we use the fact that any magnetic scattering is very small or zero intensity at high momentum transfers, as a result of the wave vector dependence of magnetic form factors. Due to the detector array on HET, the signal at high scattering angles is therefore entirely phonon based. The forward detector bank, at low angles, detects a mixture of magnetic and phonon scattering. The average angle of each detector bank is shown in Table 4.3.

	w1	w2	w3	w4	w5	w6	w7	w8
ϕ	4.9	4.9	11.5	16.5	21.5	26.5	115	135

Table 4.3: The average angle of the detector bank workspaces on HET at the time of the experiment. w1 and w2 are the 4m low angle bank detectors, w3-w6 the 2.5m low angle bank detectors, and w7 and w8 the 4m and 2.5m high angle bank detectors respectively.

To determine the magnetic response only, a non-magnetic reference compound with the same crystal structure is needed. In this case, LaNiSn is used [Figures 4.5 – 4.6].

Other examples of reference samples include ThNiSn for studies on UNiSn and YPd_3 for UPd_3 experiments. We assume that the average phonon contribution is the same for the reference material and the sample.

The phonon scattering in the low-angle raw data is then estimated by multiplying the high-angle sample data by the ratio of the low-angle: high-angle data from the reference material [Figures 4.5 – 4.6]. In the case of most materials, this ratio is approximately 1:5. Initial analysis can then be carried out using this ratio. But as is evident in the E_i = 35 meV and 60 meV data [discussed below, Figures 6 - 10], it is sometimes necessary to carry out the detailed analysis to eliminate weak excitations that would otherwise be mistaken for magnetic modes.

Figure 4.7 shows the two 2.5m bank spectra taken with an energy transfer of 23 meV, at T = 10 K and 25 K. At 10 K it is apparent there are 4 peaks below 10 meV. As we increase the temperature, their widths decrease. Although we can still see the peaks at 25 K, they are not as distinct. It is possible to fit the excitations at 10 K to Gaussians, as shown in Figure 4.8.

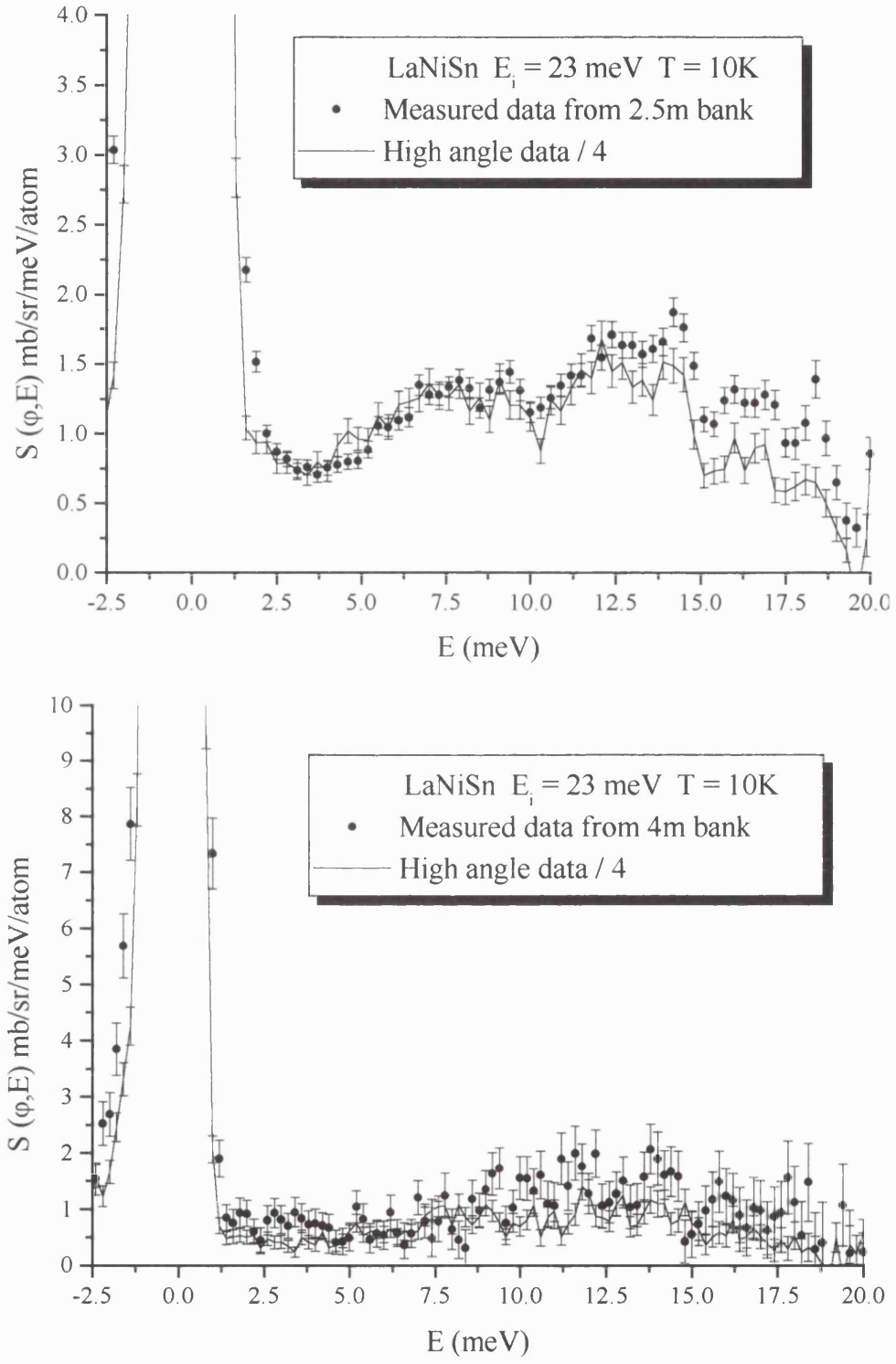

Figure 4.5: Inelastic neutron scattering on powder LaNiSn with E_i = 23 meV at T = 10 K. The graphs show the raw data for both 2.5 and 4m bank, with the estimated phonon background from the high angle detector banks.

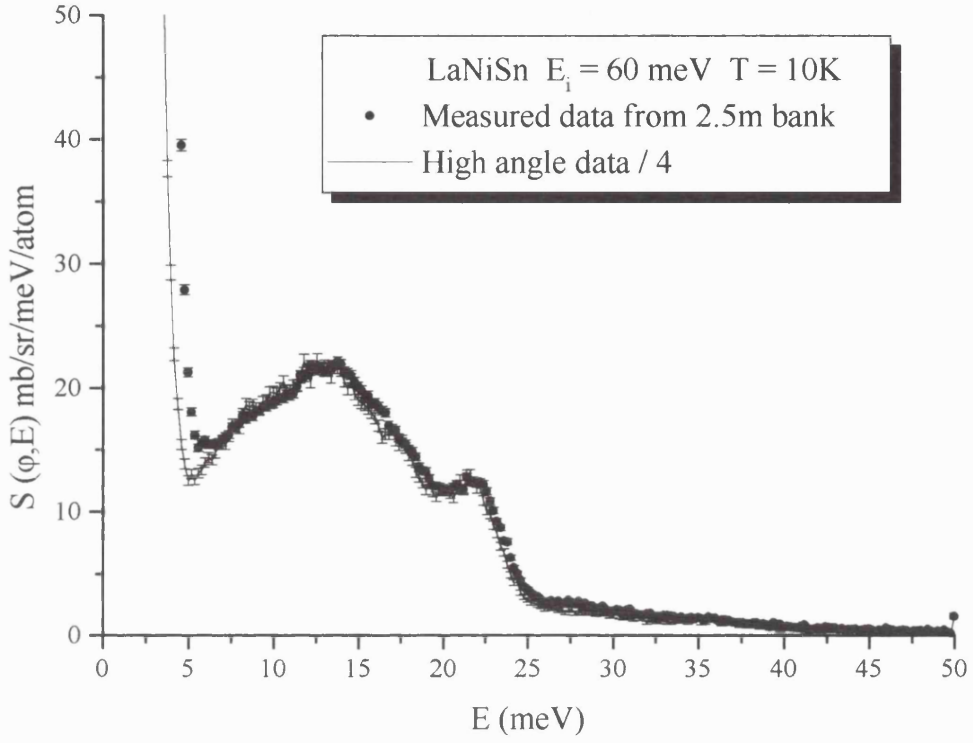

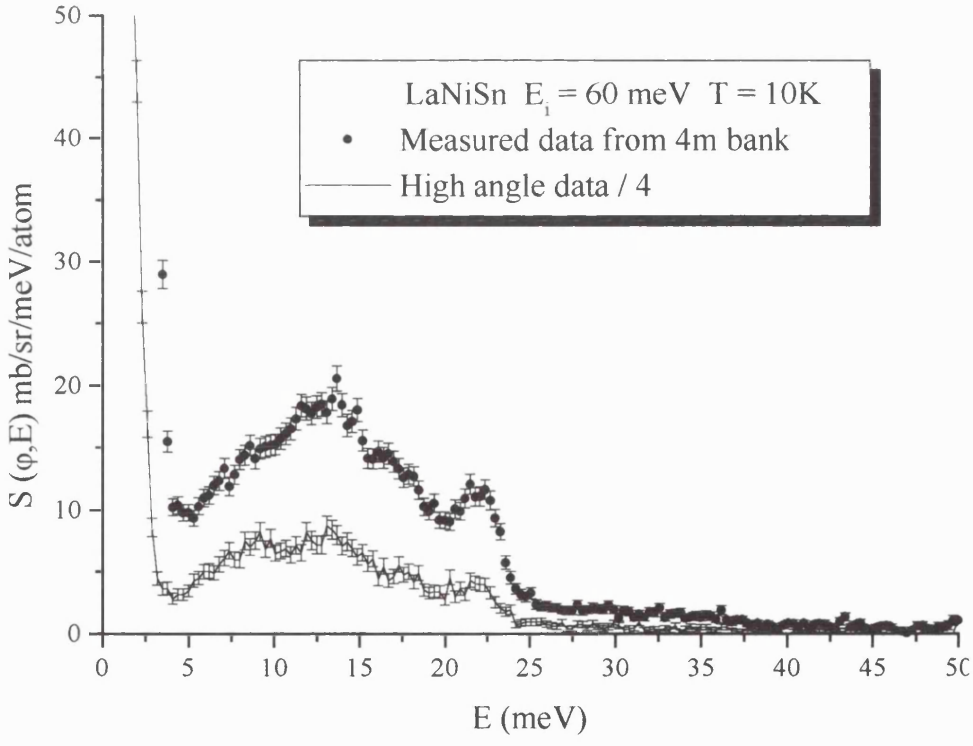

Figure 4.6: Inelastic neutron scattering on powder LaNiSn with E_i = 60 meV at T = 10 K. The graphs show the raw data for both 2.5 and 4m bank, with the estimated phonon background from the high angle detector banks.

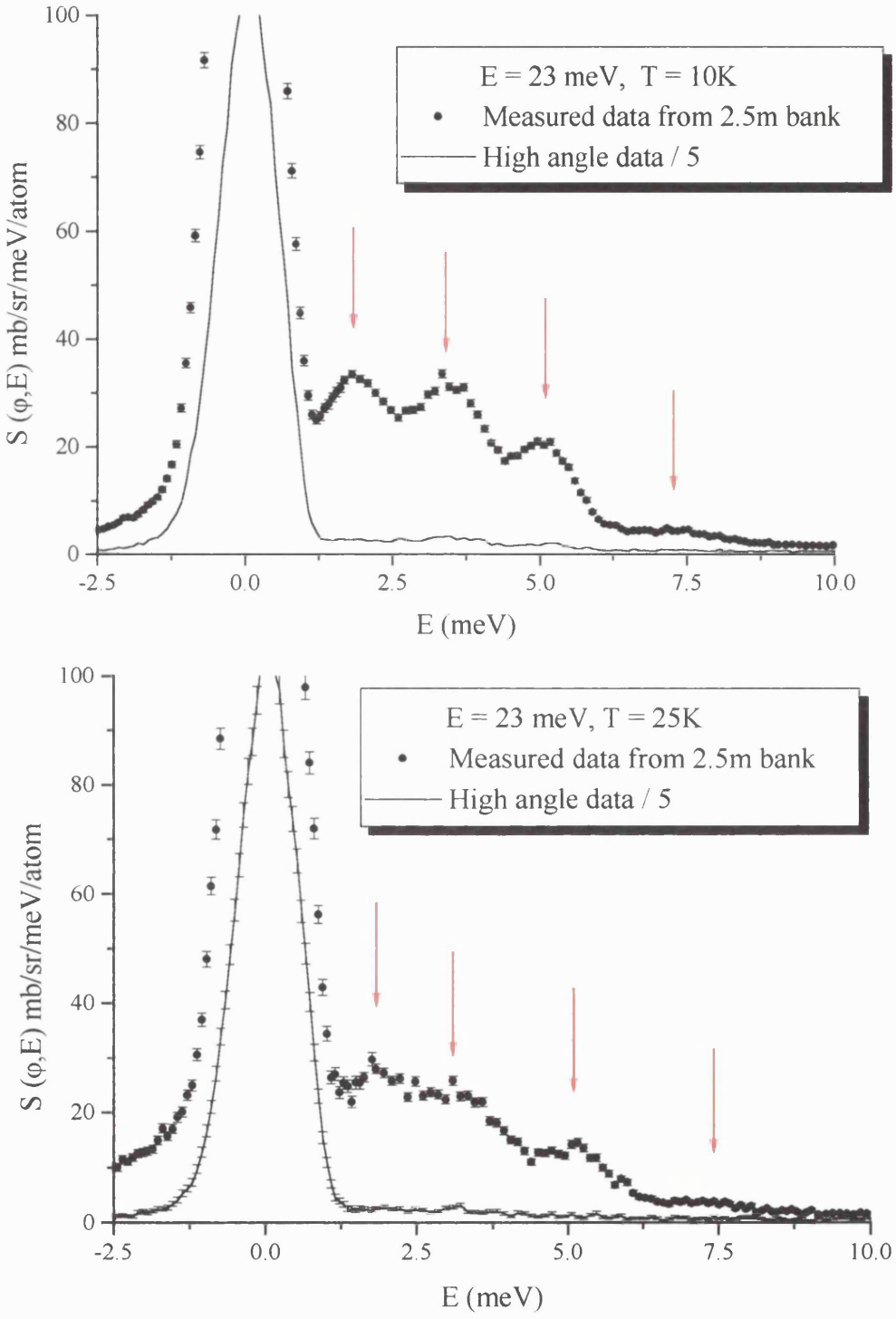

Figure 4.7: Inelastic neutron scattering on powder PrNiSn with an incident energy of 23 meV, for T=10 K and 25 K. At 10 K 4 peaks are evident, marked by arrows. The change in shape is demonstrated in the bottom graph at 25 K. Each spectrum is 500 – 600 μAhr, which takes approximately 3 hours. Raw data from the 2.5m bank is shown, as well as the phonon contribution estimated from w8/5.

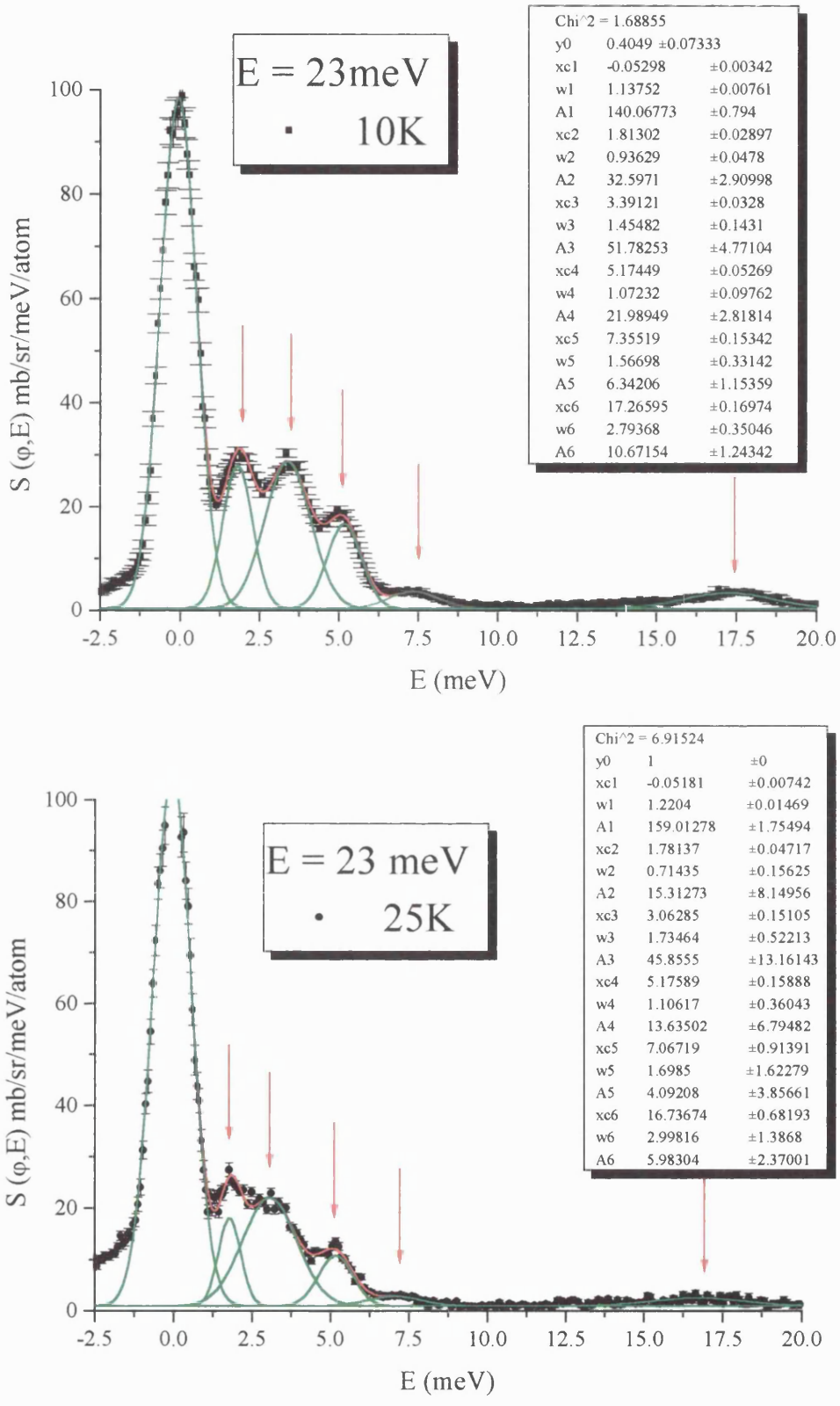

Figure 4.8: Gaussian fit to the 5 lowest excitations seen in the 23 meV incident energy spectrum at 10 K and 25 K. The parameters for each peak are shown in the inserts. The fits are to the raw 2.5m bank data minus the phonon contribution estimated from w8/5.

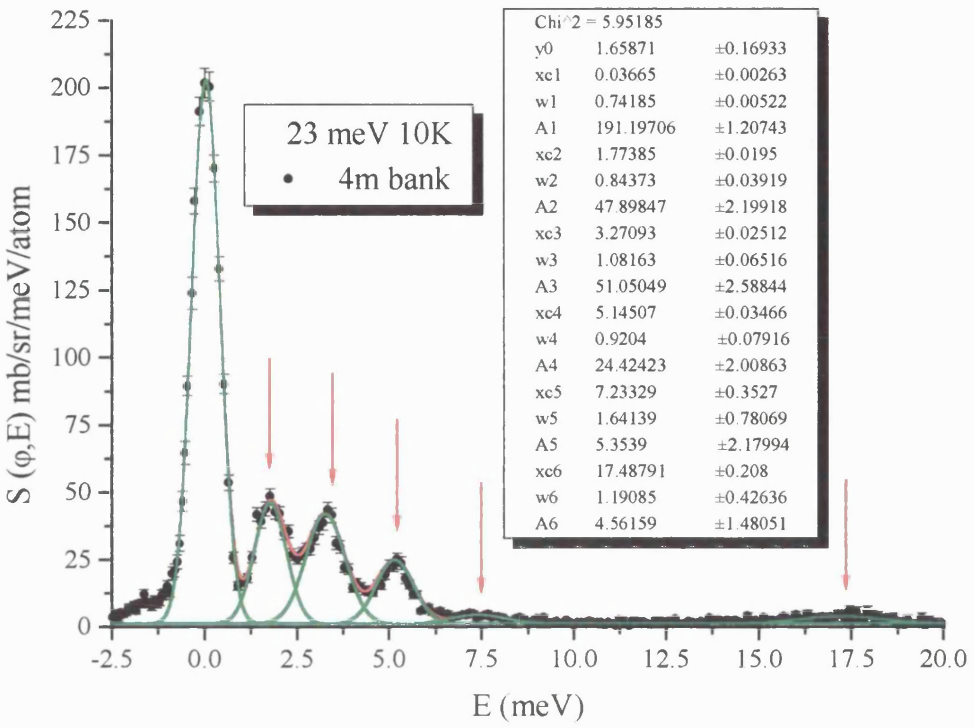

Figure 4.9: 4m bank data showing the lowest 5 excitations seen with incident energy E_i = 23 meV at 10 K.

Fitting each excitation in the 2.5 m bank E_i = 23 meV spectrum at 10 K to a Gaussian yields 5 modes at E = 1.81±0.03, 3.39±0.03, 5.17±0.05, 7.36±0.15 and 17.27±0.17 meV. The widths and areas of the peaks are given in the insert to Figure 4.8 and in Table 4.4. The excitations are also observed in the 4m bank and fitting to a Gaussian peak shape [Figure 4.9] gives comparable energy positions of E = 1.77±0.02, 3.27±0.03, 5.14±0.03, 7.23±0.35 and 17.49±0.21 meV [Table 4.4]. It is obvious that there may be peaks below 1.81 meV, but due to the width of the elastic peak they are not visible. It is also possible that there are more modes within the range 1 - 6.5 meV, but it is impossible to fit more than those already described.

Two more excitations, as well as the 17.3 meV excitation, are visible with an incident energy of 35 meV [Figures 4.10 – 4.11] and 60 meV [Figures 4.12 – 4.14]. The modes below 17.3 meV are not seen due to the large width of the elastic peak at this energy.

It appears that the two modes above 17.3 meV are at approximately 23 meV and 28 meV. As we move higher in temperature it appears that the mode at 23 meV is also seen at 100 K [Figure 4.10, blue arrow]. This appears to be borne out by a difference plot of the two spectra showing two clear excitations at 17.5 meV and 28 meV [Figure 4.10].

If we look at the 4m bank data, three higher energy excitations are well defined, and the question of whether the 23 meV peak exists or is background appears to be clearly answered. The 3 high energy excitations at 10 K seen in the 35 meV energy transfer spectrum are also very clearly seen in the 60 meV spectrum [Figures 4.12 – 4.14]. Fitting to the data it is firstly clear that the high energy tail of the elastic peak is not fitted satisfactorily. This is expected, since the elastic peak is very broad at this energy and incorporates the 4 lowest energy modes seen in the 23 meV data. The fit parameters to the 3 excitations are given in Table 4.4, along with the parameters from the 23 meV fits.

The 60 meV data allows us to check the validity of the phonon correction method using LaNiSn as a reference material. Figure 4.12 shows 2 phonon contributions. The first is using the ratio method, and clearly shows some peaks at 12.5 meV and 23 meV. The red data curve is taking the high angle bank PrNiSn data and dividing it by 4. It was noted earlier that initial analysis may be carried out by dividing the high bank data by 5. It is clear from Figure 4.12 that the ratio of 1:4 is an excellent fit to the reference material phonon ratio. This is important in this case because of the excitation at 23 meV. If we assume the ratio is 1:5, we have to fit the corrected 60 meV data to 3 peaks and assume that they are CEF excitations. Correcting the raw data with the ratio 1:4 however, makes fitting 3 Gaussians to the spectrum more difficult. This poses the question as to whether or not the 23 meV CEF excitation is present. According to the E_i = 35 meV 4m bank data, there is an excitation at this energy [Figure 4.11]. Although in the E_i = 60 meV 2.5m bank data it is difficult to fit 3 CEF peaks, the 4m bank data [Figure 4.14], like the 35 meV 4m bank data, clearly shows a peak at 23 meV.

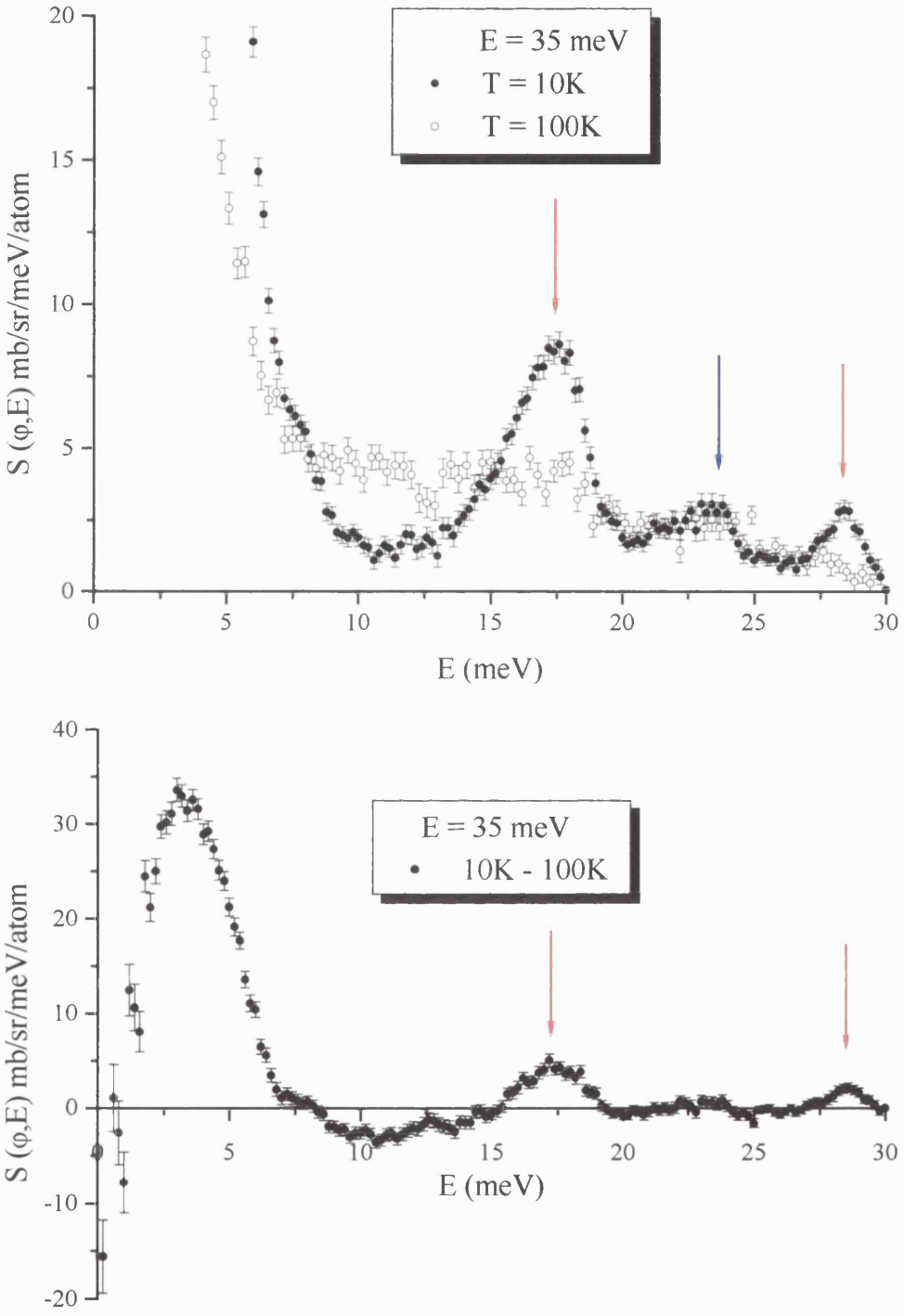

Figure 4.10: Inelastic neutron scattering from the 2.5m bank, with incident energy of 35 meV at T = 10 K and 100 K. The 10 K has 3 peaks, at E ≈ 17.5 meV, 23 meV and 28 meV. The blue arrow shows the peak seen at 10 K that appears to be present at 100 K. The 2 clear CEF excitations are indicated in the difference plot of the 2 spectra by arrows.

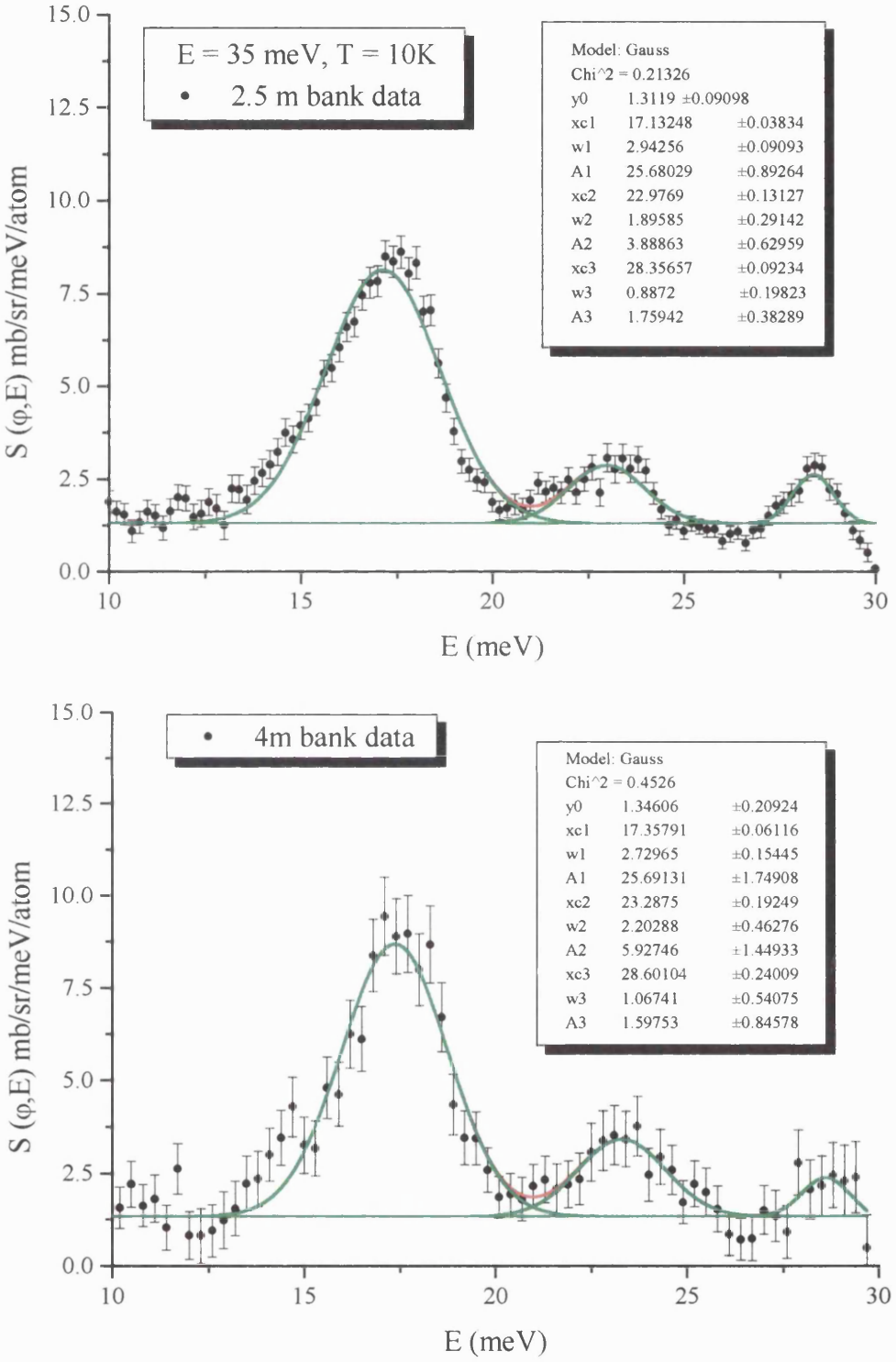

Figure 4.11: Gaussian fit to the 3 highest excitations seen in the 2.5m and 4m banks E_i = 35 meV spectra, minus the phonon contribution. The parameters for each peak are shown in the inserts.

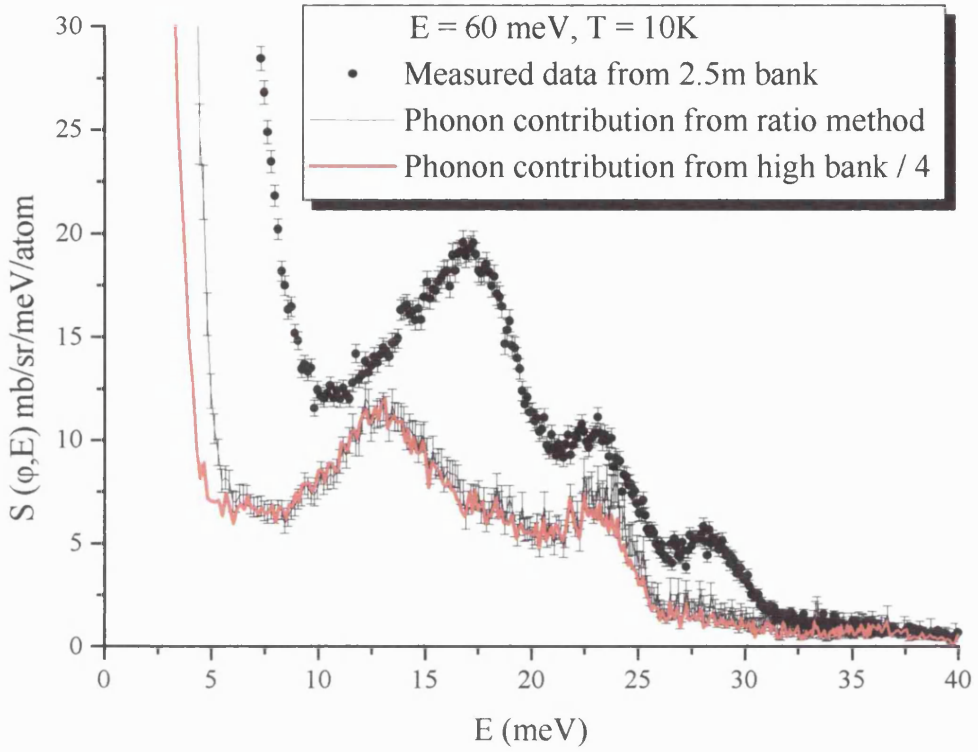

Figure 4.12: The 3 excitations seen in the 35 meV spectrum are also clearly evident at 60 meV incident energy.

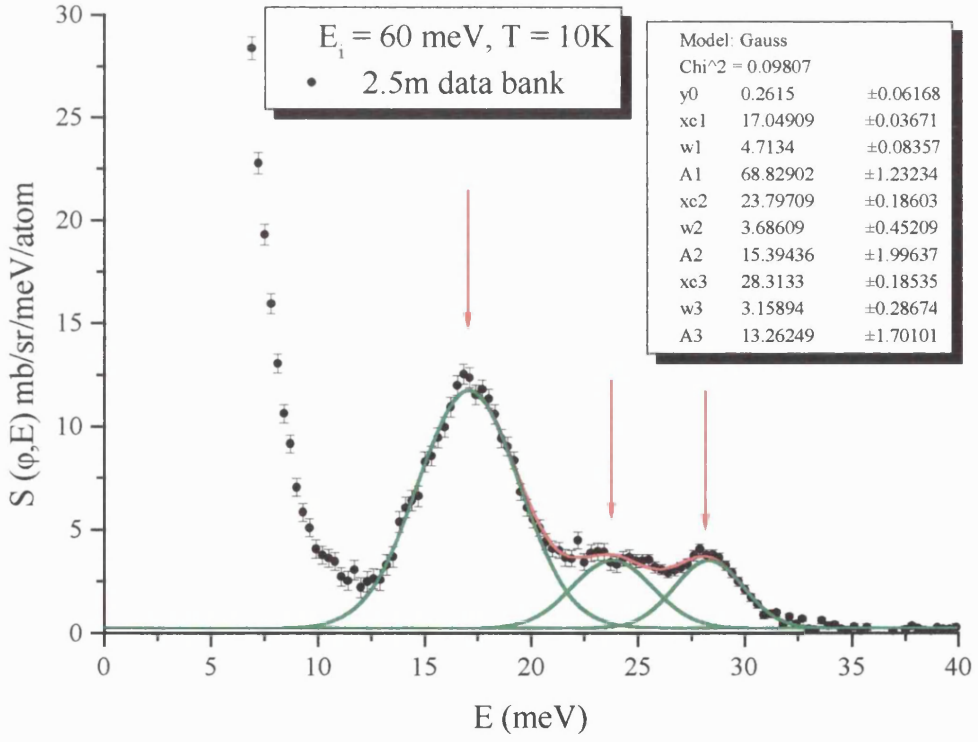

Figure 4.13: Gaussian fit to the 3 highest excitations seen in the 2m bank 60 meV incident energy spectrum. The parameters for each peak are shown in the insert.

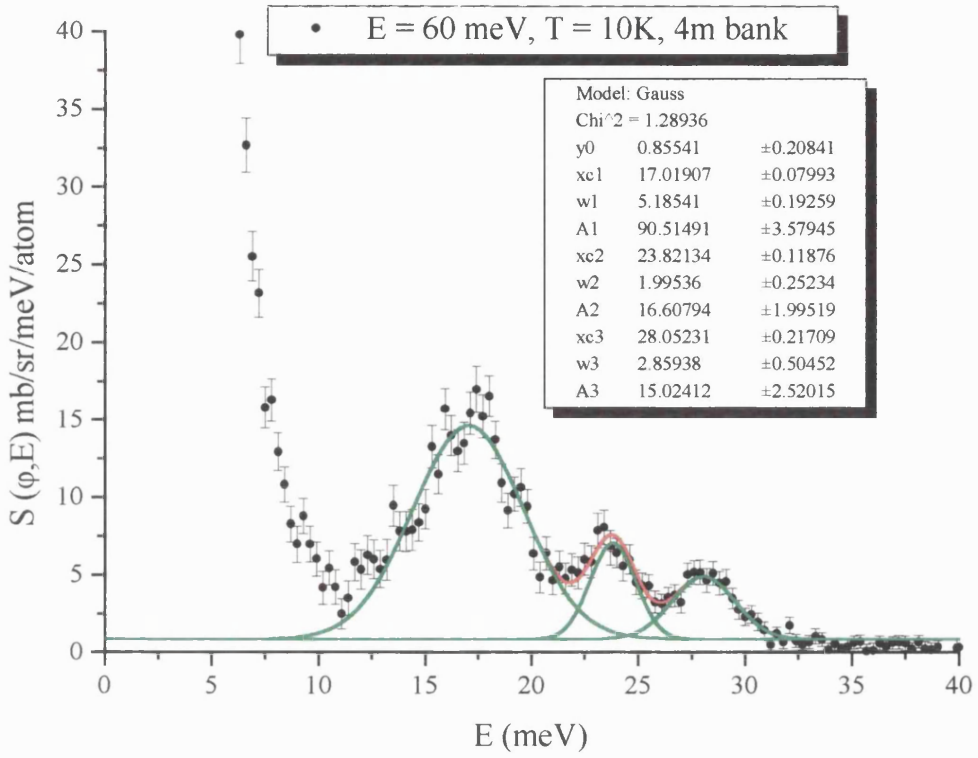

Figure 4.14: The 4m bank corrected data for E_i = 60 meV, which suggests there are 3 excitations visible. In the 2m bank data the excitation at E = 23 meV is very hard to see, and only with this 4m bank data can we confirm its presence.

4.2.2.1 CEF peak fitting summary.

From the available data, 7 CEF excitations have been observed and fitted. Table 4.4 summarises the fits for each incident energy spectrum and for both 2.5 and 4m bank data. It is important to note the inelastic resolution (FWHM, meV) at each excitation for the different incident energies. Figure 4.15 shows the Resolution v Transfer Energy curves for each incident energy used in this experiment. For each observed mode we can see that the FWHM is greater than the instrumental resolution at the respective energy transfer.

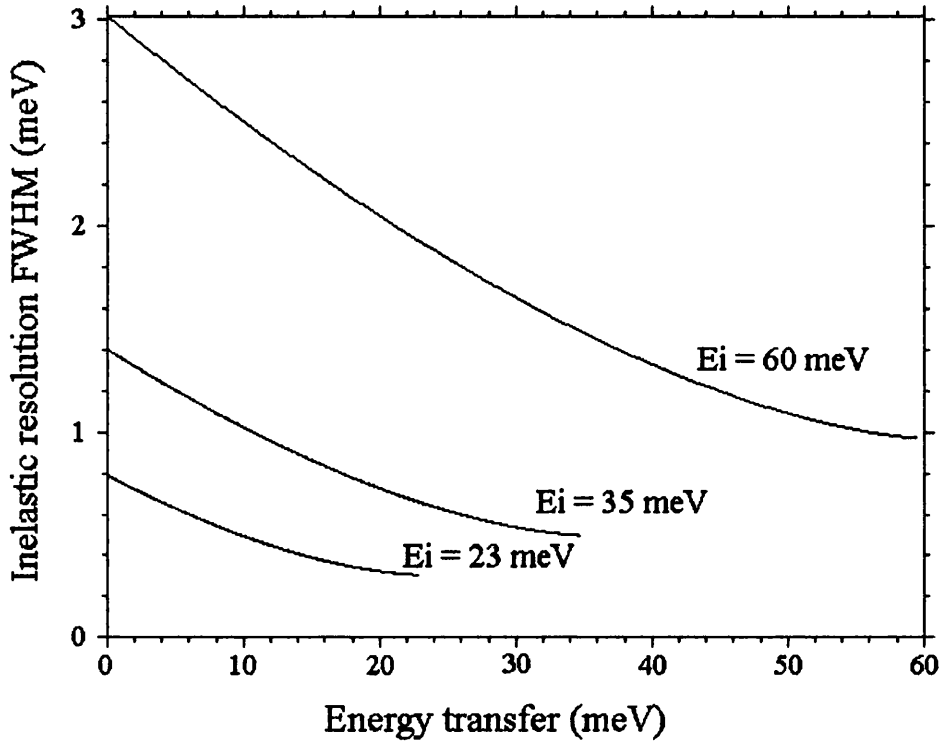

Figure 4.15: Resolution curves for the incident energies of 23 meV, 35 meV and 60 meV. These curves allow us to compare the CEF excitation widths to the instrument resolution.

E_i = 23 meV						E_i = 35 meV					
2.5m bank			4m bank			2.5m bank			4		
E (meV)	W (meV)	A	E (meV)	W (meV)	A	E (meV)	W (meV)	A	E (meV)	W (meV)	A
1.81±0.03	0.94±0.05	32.60±2.91	1.77±0.02	0.84±0.03	47.90±2.20	-	-	-	-	-	-
3.39±0.03	1.45±0.14	51.78±4.77	3.27±0.03	1.08±0.07	51.05±2.59	-	-	-	-	-	-
5.17±0.05	1.07±0.10	21.99±2.82	5.45±0.03	0.92±0.08	24.42±2.01	-	-	-	-	-	-
7.36±0.15	1.57±0.33	6.34±1.15	7.23±0.35	1.64±0.78	5.35±2.18	-	-	-	-	-	-
17.27±0.17	2.79±0.35	10.67±1.25	17.49±0.21	1.19±0.43	4.56±1.48	17.13±0.04	2.94±0.09	25.68±0.89	17.36±0.06	2.73±0.15	25.69±1.74
						22.98±0.13	1.90±0.29	3.89±0.63	23.29±0.19	2.20±0.46	5.93±1.45
						28.36±0.09	0.89±0.20	1.76±0.38	28.60±0.24	1.07±0.54	1.60±0.85

E_i = 60 meV						Average E (meV)
2.5m bank			4m bank			
E (meV)	W (meV)	A	E (meV)	W (meV)	A	
-	-	-	-	-	-	1.78±0.02
-	-	-	-	-	-	3.33±0.02
-	-	-	-	-	-	5.38±0.03
-	-	-	-	-	-	7.34±0.14
17.05±0.04	4.71±0.08	68.82±1.23	17.02±0.08	5.19±0.20	90.51±3.58	17.17±0.02
23.78±0.19	3.69±0.45	15.39±2.00	23.82±0.11	2.00±0.25	16.61±2.00	23.49±0.07
28.31±0.19	3.16±0.29	13.26±1.70	28.05±0.22	2.86±0.50	15.02±2.52	28.34±0.07

Table 4.4: Energy, FWHM, and Area of the peak calculated from the Gaussian fits to the excitations in the E_i = 23, 35 and 60 meV 2m and 4m bank data at T = 10 K. The weighted mean of the Energy is then calculated for each excitation.

4.2.3 Intermultiplet results.

The experiment at HET also allowed us the opportunity to search for intermultiplet transitions. With an incident energy of 800 meV we see three peaks, at T = 10 K. Fitting these to Gaussian form [Figure 4.16] and comparing the results to free Pr-ion and metal Pr [Table 4.5], the $^3H_5$ and $^3F_2$ transitions are evident. The middle peak at E = 367 meV does not match to any known transition. However, we can treat this peak as an instrumental artefact because of its occurrence in other data taken on HET.

	Free ion	Pr metal	PrNiSn
$^3H_5$	266.8	261	263
$^3H_6$	544.1	-	-
$^3F_2$	619.5	578	577
$^3F_3$	795.4	747	
$^3F_4$	849.9	809	
$^1G_4$	1230.0	-	

Table 4.5: Experimental energies (meV) of intermultiplet transitions for the Pr free ion, Pr metal, and PrNiSn. Values have been taken from A. D. Taylor *et al* [1988] for the free ion and Pr metal, and from Figure 4.16 below for PrNiSn.

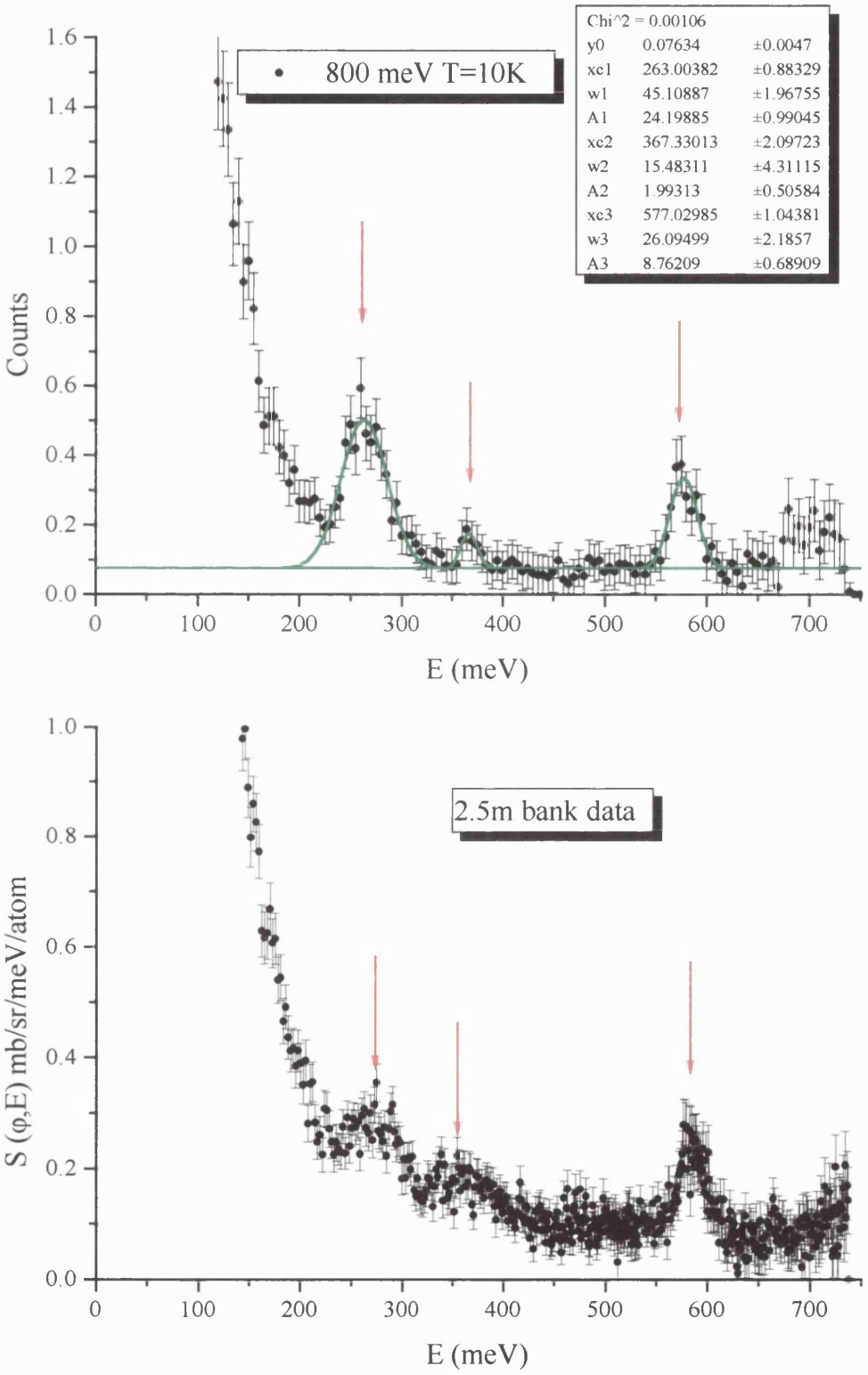

Figure 4.16: Inelastic scattering with an incident energy of 800 meV shows 2 intermultiplet transitions, and a well known anomalous peak at 367 meV. The lines are fits to Gaussian functions, with the parameters given in the inset to the first spectrum. The first spectrum is taken from the 4m bank, and the second spectrum from the 2.5m banks.

4.2.4 FOCUS fit.

It is possible, using the ISIS program FOCUS, to fit to the data to give possible CEF parameters. An interactive CEF parameter fitting package for inelastic scattering data, it is used to determine the crystal field parameters for rare earth compounds. The program can work with all R^{3+}, excluding La^{3+} and Lu^{3+} which show no crystal field splitting, with any of the 32 point symmetries. The crystal field Hamiltonian is calculated using Stevens' operator equivalents, and produces a level scheme, wavefunctions of the levels and relative intensities of the transitions.

The limits of the program are such that fitting can be a tricky process. The current version of FOCUS does not allow multiple spectra fitting; thus the parameters given below are based on a fit to the 5 excitations seen in the 23 meV data only. Therefore the highest levels predicted tend not to match exactly the observed excitations seen in the scans with transfer energies of 35 meV and 60 meV. The fit may also become unstable very quickly, generating CEF parameters that may have no physical meaning.

4.2.5 FOCUS analysis and results.

Once the rare earth ion has been identified, along with the point symmetry, the user has to input several parameters. These include the temperature of the sample, the angle of the detector bank, applied field, and the incident energy. These can then be fixed at their known value. For PrNiSn, which has the D_{2h} point symmetry, there are a total of 26 parameters for the data set, including 9 CEF parameters and the parameters mentioned above.

A list of these parameters is given below, in the format used by the FOCUS program:

Parameter set		P	Sigma
1	Temperature (Kelvin)	10.000	Fixed
2	Incoming Energy(meV)	23.000	Fixed
3	Detector angle	19.500	Fixed
4	Bkgd Const (b)	0.60098E-02	Fixed
5	Bkgd slope (b/meV)	0.68108E-03	Fixed
6	Elastic Int (b)	7.7799	Fixed
7	Elastic pos (meV)	-0.23067E-01	Fixed
8	Elastic FWHM (meV)	1.3501	Fixed
9	Quasielas FWHM (meV)	0.53000	Fixed
10	Inelastic FWHM (meV)	1.3501	Bound to para 8
11	Intensity factor	0.21955	Fixed
12	B_ext(x) Tesla)	0.00000E+00	Fixed
13	B_ext(y) (Tesla)	0.00000E+00	Fixed
14	B_ext(z) (Tesla)	0.00000E+00	Fixed
15	B_mol(x) (Tesla)	0.00000E+00	Fixed
16	B_mol(y) (Tesla)	0.00000E+00	Fixed
17	B_mol(z) (Tesla)	0.00000E+00	Fixed
18	Re B20 (meV)	-0.22490	0.25966E-02
19	Re B22 (meV)	0.38449	0.42007E-02
20	Re B40 (meV)	0.98138E-02	0.10799E-04
21	Re B42 (meV)	-0.17324E-01	0.34174E-03
22	Re B44 (meV)	-0.49382E-01	0.14064E-03
23	Re B60 (meV)	-0.16526E-03	Fixed
24	Re B62 (meV)	-0.10019E-02	Fixed
25	Re B64 (meV)	-0.26544E-02	Fixed
26	Re B66 (meV)	-0.50182E-03	Fixed

These parameters may be fixed, free, bound to each other, or limited between a maximum and minimum. In the case of a magnetically ordered phase, you may also specify the direction of the moment. The general sequence of analysis is to fit the elastic peak and background first. This is easily done if the intensity of the elastic peak is much greater then the CEF excitations.

It is possible for FOCUS to provide a random selection of initial parameters with finite boundaries by Monte-Carlo simulation. This is useful if you have no initial idea of the magnitude of your CEF parameters. But it is possible to estimate starting values from experimental data or from the CEF parameters of similar systems.

4.2.5.1 Method 1: Analysis from YbNiSn CEF parameters.

YbNiSn has the CEF parameters B_2^0 = 0.272 meV and B_2^2 = 0.360 meV [D.T. Adroja *et al*, 1998]. We know from Chapter 1 that $B_l^m = A_l^m \langle r^l \rangle \theta_l^m$, where A_l^m is a crystal field potential, $\langle r^l \rangle$ the radial average of the 4*f* wavefunctions, and θ_l^m the Stevens factor. The Stevens factors are sometimes denoted by α_J, β_J and γ_J for θ_2, θ_4 and θ_6 respectively. These are listed in Table 4.6 for the rare earths, as taken from Jensen and Mackintosh [1991]. We can assume that A_l^m and $\langle r^l \rangle$ are approximately the same for the Pr ion and Yb ion in the RNiSn case for the purpose of the fitting process. This leads us to the conclusion

$$\left[\frac{B_2^0}{\alpha_J}\right]_{Pr} \approx \left[\frac{B_2^0}{\alpha_J}\right]_{Yb},$$

And is also valid for B_2^2. It is therefore possible to estimate from the YbNiSn starting values for PrNiSn: B_2^0 = -0.180 meV and B_2^2 = -0.238 meV.

Rare earth ion	$\alpha \times 10^2$	$\beta \times 10^4$	$\gamma \times 10^6$
Ce	-5.71	63.5	0
Pr	-2.10	-7.35	61
Nd	0.643	-2.91	-38
Yb	3.17	-17.3	148

Table 4.6: Stevens factors for rare earth ions, as taken from Jensen and Mackintosh [1991] pg. 40

Starting with fixing these values for B_2^0 and B_2^2, and freeing the other CEF parameters in stages, before freeing all together for the fit, a level scheme has been produced with wavefunctions for each level.

The fit is shown in Figure 4.17, and the proposed levels in Figure 4.18. It is clear that the 6 lowest levels fit the excitations very well, as expected. But the calculation of the levels does not predict the higher levels to a great accuracy, placing two levels at 30.8 and 37 meV. Returning to the HET data at 35 meV and 60 meV transfer energy spectra, the two highest visible excitations are at 17.24 meV and 27.99 meV. Figure 4.19 shows the fit to the E_i = 23 meV, T = 25 K data using the calculated values from the 10K data. The parameters have been fixed, with only the elastic peak and background parameters allowed to change.

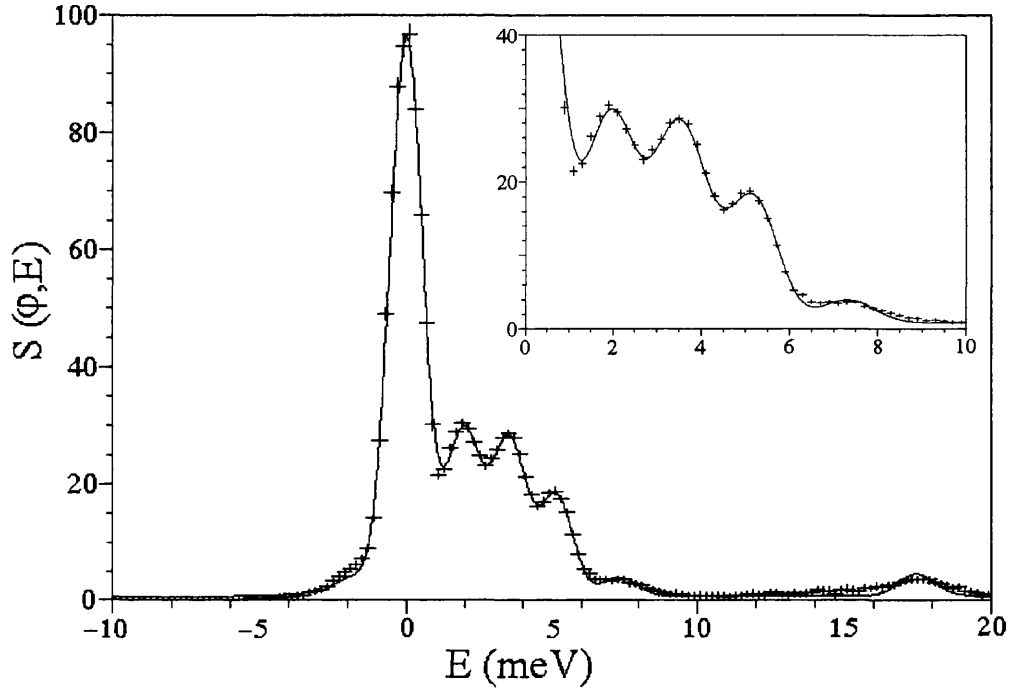

Figure 4.17: CEF FOCUS fit to the 23 meV energy transfer data at T=10 K. There are 5 CEF excitations shown, at approximately 2, 3.5, 5, 7.5 and 17.5 meV. The insert shows the low energy data in detail. See text for a detailed description of the fit.

	meV
B_2^0	-0.466 ± 0.040
B_2^2	-0.340 ± 0.081
B_4^0	(0.788 ± 0.052)E-02
B_4^2	0.010 ± 0.003
B_4^4	-0.026 ± 0.001
B_6^0	(-0.143 ± 0.013)E-03
B_6^2	(-0.596 ± 0.1171)E-03
B_6^4	(-0.165 ± 0.004)E-02
B_6^6	(5.076 ± 0.647)E-04

Table 4.7: CEF parameters in meV, for T = 10 K, produced by the fitting program FOCUS, using the analysis from YbNiSn parameter method.

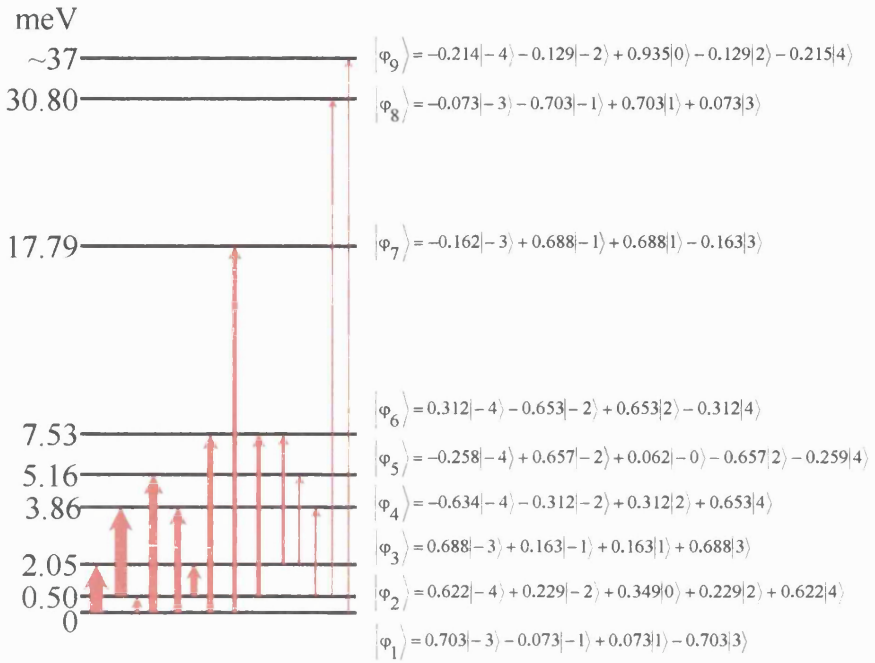

E_{Trans} (meV)	I (barn)
2.05	1.93
3.37	1.55
5.16	1.37
3.86	0.92
1.55	0.64
17.29	0.23
-2.05	0.18
7.53	0.17
17.79	0.14
7.02	0.12
0.5	0.11
-1.55	0.11
5.48	0.07
3.11	0.06
-0.5	0.06
3.37	0.03
30.30	0.02
37.83	0.02

Figure 4.18: Proposed level scheme as predicted by a FOCUS fit to the 23 meV HET data of PrNiSn at 10 K. The arrows indicate possible transitions, with the thickness of each arrow an indication to the relative intensities of each transition. These are detailed in the table. Also shown is the proposed wavefunction for each CEF level.

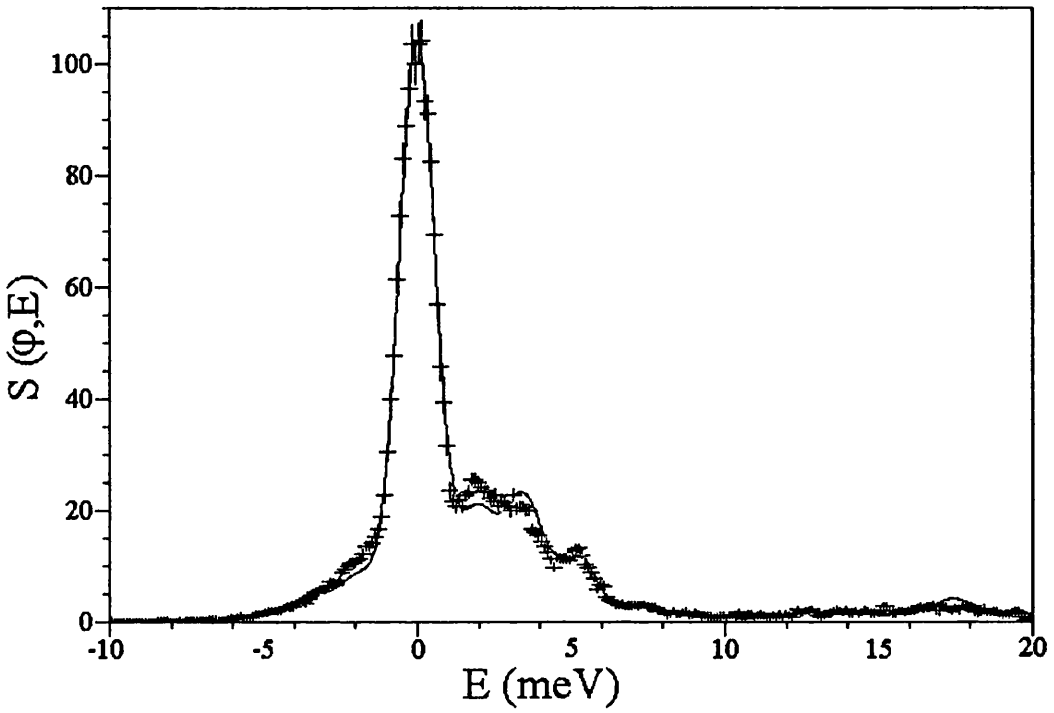

Figure 4.19: Using the calculated CEF parameters at T = 10 K, the fit to the T = 25 K data is shown. The only parameters allowed to change are related to the elastic peak and background.

4.2.5.2 Method 2: Analysis based on the point charge model and molecular field theory.

The second method for estimating starting values for the CEF parameters is based on the point charge model. The crystal field potential may be approximated in the lowest order by the expression

$$V_{CF} = B_2^0\left(3J_z^2 - J(J+1)\right) + B_2^2\left(J_+^2 + J_-^2\right),$$

where J is the total angular momentum. Using this approximation and from the molecular field theory, we can relate the CEF parameters to the paramagnetic Curie temperature along each of the principal axes as

$$\theta_a = \theta_p + \frac{(2J-1)(2J+3)}{10k_B}\left(B_2^0 + B_2^2\right),$$

$$\theta_b = \theta_p - \frac{(2J-1)(2J+3)}{5k_B}\left(B_2^0\right),$$

$$\theta_c = \theta_p + \frac{(2J-1)(2J+3)}{10k_B}\left(B_2^0 - B_2^2\right),$$

where θ_p is the paramagnetic Curie temperature. From the single crystal susceptibility data [Chapter 4.4.2] the values for the Curie temperatures are: θ_p = -18 K, θ_a = -7 K, θ_b = 4 K and θ_c = -52 K. Since $J = 4$ for Pr^+, we can calculate the CEF parameters as B_2^0 = -0.1231 meV and B_2^2 = 0.2574 meV. Using the same FOCUS program and method, the level scheme, wavefunctions and possible transitions are shown in Figure 4.21, with the fit to 10 K data shown in Figure 4.20, and the resulting fit for the 25 K data using the 10 K parameters is shown in Figure 4.22.

	meV
B_2^0	-0.225 ± 0.003
B_2^2	0.384 ± 0.004
B_4^0	(0.981 ± 0.001)E-02
B_4^2	-0.017 ± 0.001
B_4^4	(-0.494 ± 0.001)E-01
B_6^0	(-0.165 ± 0.055)E-03
B_6^2	(-0.100 ± 0.021)E-02
B_6^4	(-0.265 ± 0.004)E-02
B_6^6	(-0.502 ± 0.284)E-03

Table 4.8: CEF parameters in meV, for T=10 K, produced by the fitting program FOCUS, using the analysis of the single crystal magnetic susceptibility data based on the point charge model and molecular field theory.

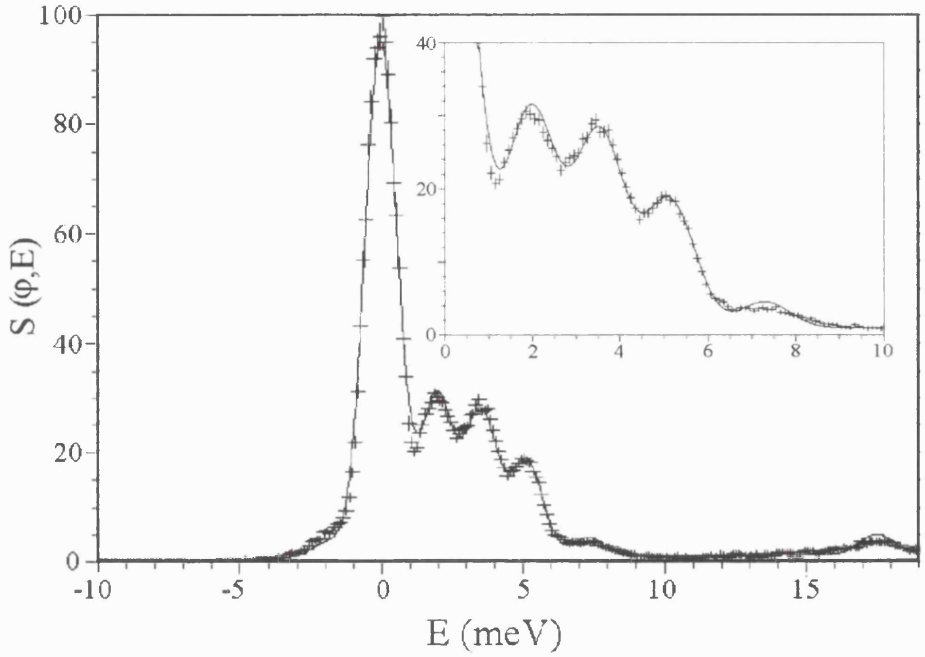

Figure 4.20: CEF FOCUS fit to the 23 meV energy transfer data at T = 10 K using the molecular field method. The insert shows the low energy data in detail.

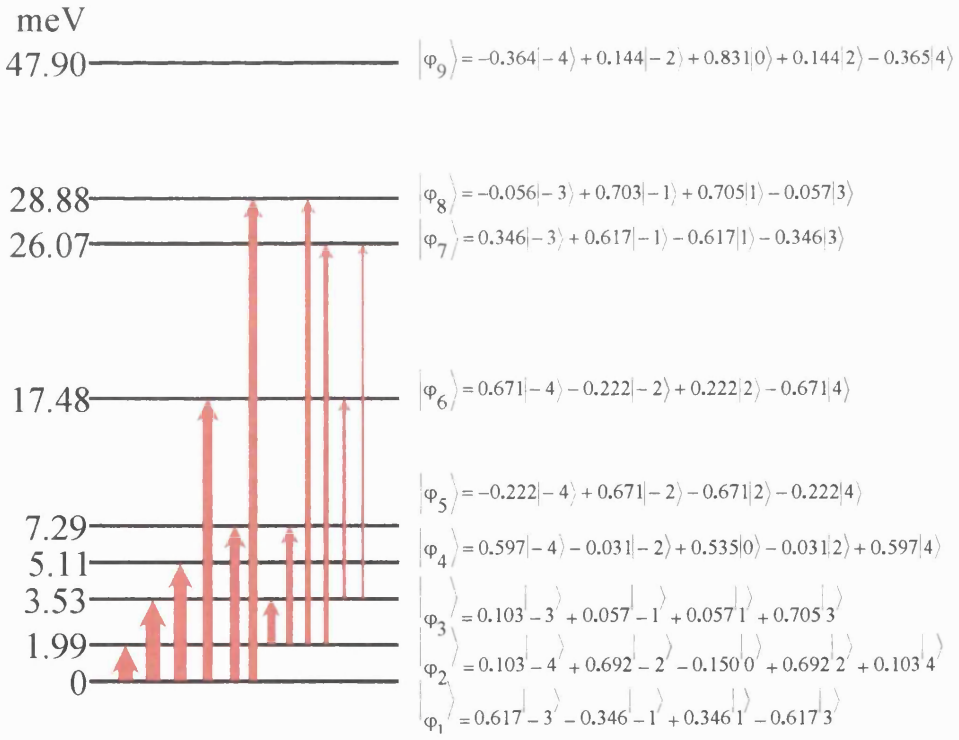

E_{Trans} (meV)	I (barn)
1.99	2.46
3.53	2.29
5.11	1.37
17.48	0.34
7.29	0.32
28.88	0.17
1.55	0.16
5.31	0.14
26.89	0.07
24.08	0.07
13.95	0.02
22.53	0.01

Figure 4.21: Proposed level scheme as predicted by a FOCUS fit to the 23 meV HET data of PrNiSn at T = 10 K. The arrows indicate possible transitions, with the thickness of each arrow an indication to the relative intensities of each transition. These are detailed in the table. Also shown is the proposed wavefunction for each CEF level.

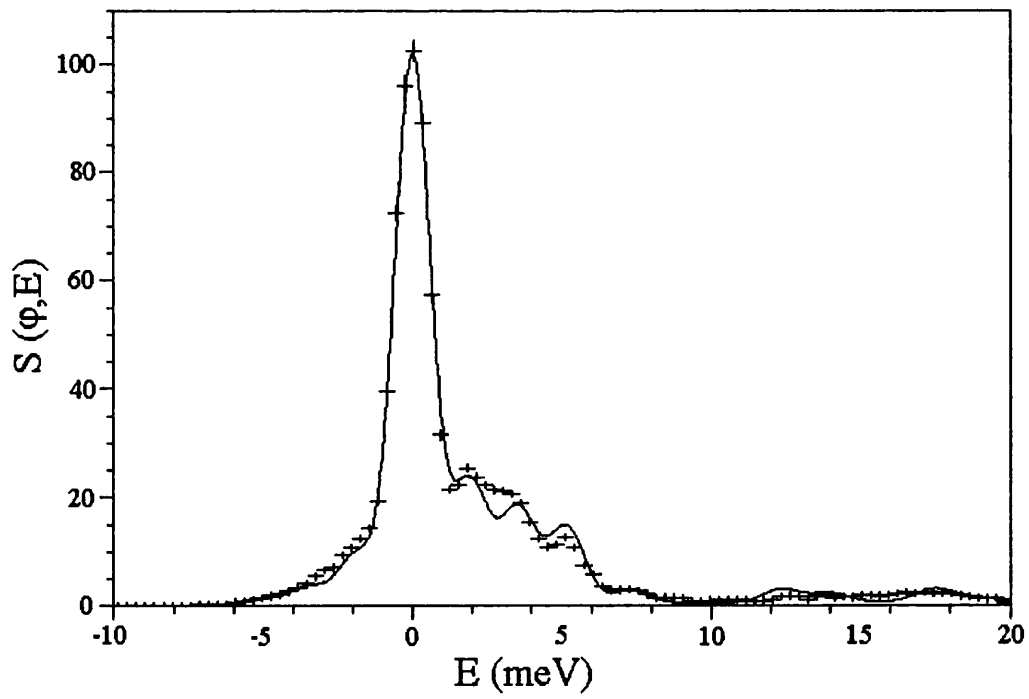

Figure 4.22: Using the calculated CEF parameters at T = 10 K, the fit to the T = 25 K data is shown. The only parameters allowed to change are related to the elastic peak and background.

4.2.6 Conclusion.

From the low energy HET data and FOCUS fits we have produced two possible CEF level schemes for PrNiSn. Each scheme has its basis in different analytical methods and relies on approximations to achieve the starting values for B_2^0 and B_2^2.

The comparisons between each fit and the Gaussian fits to the raw data, are shown in Table 4.9 below. In Section 4.6 I will use both schemes and the CEF parameters to calculate the magnetic susceptibility. This will be an indication of which level scheme may be taken as a good proposal to the real case.

Molecular Field method	YbNiSn method	Weighted Gaussian fit to raw data
0	0	0
	0.5	
1.99	2.05	1.78±0.02
3.53	3.86	3.33±0.02
5.11	5.16	5.38±0.03
7.29	7.53	7.34±0.14
17.48	17.79	17.17±0.02
26.07		23.49±0.07
28.88	30.8	28.34±0.07
47.9	37	

Table 4.9: Comparisons of each method and the weighted fits to the raw data.

4.3 Single crystal inelastic neutron scattering

From the HET data it is clear there are several low-lying CEF states below 10 meV. The aim of the single crystal experiment on V2 is to study the low-lying excitations below 5 meV which show strong intensities. With E_F = 5 meV, the dispersion and polarisation of these modes is presented.

4.3.1 Experimental procedure

The single crystal grown by Dave Fort, used previously for the magnetisation experiment, was cut using the spark eroder perpendicular to the **b** axis, allowing the crystal to be mounted on the $\mathbf{a}^*$- $\mathbf{c}^*$ plane [Figure 4.23]. The collimation was set at 40'-60'-60' and k_F fixed at 1.55 $Å^{-1}$ for the majority of the experiment. This configuration gave us a maximum energy transfer of 5 meV. A standard Orange cryostat was used, with most measurements made at 2 K and 6 K.

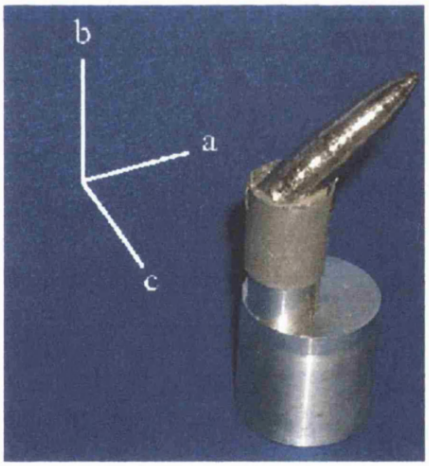

Figure 4.23: PrNiSn single crystal mounted on the **a*-c*** face, perpendicular to the **b** axis. The crystal is attached to the mount with a resin based hardener. Scattering from the adhesive is prevented by wrapping the base of the crystal with cadmium, as shown. The principal axes are demonstrated.

4.3.2 Results at T = 6 K

4.3.2.1 [0 0 q]

It is immediately evident at 6 K that the low energy spectrum is dominated by 2 main modes at 2.4 meV and around 3.5 meV along the [001] direction [Figure 4.24]. It is interesting to note that there is a low-lying excitation at around 0.5 meV. This was not seen in the polycrystalline data from HET due to the width of the elastic peak. As previously noted, fitting to the HET data using the program FOCUS predicts a low CEF energy level at E = 0.49 meV. The appearance of a small peak near this energy gives credence to the level scheme predicted.

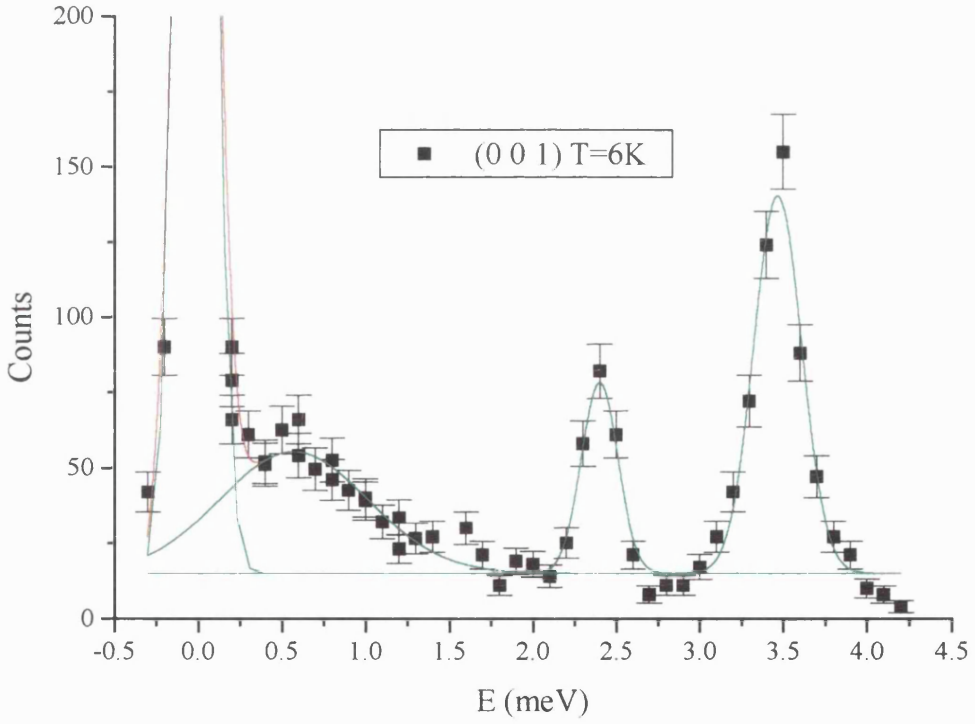

Figure 4.24: Inelastic scattering at T = 6 K for the wave vector (001). The lines are fits to Gaussian functions. Each point is taken over a counting time of approximately 8 minutes.

As we move away from (001) along [00q], the 2.4 meV excitation shows no discernible dispersion. Unlike the 2.4 meV mode, the excitation around 3.5 meV demonstrates a pronounced dispersion along $\mathbf{c}^*$.

Figure 4.25 shows that there are 2 modes in this energy range and are clearly seen as we move from (001) to (003). Each mode may be fitted to a Gaussian [Table 4.10] and the dispersion deduced from these fits [Figure 4.26]. The upper mode dispersion may be fitted to the form $E(\mathbf{q}) = E_0 + J_1 \cos(q\pi)$, shown in Figure 4.26 with the parameters given in Table 4.11. Note that the periodicity of the dispersion reflects the strong interactions between Pr atoms, which are separated by c/2 in the crystal unit cell. It is clearly evident however [Figure 4.26] that the lower mode does not fit to the same dispersion, but to $E(\mathbf{q}) = E_0 + J_1 \cos(q\pi) + J_2 \cos(2q\pi)$ instead.

The additional term of $J_2 \cos(2q\pi)$ indicates the existence of next-nearest neighbour interactions, not seen in the upper mode. The parameters for this fit are again given in Table 4.11.

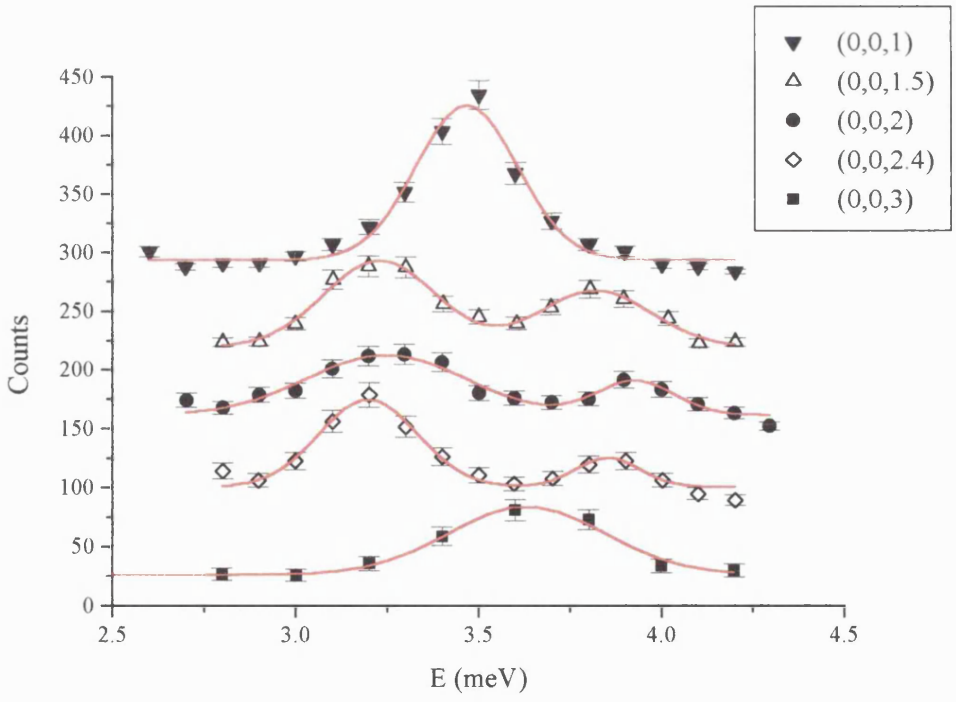

Figure 4.25: Inelastic scattering at T = 6 K for a series of wave vectors between (001) and (003). Each data set is offset by 70 counts (for 1E6 monitor counts) for clarity and the lines are fits to Gaussian functions.

q	E_1 (meV)	A_1 (counts)	W_1 (meV)	E_2 (meV)	A_2 (counts)	W_2 (meV)
1	3.468±0.007	44.95±2.82	0.277±0.016			
1.1	3.454±0.005	46.65±1.72	0.330±0.012	3.75±0.045	2.056±0.91	0.117±0.043
1.2	3.399±0.017	33.02±4.30	0.264±0.034	3.732±0.032	12.09±3.85	0.207±0.056
1.3	3.335±0.007	29.06±1.78	0.284±0.017	3.764±0.012	13.96±1.55	0.237±0.026
1.4	3.247±0.016	22.61±2.70	0.293±0.035	3.778±0.024	14.81±2.70	0.296±0.053
1.5	3.230±0.009	28.10±2.82	0.306±0.023	3.820±0.014	18.29±2.79	0.305±0.034
1.6	3.255±0.013	19.24±3.087	0.235±0.032	3.860±0.021	12.04±3.14	0.240±0.052
1.7	3.222±0.01	22.27±3.117	0.322±0.032	3.883±0.011	14.29±2.43	0.251±0.031
1.8	3.226±0.011	21.30±2.247	0.284±0.025	3.864±0.014	11.94±1.92	0.237±0.034
1.9	3.216±0.010	23.93±2.480	0.319±0.027	3.909±0.013	12.79±1.96	0.245±0.031
2	3.249±0.018	26.89±4.37	0.421±0.051	3.927±0.023	7.39±2.25	0.208±0.054
2.4	3.199±0.012	25.16±3.40	0.270±0.031	3.854±0.028	5.54±2.41	0.176±0.072
2.6	3.236±0.005	28.54±1.65	0.289±0.013	3.789±0.014	8.81±1.51	0.273±0.035
2.8	3.400±0.015	29.58±3.14	0.293±0.029	3.775±0.030	11.27±2.88	0.245±0.053
3	3.630±0.015	16.17±1.61	0.439±0.038			

Table 4.10: Area under the curve, FWHM and energy positions for the two modes around 3.5 meV along the (00q) direction, fitted to Gaussian curves.

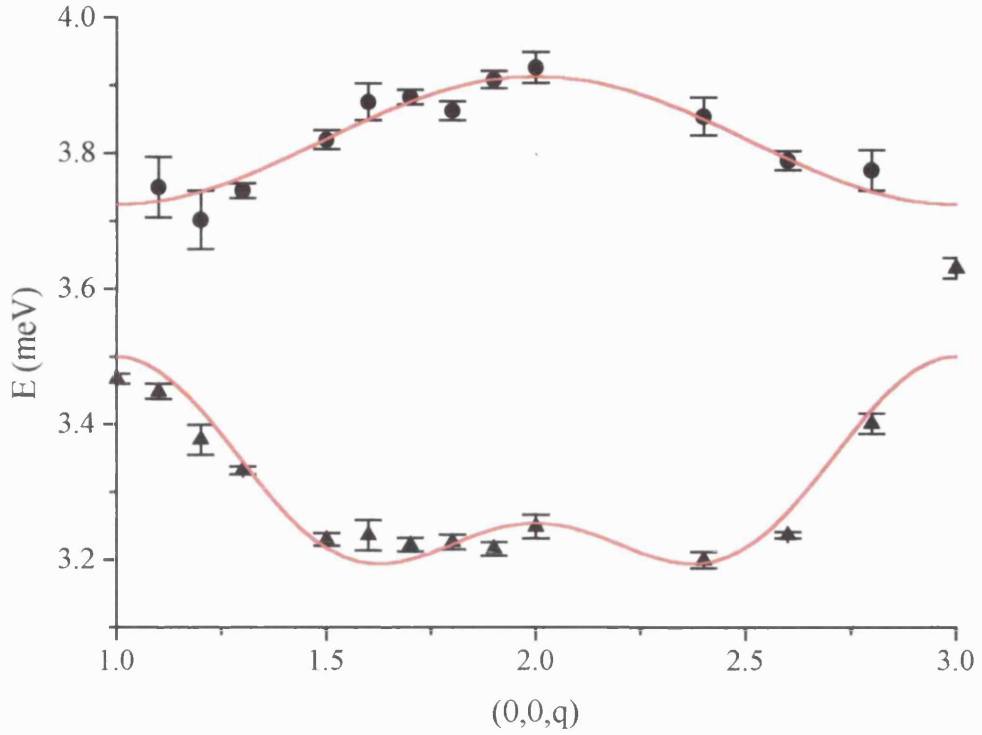

Figure 4.26: Dispersion of the two modes around 3.5 meV, between (001) and (003). The lines represent a fit to the functions described in the text and Table 4.11.

	Upper Mode (meV)	Lower Mode (meV)
E_0	3.820±0.007	3.298±0.013
J_1	0.094±0.010	-0.123±0.018
J_2	--	0.08±0.018
χ^2	0.00056	0.00236

Table 4.11: Dispersion coefficients of the equations detailed in the text, $E(\mathbf{q}) = J_0 + J_1 \cos(q\pi)$ and $E(\mathbf{q}) = E_0 + J_1 \cos(q\pi) + J_2 \cos(2q\pi)$

In the case of the lower mode, the magnitude of J_1 is larger than for the upper mode, whilst J_2 is some two-thirds that of J_1. We can attribute these two modes to acoustic and optic modes of the excitation to the crystal field state at 3.5 meV, where the upper mode is the optic, and the lower mode is the acoustic. We may fit the 2 modes to this particular form because of the dispersion of magnetic excitations in a singlet ground state.

These excitations take the form

$$E(\mathrm{q}) = \left[\Delta\left(\Delta - 2\eta_{01}M_{\alpha}^{2}\left\{J_{\alpha\alpha}(\mathrm{q}) \pm J'_{\alpha\alpha}(\mathrm{q})\right\}\right)\right]^{1/2}$$

Equation 4.1

where Δ is the energy difference, n_{01} the population difference, and M_{α} is the matrix element of J_{α} between the two states.

In the limit $2\eta_{01}M_{\alpha}^{2}\left\{J_{\alpha\alpha}(\mathrm{q}) \pm J'_{\alpha\alpha}(\mathrm{q})\right\} << \Delta$, we can approximate the dispersion to the form

$$E(\mathrm{q}) = \Delta - \frac{\eta_{01}M_{\alpha}^{2}\left\{J_{\alpha\alpha}(\mathrm{q}) \pm J'_{\alpha\alpha}(\mathrm{q})\right\}}{\Delta}$$

Equation 4.2

where $J_{\alpha\alpha}(\mathbf{q})$ is the Fourier transform of the intra-sublattice exchange and $J'_{\alpha\alpha}(\mathbf{q})$ is the Fourier transform of the inter-sublattice exchange. [Jensen & Machintosh, 1991, pg 314].

We can therefore relate Equations 4.1 and 4.2 to the calculated coefficients J_1 and J_2 by

$$J_1 = J_{1\alpha\alpha} \pm J_1'_{\alpha\alpha} \text{ and } J_2 = J_{2\alpha\alpha} \pm J_2'_{\alpha\alpha}$$

Thus,

$$J_{\alpha\alpha}(\mathbf{q}) = J_{1\alpha\alpha}\cos(\mathbf{q}\pi) + J_{2\alpha\alpha}\cos(2\mathbf{q}\pi)$$

and

$$J'_{\alpha\alpha}(\mathbf{q}) = J_1'_{\alpha\alpha}\cos(\mathbf{q}\pi) + J_2'_{\alpha\alpha}\cos(2\mathbf{q}\pi).$$

Note that our parameters J_1 and J_2 include the matrix element and population factors.

Using the coefficients J_1 and J_2 from Table 4.11, we can calculate

$$J_{1\alpha\alpha} = -0.0145 \text{ and } J_1'_{\alpha\alpha} = -0.1085$$
$$J_{2\alpha\alpha} = 0.04 \text{ and } J_2'_{\alpha\alpha} = 0.04$$

From this, we can assume that the nearest neighbours display an antiferromagnetic interaction, while the next nearest neighbours show a ferromagnetic interaction.

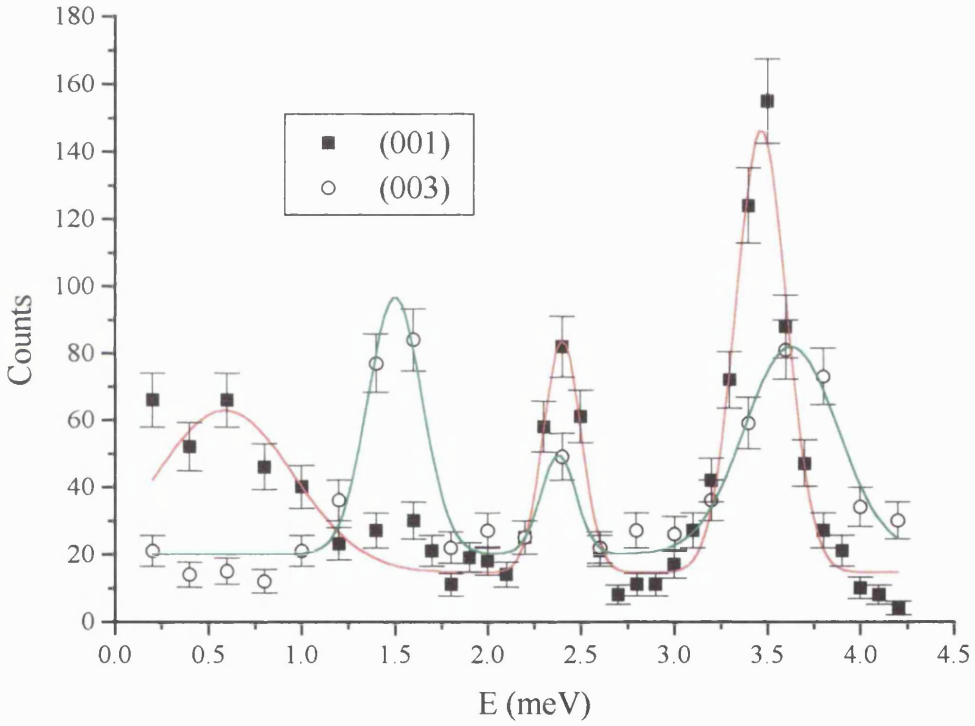

Figure 4.27: Inelastic scattering at T = 6 K for the wave vectors (001) and (003). Each excitation is fitted with a Gaussian function.

From the available data, it also appears that the 0.5 meV mode has a large dispersion over the same range. Although we do not have a complete picture of the dispersion from (001) to (003), at (003) the 0.5 meV mode is not evident. But a sharper mode has appeared at around 1.5 meV. At first glance this excitation may be taken for the shifted 0.5 meV mode, but this is not the case. From the data at (001) at T = 4.8 K, both excitations are present, indicating the 1.5 meV peak is not related to the 0.5 meV mode. The behaviour of the 0.5 meV mode is discussed in greater detail in Section 4.3.3.

4.3.2.2 [q 0 0]

At the wave vector (100) [Figure 4.28], the 2.4 meV mode is much weaker then at (001), indicating it is polarised mostly along **a***. The 0.5 meV and 3.5 meV modes are polarised along the **b*** direction, since they are evident in both spectrums.

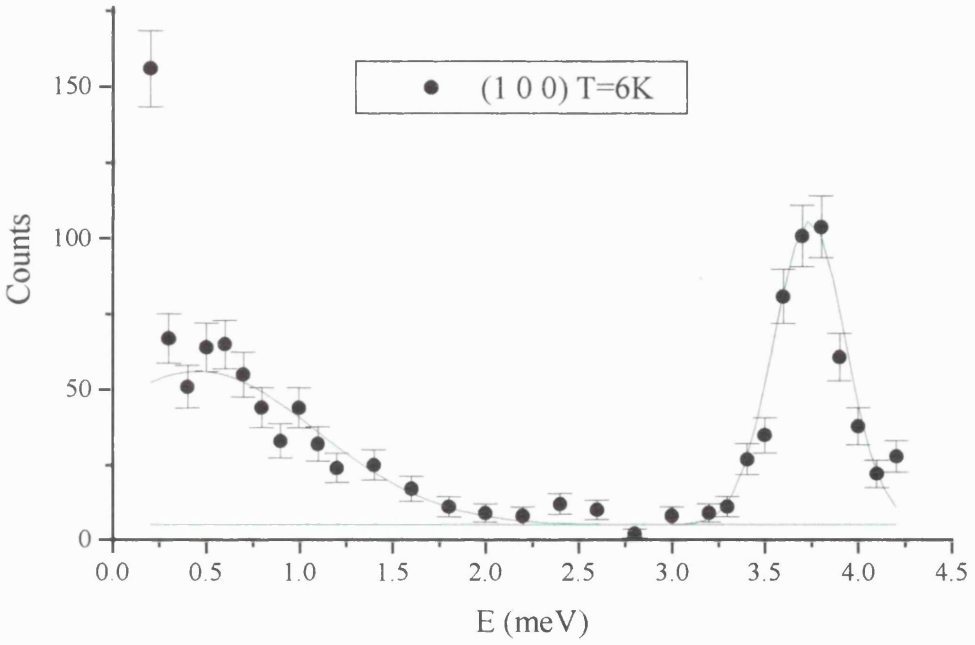

Figure 4.28: Inelastic scattering at T = 6 K for the wave vector (100). Note the 2.4 meV mode seen at (001) is barely evident and the 3.5 meV mode has shifted slightly to 3.75 meV. The 0.5 meV mode is also still evident.

The 3.5meV mode splits again as we move through [q00] [Figure 4.29], but it is only possible to fit this splitting between (100) and (200). The dispersion of the lower mode is similar to the lower mode along [00q], fitting a next-nearest neighbour dispersion rather than that of a nearest neighbour dispersion between (100) and (300). The upper mode however has a small dispersion, splitting at (100) and following the lower mode gradient until (200), where only lower mode is apparent [Figure 4.30].

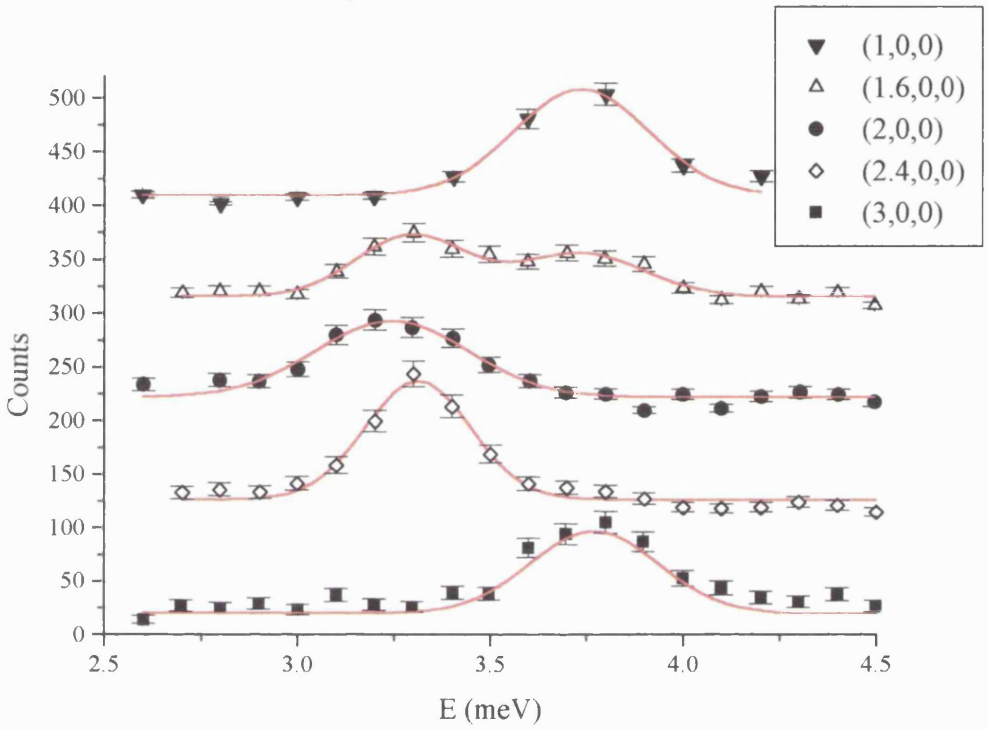

Figure 4.29: Inelastic scattering at T = 6 K for a series of wave vectors between (1 0 0) and (3 0 0). Each data set is offset by 100 counts (in 1E6 monitor counts) for clarity and the lines are fits to Gaussian functions.

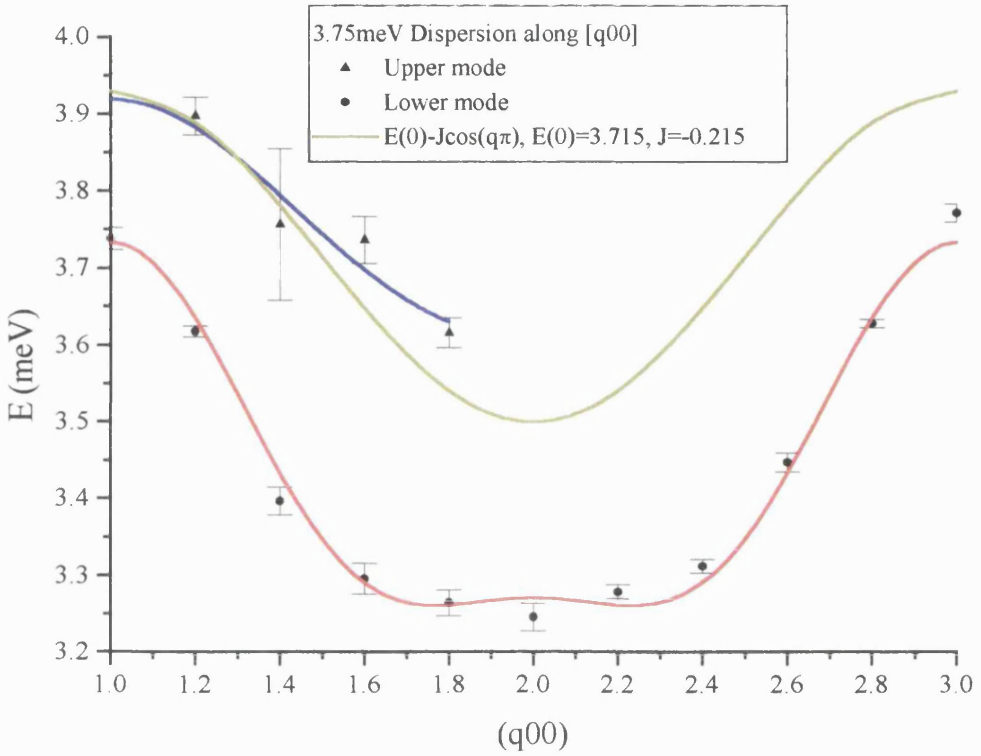

Figure 4.30: Dispersion of the 2 (q00) modes around 3.75 meV. Note the lower mode fits to the equation specified in the text, but the upper mode shows a different form to the upper mode along [00q]. The blue line is a fit to the data, and the yellow line a theoretical curve, both of which are specified in the text.

q	E_1 (meV)	I_1 (counts)	W_1 (meV)	E_2 (meV)	I_2 (counts/)	W_2 (meV)
1	3.74±0.01	48.82±3.16	0.39±0.03			
1.2	3.59±0.03	19.17±4.50	0.28±0.02	3.90±0.03	30.45±3.85	0.53±0.12
1.4	3.41±0.02	17.89±4.39	0.27±0.03	3.77±0.05	19.04±4.83	0.40±0.08
1.6	3.30±0.02	20.25±2.84	0.29±0.04	3.74±0.03	16.16±3.05	0.32±0.05
1.8	3.26±0.02	22.38±2.58	0.35±0.04	3.62±0.02	14.77±1.65	0.30±0.04
2	3.25±0.02	27.74±3.02	0.34±0.04			
2.2	3.28±0.01	38.18±3.27	0.31±0.03			
2.4	3.31±0.01	38.61±2.72	0.27±0.02			
2.6	3.47±0.01	35.76±3.23	0.31±0.03			
2.8	3.63±0.01	31.12±1.41	0.26±0.01			
3	3.77±0.01	31.96±2.61	0.33±0.03			

Table 4.12: Intensity, FWHM and energy positions for the 2 modes around 3.75 meV along the [q00] direction, fitted to Gaussian curves.

	Upper Mode (meV)	Lower Mode (meV)
E_0	3.751±0.021	3.425 ± 0.008
J_1	-0.156±0.034	-0.232 ± 0.011
J_2		0.077 ± 0.011
χ^2		0.0007

Table 4.13: Dispersion coefficients of the equation detailed in the text for (q00), $E(\mathbf{q}) = E_0 + J_1 \cos(q\pi) + J_2 \cos(2q\pi)$.

The upper mode may be fitted to a nearest neighbour form [blue line, Figure 4.30] from (100) to (200), yielding the exchange parameters in Table 4.13. The parameters for the next-nearest neighbour fit to the lower mode are also given in this table.

Again we can attribute the upper mode to an optic dispersion, and the lower mode to an acoustic dispersion. Following the same evaluation as that carried out along [00q], we can determine the exchange parameters to be

$$J_{1\alpha\alpha} = -0.194 \text{ and } J_1'_{\alpha\alpha} = -0.038$$
$$J_{2\alpha\alpha} = 0.0385 \text{ and } J_2'_{\alpha\alpha} = 0.0385$$

Again, the negative numbers show an antiferromagnetic interaction between the nearest neighbours, but it is interesting to note that along [00q] $J_{1\alpha\alpha}$ is smaller that $J_1'_{\alpha\alpha}$, but this is reversed along [q00]. This is not unexpected however, given the change in shape of the optic mode dispersion between directions.

Also note that $J_{2\alpha\alpha}$ and $J_2'_{\alpha\alpha}$ is very similar along both directions.

Given these results, it is possible to determine the relationship between the observed modes and their dispersion along [00q] and [q00]. As previously mentioned, the crystal structure is TiNiSi-type (Pnma space group), giving 4 Pr ions per unit cell. Although the cell is orthorhombic in nature, the site symmetry of each ion is the same. If this was not the case, each site would experience

different crystal fields, yielding different CEF levels within the Pr ion. However, we can see that each Pr ion can be treated identically in this system. Because there are 4 rare earth ions per unit cell, this implies 4 modes should be seen.

If we look at the (00q) case, the 4 modes are visible at 3.50 meV and 3.72 meV at (001) and 3.25 meV and 3.93 meV at (002) [Figure 4.26]. Thus, along the [q00] direction we should observe the connecting branches between these nodes.

The lower mode along [q00] demonstrates one such branch very clearly, connecting the 3.72 meV mode to the 3.25 meV mode [Figure 4.30].

The other branch is harder to resolve, but the small intensity splitting seen between (100) and (200) is most likely to be from the branch between 3.93 meV and 3.50 meV modes. Figure 4.30 shows two lines associated with the upper mode. The blue line is a fit to the available data of the upper mode, whereas the yellow curve is a theoretical branch, connecting the 3.93 meV and 3.5 meV modes, with the form $E(\mathbf{q}) = E_0 + J_1 \cos(q\pi)$, where E_0 = 3.715 meV and J_1 = -0.215 meV (nearest neighbour dispersion).

Comparing the two, it is clear that the fit to the data appears to diverge from the theoretical branch. This is not so surprising. The intensities of the upper mode peaks are small in comparison to the low mode, and because the splitting is smaller than the FWHM of the peaks, the two modes overlap. Thus fitting the upper excitations is difficult since they tend to become lost in the tail of the larger lower mode. It is possible to fit a small peak in most of the spectra at the position given by the theoretical curve, but to some extent you are forcing the fit, and when left alone to fit itself, the small peak will disappear. This may be seen in Figure 4.31. Using the peak position predicted by the theoretical curve, the excitation seen at (2.2 0 0) can be forced to fit two peaks, the highest peak (E = 3.54 meV) being fixed at this energy. For comparison, the single Gaussian fit is

also shown at an offset of 100 counts. The difference in the two fits is plausible, but not sufficient to use these fits as part of the dispersion curve for the upper mode seen in Figure 4.30.

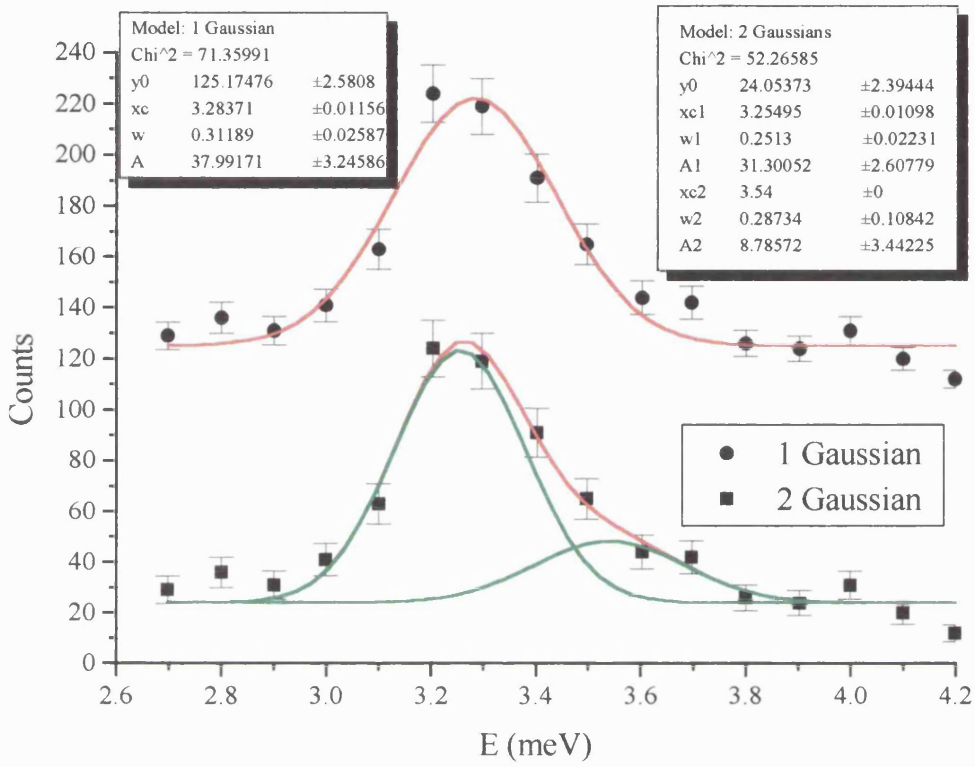

Figure 4.31: Inelastic scattering at T = 6 K for the wave vector (2.2 0 0). The graph shows 2 fits to the same data. The top curve is a single Gaussian fit (offset by 100 counts), allowing all the available parameters to freely move. The bottom curve is the result of a 2 Gaussian fit, where the second Gaussian has been fixed at an energy of 3.54 meV as predicted by the theoretical curve given in Figure 4.30.

4.3.3 Results at T = 2 K

Continuing to look along the [001] direction, we carried out scans at T = 2 K. As seen in Figure 4.30, the 3.5 meV and 2.4 meV modes are still very evident, but there is a large asymmetrical peak upon which they sit. It appears that as the temperature decreases, the 0.5 meV excitation shifts in energy, intensity and shape [Figure 4.32]. Plotting the behaviour of the energy and intensity (area under the curve), it is apparent that there is some transition at about 4.5K [Figure 4.33].

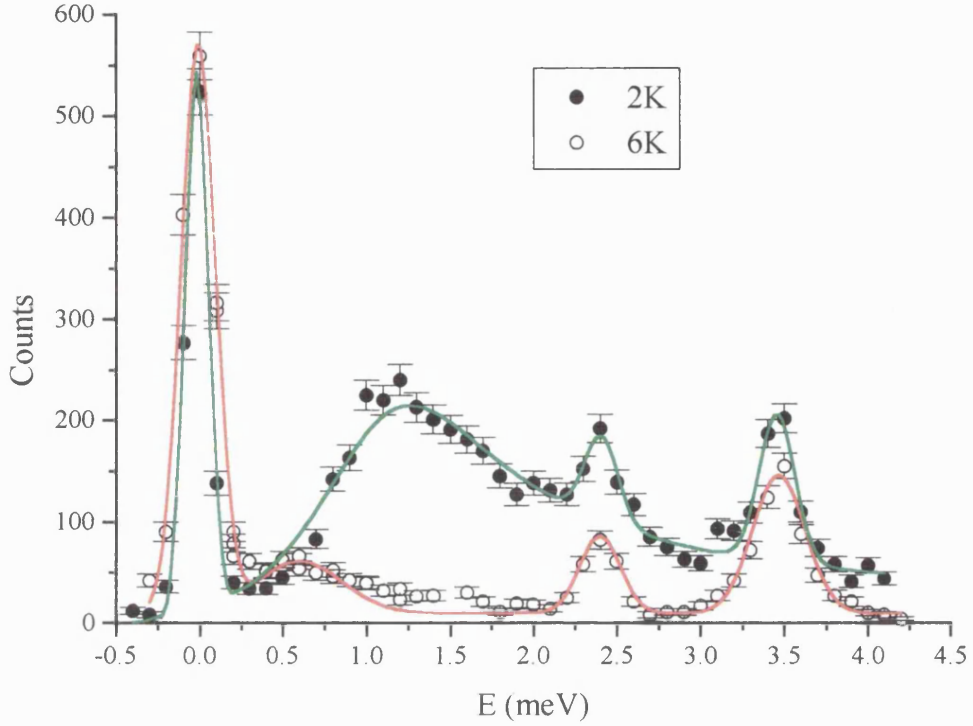

Figure 4.32: Inelastic scattering at T = 2 K & 6 K for the wave vector (001), as detailed in the text.

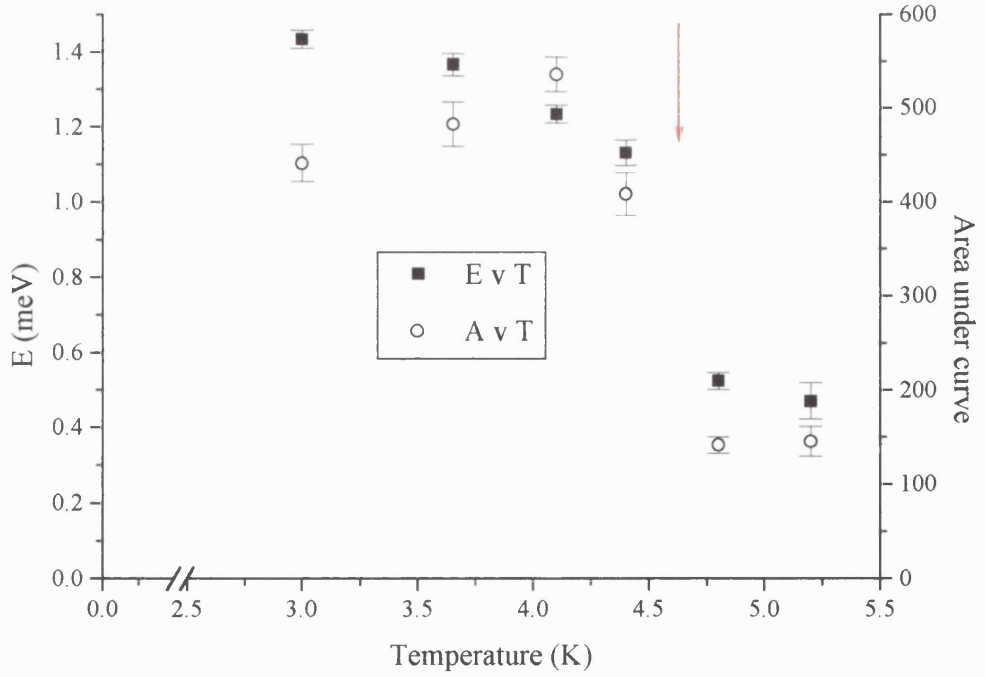

Figure 4.33: Temperature dependency of the Position and Area of the 0.5 meV (T = 6 K) mode at the wave vector (001). There appears to be a transition of some description at about T = 4.5 K (indicated by arrow).

Figure 4.33 clearly shows the proposed transition, but it is also evident that the mode does not disappear above this temperature.

The shape of the mode also changes with temperature. At high temperature, the excitation can be fitted to a Lorenztian function, but as the temperature decreases, the peak becomes more asymmetrical. This is very clear at 2 K [Figure 4.32]. It is possible to fit this asymmetry to a Boltzman dependent Lorenztian, by using the Full Width Half Maximum of the Lorenztian peak at 4.8 K.

As well as a change with temperature, the excitation demonstrates a large **q** dependence at T = 2 K [Figure 4.34]. At the wave vector (003), the peak has shifted in energy to 1.55 meV from 1.1 meV at (001). The intensity of the peak also changes dramatically, doubling in area and height. It is interesting to note that the scan at (0 0 1.4) is very similar to (001) and it is only when we move further along the **c*** direction that we see the large changes.

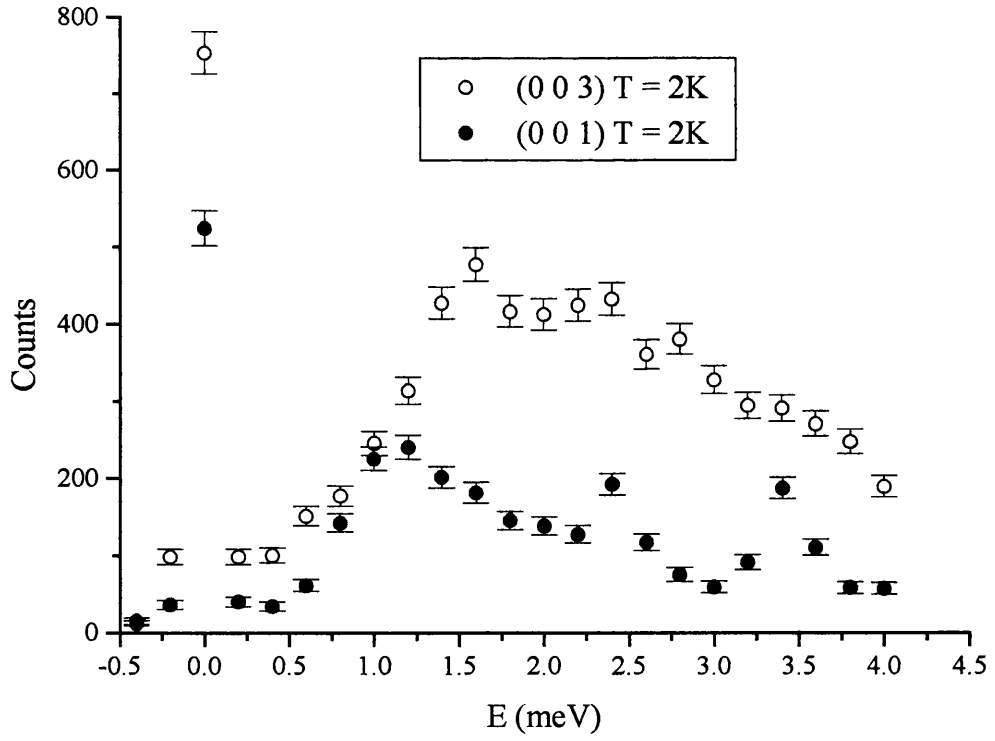

Figure 4.34: Data taken at the wave vectors (0 0 1) and (0 0 3) at T = 2 K.

Although there is no evidence of magnetic ordering from the other experiments detailed elsewhere in this thesis, it is possible that this peak has magnetic origins. We can confirm that there is no ordering in the sample, due to the elastic peaks at 2K and 6K being of the same intensity. But the fact that the large asymmetric peak at low temperature increases in intensity with **q** also suggests that it is not magnetic in origin.

4.3.4 Further investigation at T = 2 K

Since this experiment on V2, further work has been carried out by J. Allen, K. A. McEwen and K. Habicht, on the same single crystal, to determine the nature of this anomalous low-lying peak. It was determined that no low-lying excitation is evident [Figure 4.35] at either temperature of T = 2 K and 6 K at the wave vector (001). Figure 4.36 also shows that there is no low-lying excitation at T = 1.6 K at the wave vectors (001) and (003).

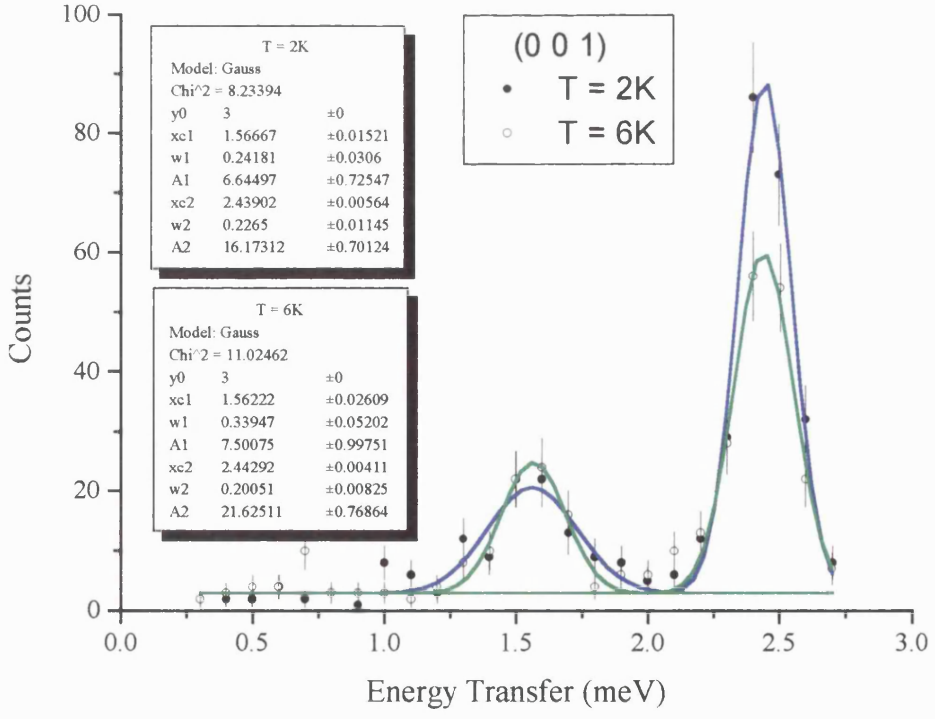

Figure 4.35: Inelastic scattering at T = 2 K & 6 K for the wave vector (001). Each excitation is fitted with a Gaussian function, and the fit parameters described in the inserts [J. Allen *et al* To be published].

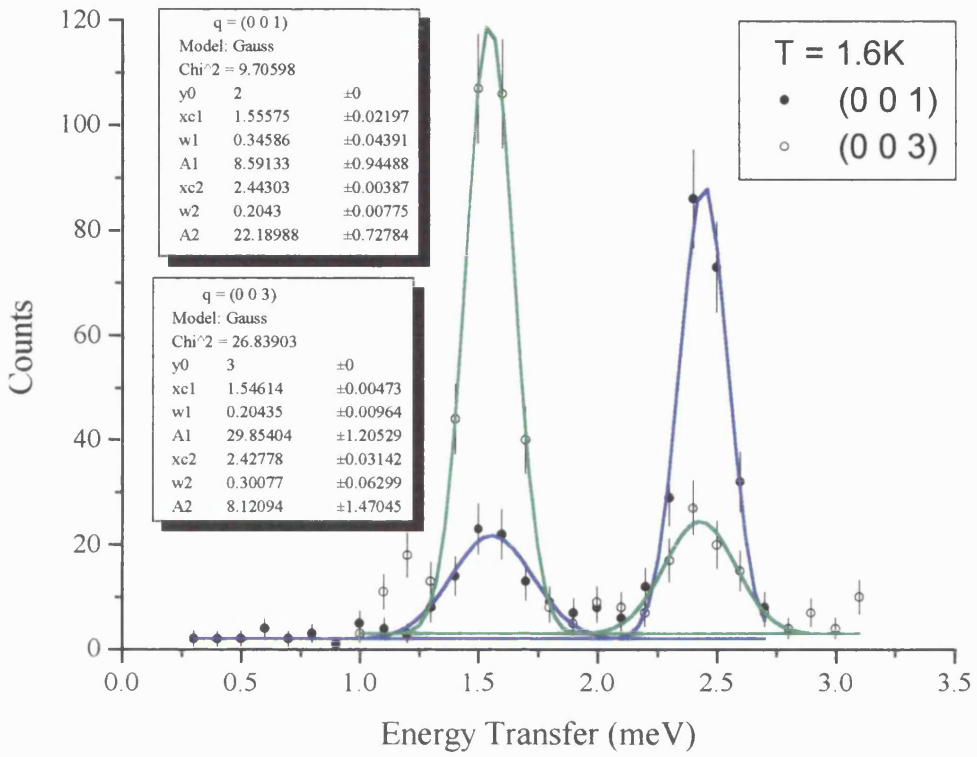

Figure 4.36: Inelastic scattering at T = 1.6 K for the wave vectors (001) and (003). Each excitation is fitted with a Gaussian function and the resulting parameters shown in the inserts [J. Allen *et al* To be published].

It can therefore be concluded that the low-lying excitation observed in the earlier experiment was the result of trapped helium in the cryostat. This is borne out by the apparent transition seen at T = 4.5 K [Figure 4.33].

4.3.5 Conclusions

The 3.5 meV excitation is polarised along **b***, while the 2.4 meV mode is polarised mostly along **c***, and there is a pronounced splitting of the 3.5 meV mode along [00q] and [q00]. The lower modes in both directions fit to a next-nearest neighbour interaction between (001) & (003) and (100) & (300). Along [00q], the upper mode has a nearest neighbour – type interaction between (001) and (003). Along [q00], the upper mode does not fit to either type of interaction, and is only evident between (100) and (200).

It is concluded that there are 4 modes within the 3.5 meV peak. The 2.4 meV mode shows no dispersion over any observed range.

Although the in the initial experiment a low-lying peak at 0.5 meV was observed, further investigation has determined this to be caused by trapped helium in the cryostat. There is no evidence of magnetic ordering from this experiment, confirming results from the magnetic susceptibility and powder diffraction experiments.

4.4 Magnetic susceptibility and magnetisation

Initial magnetisation experiments have been carried out using polycrystalline PrNiSn grown at UCL using a Büler arc furnace, under an argon atmosphere. A small piece of mass ~ 0.1g was spark cut from this button. For the single crystal experiments, a rectangular cuboid with dimensions of 2 - 3mm was spark cut, with each face perpendicular to the principal axes, from the crystal grown at Birmingham.

All measurements have been carried out using a Quantum Design SQUID magnetometer. The sample is moved through two sense coils, producing an output voltage proportional to the current induced in the coils. Normal measurements involve the sample moving through the counter-wound superconducting coils over a distance of 4 cm, usually twice. The sample is mounted in the centre of a 20 cm long plastic straw, ensuring that there is a constant background. The magnetometer can provide fields up to 7 T, within the temperature range 2 K – 300 K.

4.4.1 Polycrystalline results

The susceptibility of PrNiSn has been previously determined by Routsi *et al* (1992), down to a temperature of 4.2 K. Their results show a Curie Weiss temperature θ_{CW} = -10 K and an effective moment of $\mu_{eff} = 3.67\mu_B$, which is very close to the free ion moment of Pr^{3+} ($3.62\mu_B$). They report no evidence of transitions down to 4.2 K.

We have measured the susceptibility of the polycrystalline sample down to 2 K, in an applied field of 300 Oe. There is no evidence of a magnetic transition down to this temperature, confirming Routsi *et al's* results. But there is a change in gradient seen at T = 4.5 K [Inset, Figure 4.37]. It is clear the compound obeys the Curie Weiss law down to 40 K.

Fitting to this law gives θ_{CW} = -18K and $\mu_{eff} = 3.58\mu_B$. Again, the effective moment is close to the theoretical free ion moment for Pr^{3+}, indicating that the majority of the magnetic moment is situated on the rare earth ion, with the nickel and tin contributing little to the total magnetisation.

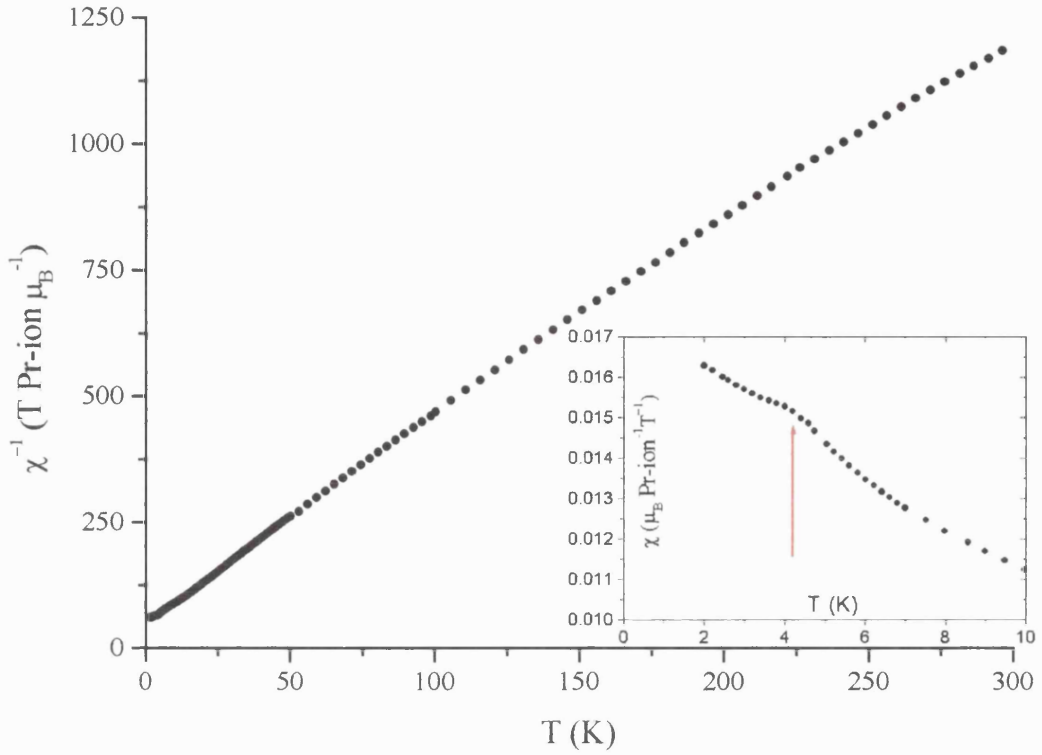

Figure 4.37: The inverse susceptibility per formula unit of polycrystalline PrNiSn, showing Curie Weiss behaviour down to 40 K. The inset demonstrates the susceptibility at low temperature, illustrating the change in gradient seen at T = 4.5 K

4.4.2 Single Crystal results

Single crystal measurements have been carried out along all principal axes. Initial measurements at H = 300 Oe show no magnetic transition to 2 K, but χ_b has a clear local maximum at T = 12K and a local minimum at T = 4.5 K. At T = 2 K the susceptibility is strongly anisotropic [Figure 4.38], with $\chi_a \approx 1.5\chi_b$ and $\approx 4\chi_c$. χ_a drops rapidly with increasing temperature and above T ≈ 13.5 K, the **a** - **b** anisotropy is reversed, $\chi_b > \chi_a$ above this temperature. Both χ_b and χ_c show a distinct upturn below 3 K, which is not evident along the **a**-axis.

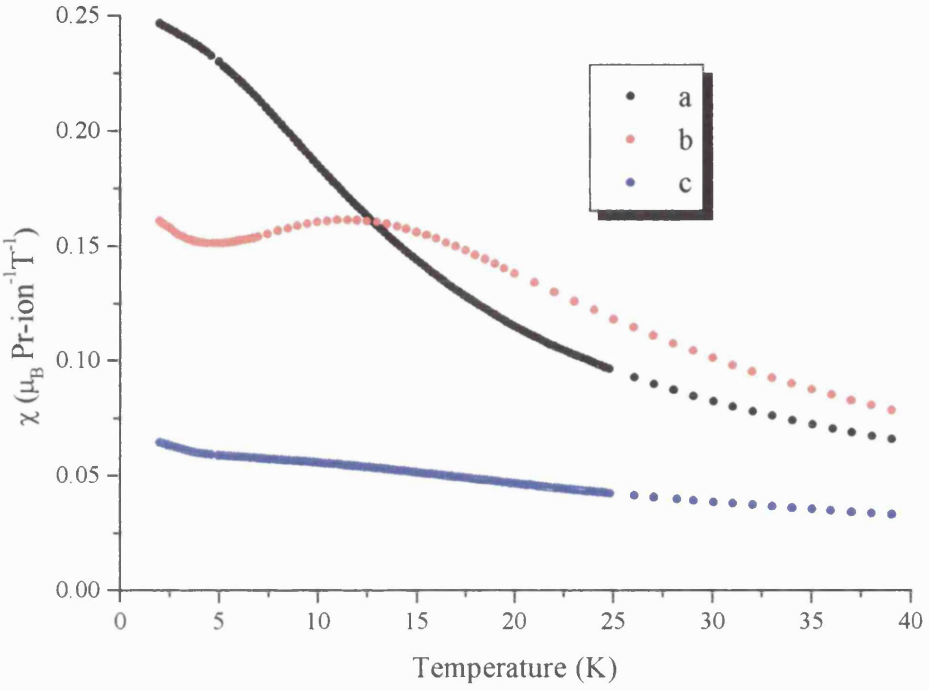

Figure 4.38: Low temperature susceptibility per formula unit for each principal axis in PrNiSn. Note the **c**-axis data have been multiplied by 2 for clarity. The local maximum at T = 12 K and minimum at T = 4.5 K along the **b** axis is clearly illustrated. Each measurement is in an applied field of H = 300 Oe.

It is interesting at this point to note the Curie Weiss dependency of each axis. They all show Curie Weiss behaviour above 50 K, but the anisotropy between each axis is evident in the Curie Weiss temperatures, θ_{CW} = -7.0 K, 4.0 K & -52 K for **a**, **b** and **c** axis respectively [Figure 4.39]. This large difference is a result of the crystal field effects. If one assumes that $\chi_p = 1/3\ (\chi_a+\chi_b+\chi_c)$, the single crystal data fits the polycrystalline Curie-Weiss temperature perfectly. The effective moment per Pr ion for each axis is close to the free ion value, as is seen in the polycrystalline sample, μ_{eff} = 3.743, 3.560 & 3.576 μ_B/Pr respectively. All these values are summarised in Table 4.14.

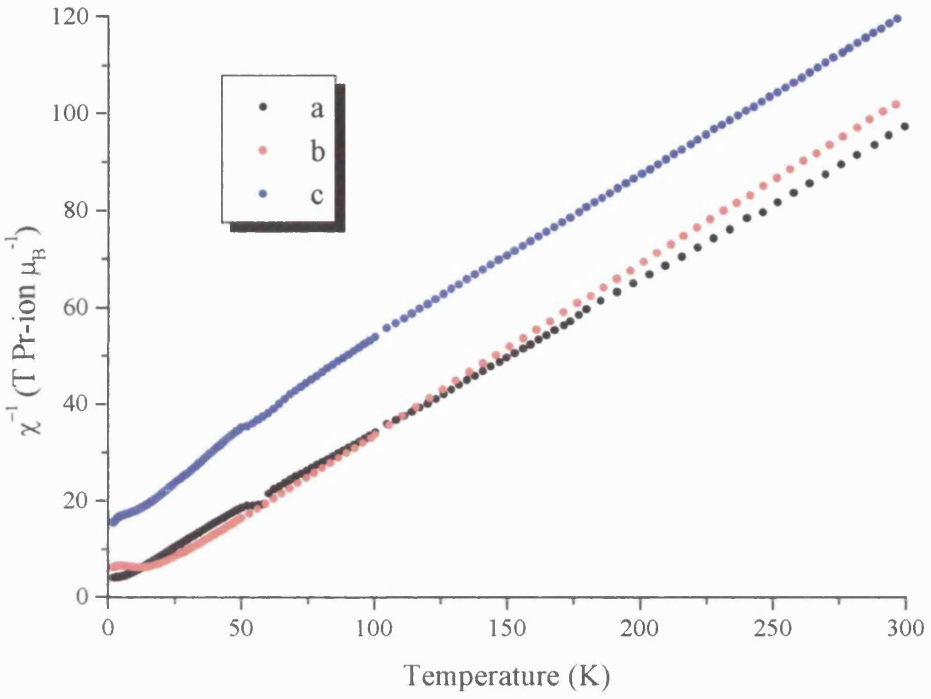

Figure 4.39: Inverse magnetic susceptibilities per formula unit for each principal axis. Curie-Weiss behaviour is evident above T = 50 K.

	A	b	C	polycrystalline
θ_{CW} (K)	-7	4	-52	-18
μ_{eff} (μ_B/Pr-ion)	3.743	3.560	3.576	3.58

Table 4.14: Summary of the values for the Curie Weiss temperatures and effective moments, calculated from the magnetic susceptibility data.

The field dependence of the low temperature **b** axis susceptibility has been carried out, in an effort to determine what effect the field has on the maximum and minimum illustrated along this axis. As is obvious in Figure 4.40, when the field is increased the overall magnetisation also increases. However, it appears that there is no significant magnitude difference between H = 1 T and 2 T, indicating that the full magnetisation of the system along this axis has been reached.

Regarding the maximum at T = 12 K, there is no shift in temperature with increasing field, but the minimum appears to have a slight shift to lower temperatures with higher field, and there is an obvious change in the shape of the minimum at higher fields, especially 2 T. Figure 4.40 also illustrates the reversibility at H = 300 Oe of these gradient changes.

The field dependence of each axis for PrNiSn at T = 2 K, 5 K and 11 K is shown in Figures 4.41 – 4.43. No field transitions are evident at any temperature. Along the **a** axis, the response is linear up to approximately 2 T for each temperature, before beginning to level out. At the applied field of H = 7 T, the response has not yet saturated at any temperature, although the magnetisation at 11 K is less than at 2 K and 5 K. The **b** axis has a similar response, except that the T =11 K data is linear up to H = 7 T and the magnitude of the magnetisation greater that at 2 K and 5 K.

The **c** axis for all three temperatures demonstrates a linear response up to H = 7 T, with similar magnitudes of the magnetisation at 2 K, 5 K and 11 K.

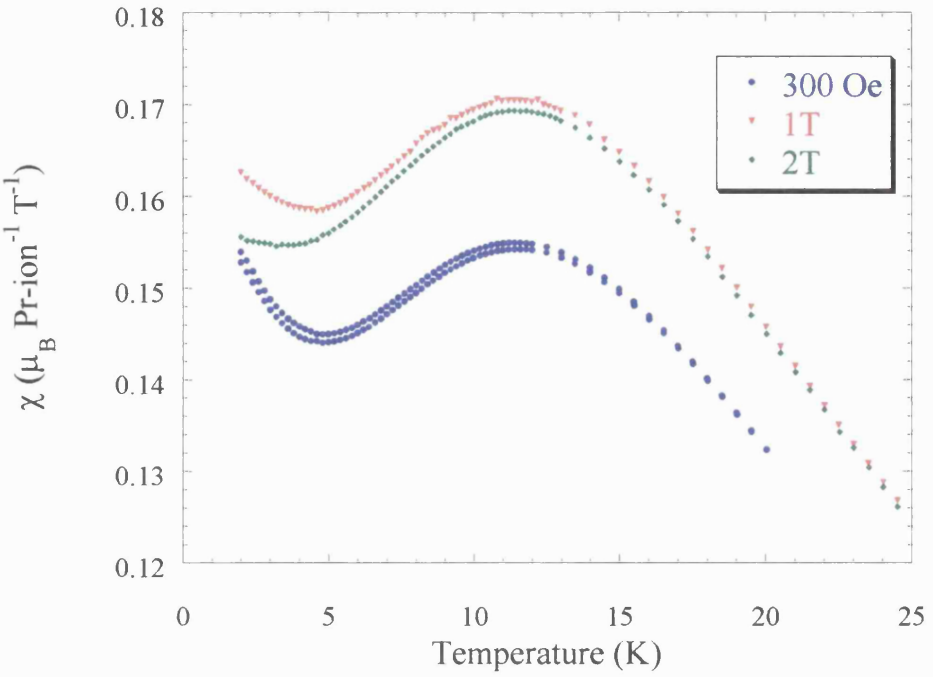

Figure 4.40: **b** axis susceptibility at 3 different applied fields: 0.03 T, 1 T & 2 T. Note the reversibility at H = 0.03 T.

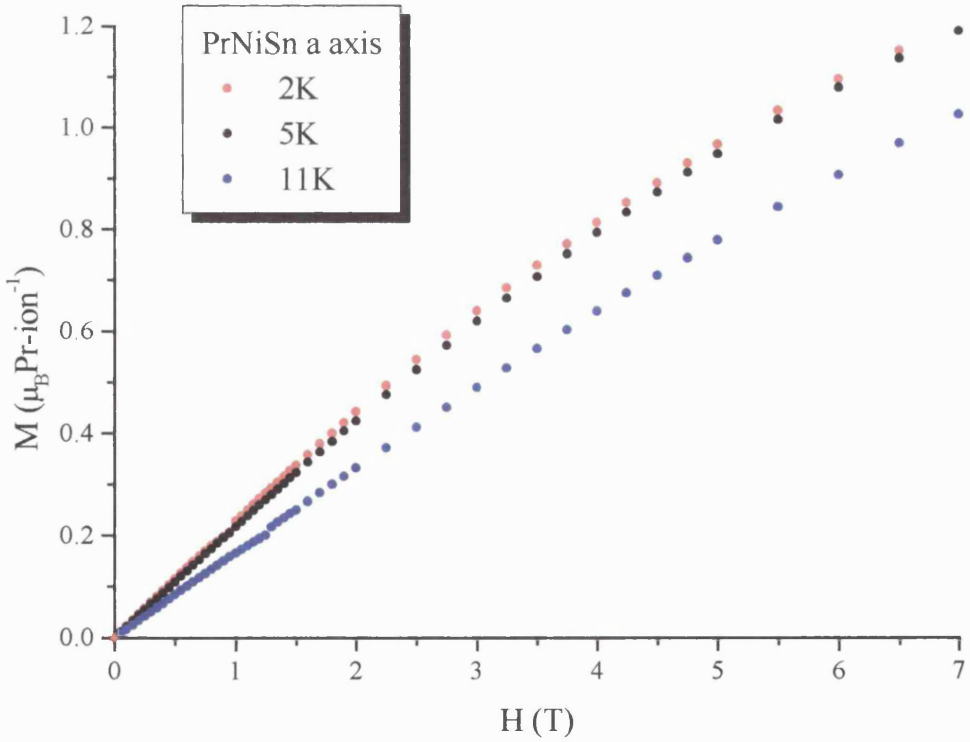

Figure 4.41: The field dependence along the **a** axis at T = 2 K, 5 K and 11 K for PrNiSn.

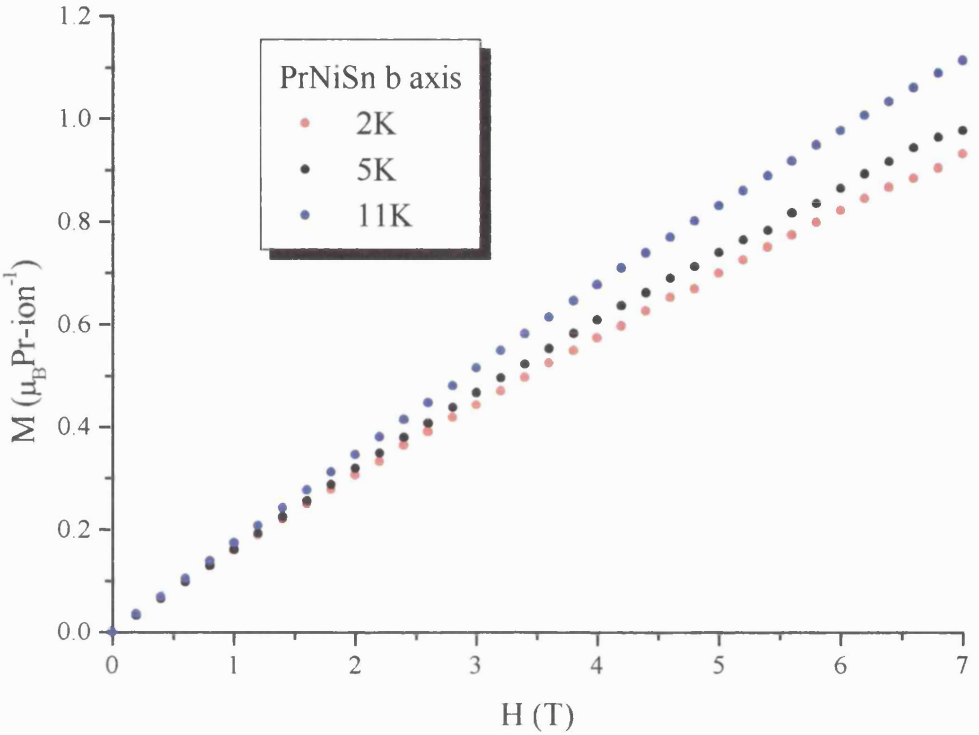

Figure 4.42: The field dependence along the **b** axis at T = 2 K, 5 K and 11 K for PrNiSn.

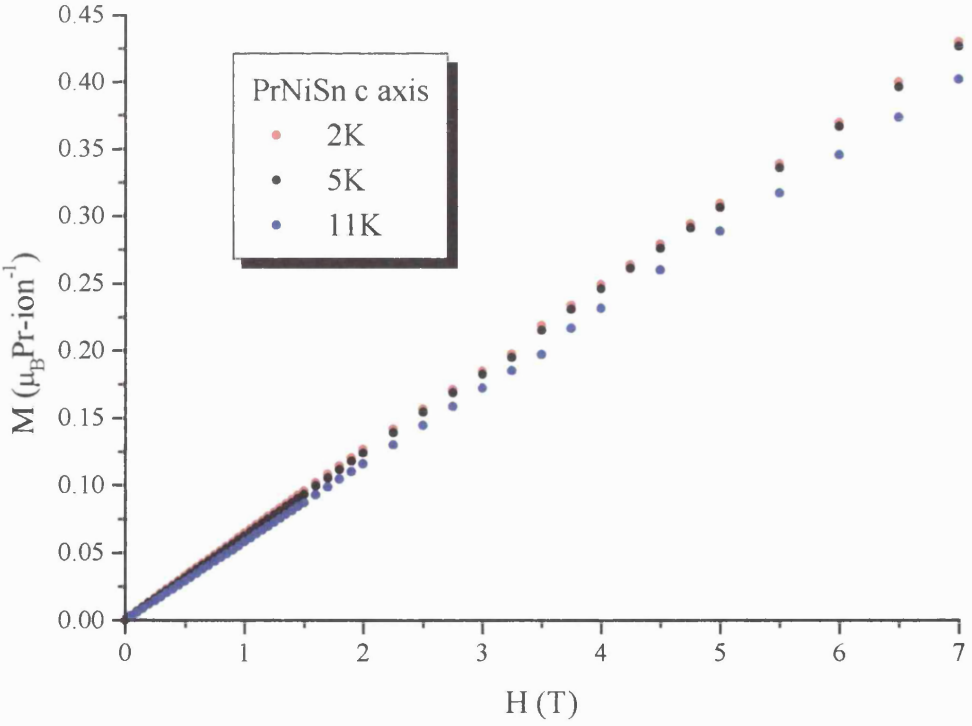

Figure 4.43: The field dependence along the **c** axis at T = 2 K, 5 K and 11 K for PrNiSn.

4.5 Resistivity

The polycrystalline resistivity of PrNiSn was determined both at UCL and the University of Cantabria, Spain, and the results are shown in Figure 4.44. Both samples were mounted in the same way as described in Section 1.3.2, and both samples were cut from the same arc melted button at UCL.

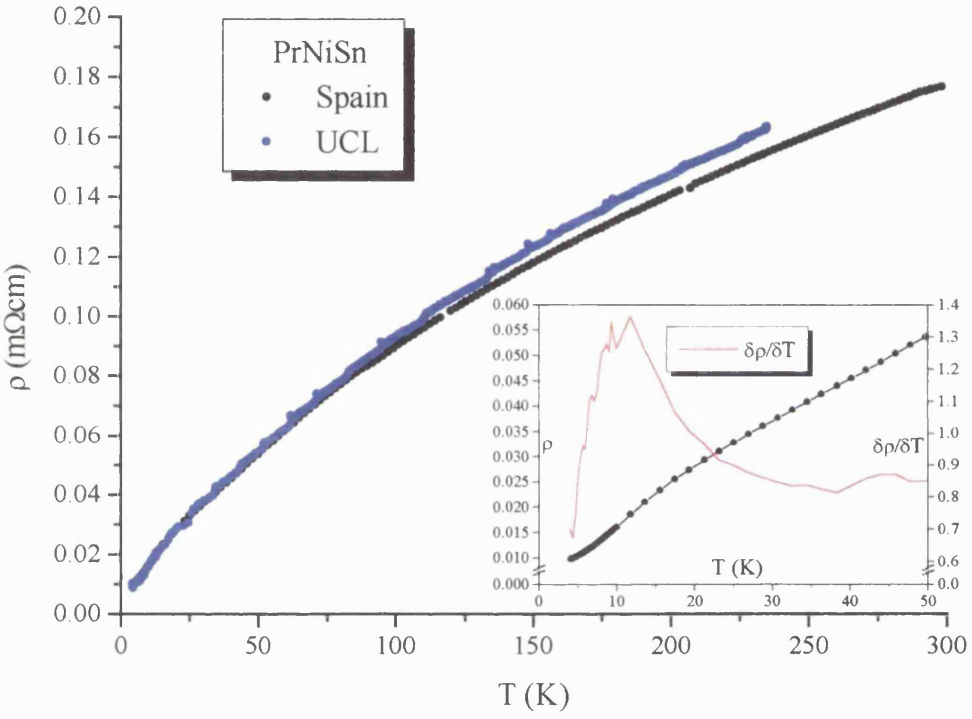

Figure 4.44: The resistivity v temperature for polycrystalline PrNiSn, taken at UCL and Spain (J. Rodríguez, Univ. Cantabria, Santander, Spain). The insert shows the low temperature resistivity and the derivative with temperature.

Both experiments give comparable results, the only difference being a slight deviation at higher temperatures. This may well be due to the rate at which the temperature was changed with time.

Neither experiment indicated any clear transitions down to 4.2 K, confirming there was no magnetic ordering to this temperature. As the inset to Figure 4.44 clearly shows, there is a gradient change to the resistivity at about 12 K. This is seen in the plot of □ρ/□T, in which a peak is observed at this temperature.

4.6 Magnetic Susceptibility Calculation.

I have calculated two possible level schemes for PrNiSn, the first based on established CEF parameters for YbNiSn, the second scheme using the single crystal magnetic susceptibility data from the experiment carried out here at UCL. Both level schemes, when refined by FOCUS, fit to the HET data very well at low temperature (6 K) and low incident energy (23 meV).

An interesting feature of the results from the first method is the proposed CEF level at E = 0.5 meV. Any excitation arising from the ground state to this excited level would not have been observable on HET due to the width of the elastic peak. This was one of the cited reasons for the single crystal experiment on V2 (Section 4.3). If a peak was visible near 0.5 meV this would strengthen the proposed level scheme.

Although initially a broad peak was observed near this energy, subsequent experiments have not confirmed an excitation at this energy (Section 4.3.5).

Concrete proof that this level at 0.5 meV exists would be if the calculated magnetic susceptibility using the proposed level scheme and CEF parameters fitted to the experiment. If a good fit is obtained, a low lying level near 0.5 meV is likely. The calculation is also carried out for the Method 2 level scheme and CEF parameters, calculated from the susceptibility data and molecular field theory. Both methods are compared to the data to determine the best model of the 4*f* level scheme.

4.6.1 Method.

The orthorhombic TiNiSi-type structure has the point group D_{2h}. Another Pr system that has a similar structure is $PrCu_2$ [Ahmet *et al* (1996)]. All the RCu_2 compounds have the $CeCu_2$-type structure (with the exception of $LaCu_2$), with the space group D_{2h}^{28} . As mentioned in Section 4.1, the TiNiSi-type structure is very similar to the $CeCu_2$-type structure. Thus the 2 systems may be treated in similar ways for this work.

The crystalline electric field of $PrCu_2$ has been studied by Ahmet *et al* (1996). Using CEF theory, the energy level scheme of the $4f$ electrons has been estimated by fitting to the magnetic susceptibility data. Using the same approach, I can carry out a calculation to fit to the single crystal magnetic susceptibility data from UCL for PrNiSn. The nine-fold degenerate multiplet $^3H_4$ in PrNiSn should split into nine singlets under the influence of the orthorhombic crystalline electric field. This is reflected in the two levels schemes produced from the FOCUS program.

As previously mentioned, we can describe the full crystal field of PrNiSn by the Hamiltonian

$$H_{cef} = B_2^0 O_2^0 + B_2^2 O_2^2 + B_4^0 O_4^2 + B_4^2 O_4^2 + B_4^4 O_4^4 + B_6^0 O_6^0 + B_6^2 O_6^2 + B_6^4 O_6^4 + B_6^6 O_6^6$$

Equation 4.3

Where B_l^m are the crystal field parameters and O_l^m are the Stevens operator equivalents.

The magnetic susceptibility of the $4f$ ion is therefore written as

$$\chi_\alpha(T) = N(g_J \mu_B)^2 \left[\sum_{\lambda_i} \beta \frac{e^{-\beta E_{\lambda_i}}}{Z} \langle \lambda_i | J_\alpha | \lambda_i \rangle^2 + \sum_{\lambda_i} \sum_{\lambda_j} \frac{e^{-\beta E_{\lambda_i}} - e^{-\beta E_{\lambda_j}}}{Z} \frac{1}{\Delta E} \langle \lambda_j | J_\alpha | \lambda_i \rangle^2 \right]$$

Equation 4.4

Where g_J is the Lande g-factor, E_n the n^{th} eigenvalue and $|\lambda\rangle$ the n^{th} eigenfuntion, J_α is the angular momentum along α = x, y or z , $\Box E = E_n - E_m$, $Z = \sum_n e^{-\beta E_n}$, $\beta = \frac{1}{k_B T}$ and k_B is the Boltzmann constant.

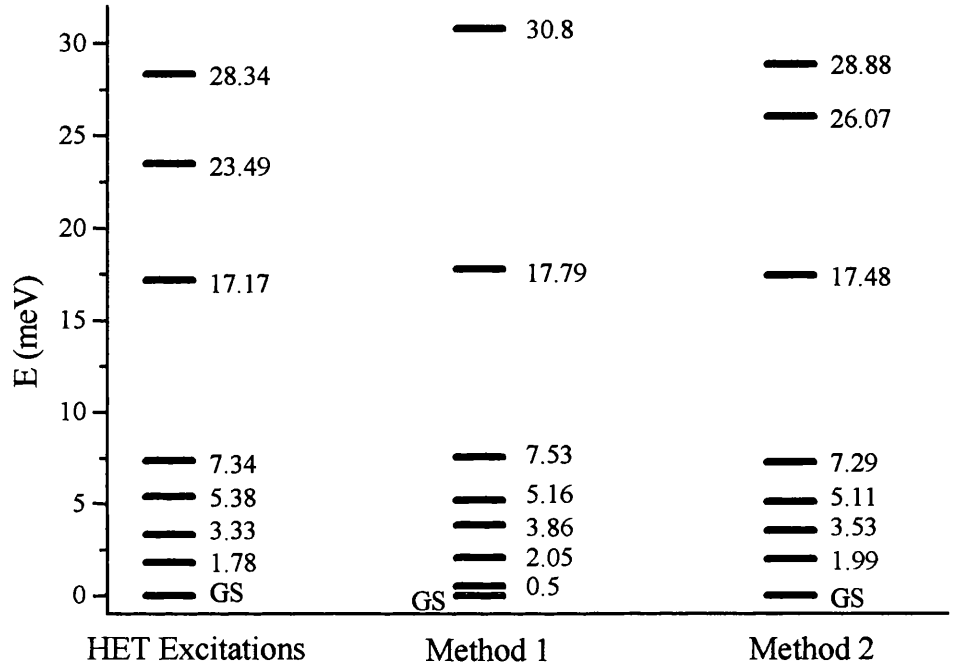

Figure 4.45: The proposed level schemes compared to the excitation data from HET. Note only 8 levels are shown for Method 2. The 9th level is at E = 47.9 meV, but is not shown so that the lower levels are clearer.

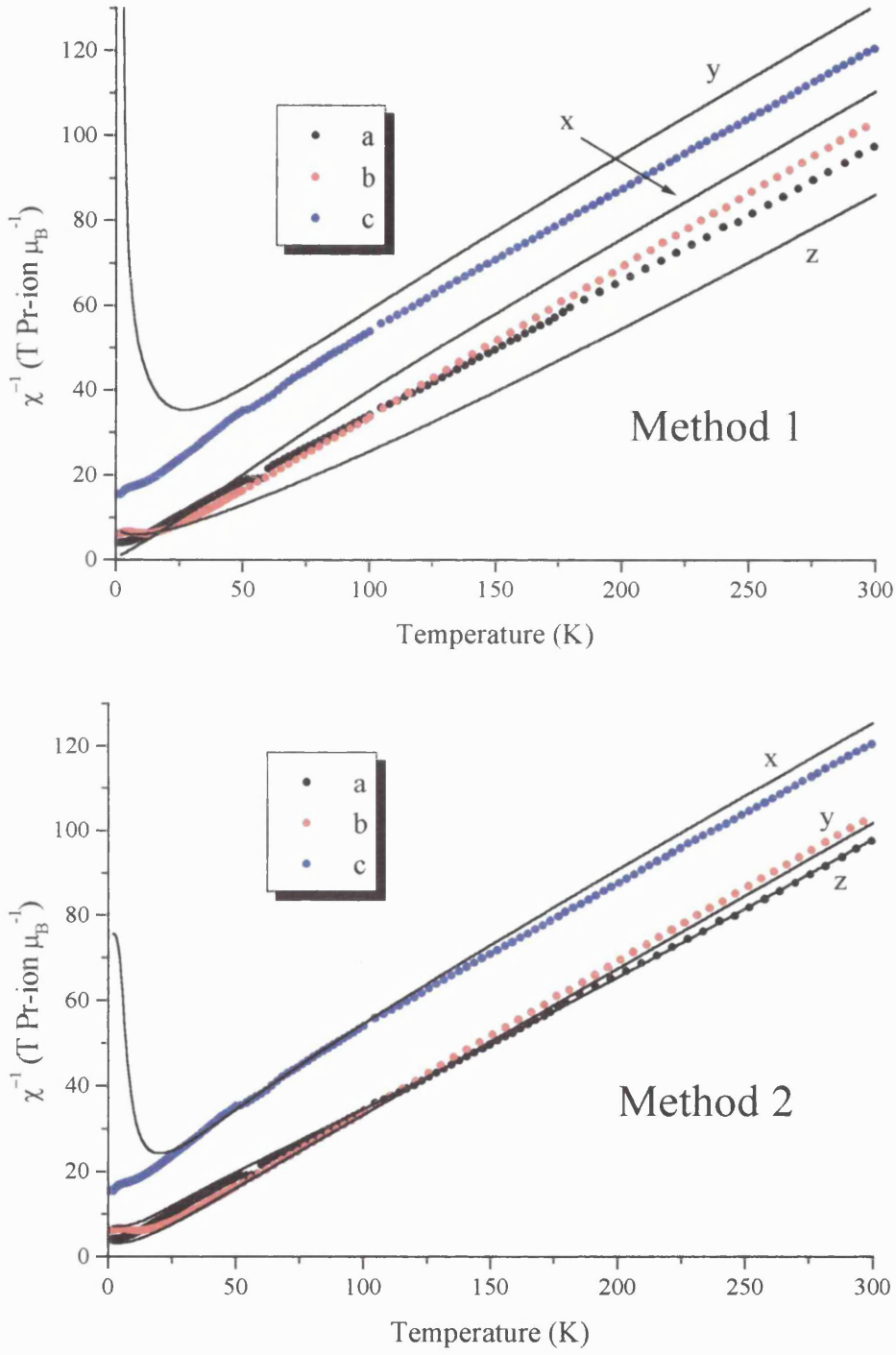

Figure 4.46: The experimental data for the single crystal PrNiSn and the CEF calculated inverse magnetic susceptibility for Method 1 and Method 2, between the temperatures 2 K – 300 K, at the applied field H = 300 G.

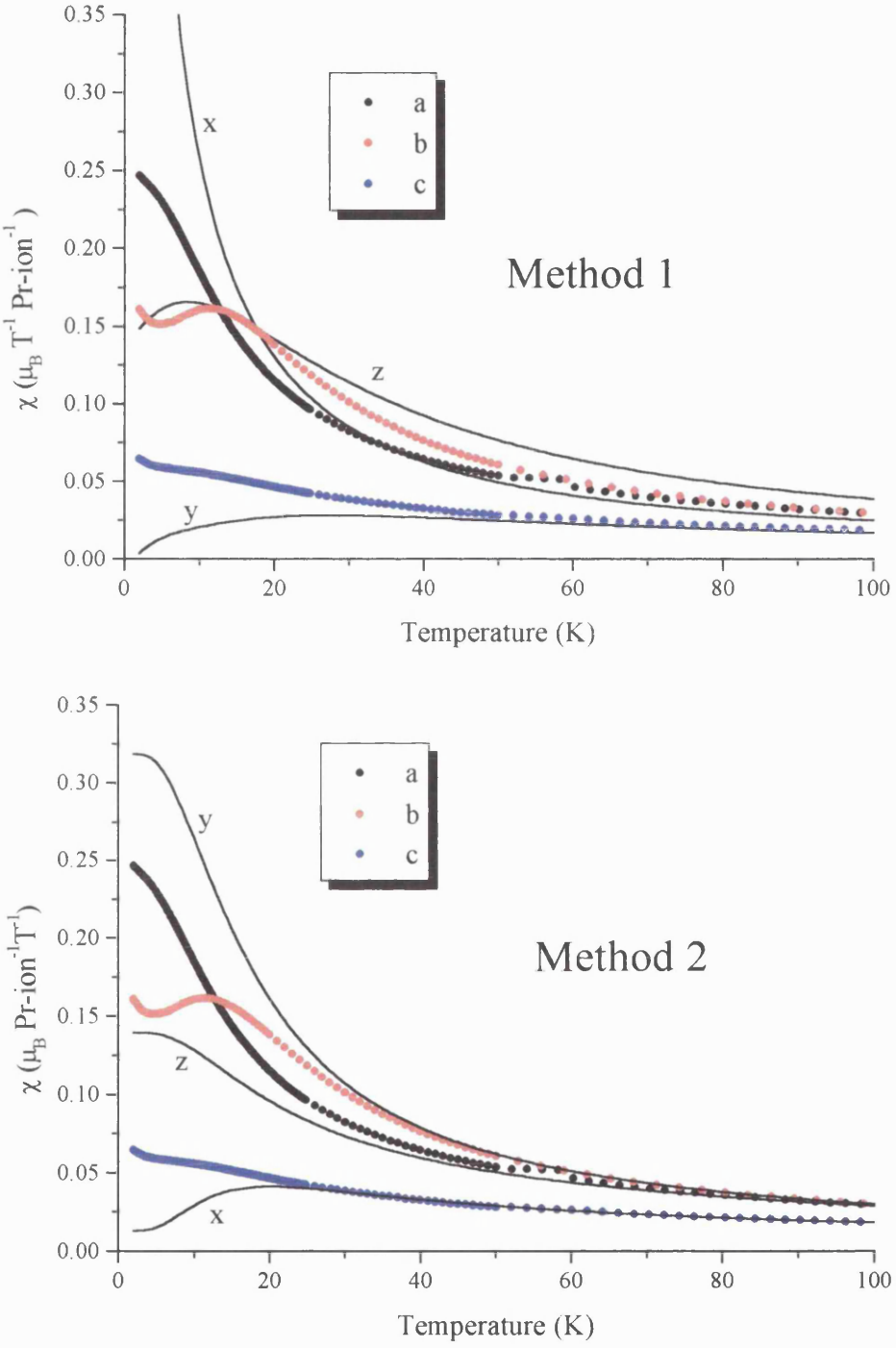

Figure 4.47: The experimental data for the single crystal PrNiSn and the CEF calculated magnetic susceptibility for Method 1 and Method 2, between the temperatures 2 K – 100 K, at the applied field H = 300 G.

From Figure 4.45, it is clear that the proposed Method 2 levels appear to fit to the observed excitations more closely than the Method 1 levels.

Using Equation 4.4 and the generated CEF parameters, a program was written in Fortran [J. Allen, *to be published*] to calculate the magnetic susceptibility, specific heat and resistivity along each axis.

Comparing the inverse magnetic susceptibility over the temperature range 2K – 300 K for each Method gives Figure 4.46.

It is immediately obvious that Method 2 fits to the inverse magnetic susceptibility better than Method 1, at high temperatures. This suggests that the level scheme generated from the Method 2 CEF parameters is closest to that of the $4f$ electron in the paramagnetic phase of PrNiSn.

Below 25 K, the calculated curves begin to deviate from the experimental curves [Figure 4.47]. This is not too surprising. At high temperatures, the low lying levels will be heavily populated. As we decrease the temperature, the levels depopulate, until at very low temperatures it is the ground state that is mostly populated. Thus, the majority of the excitations occur from the ground states to the excited states, and if the level scheme is not quite correct, it will be reflected in the fit, as is demonstrated in Figure 4.47.

CHAPTER 5

NdNiSn

5.1 Neutron Powder diffraction.

Previous work [Rossi *et al* (1985)] on NdNiSn shows the crystal structure to be the orthorhombic TiNiSi-type, the same as PrNiSn. The space group (*Pnma*) and atom position is detailed in section 4.1, and Figure 4.1 depicts the atoms in the RNiSn unit cell. As mentioned in this section, the rare earth atoms are on the 4(c) site: $x,1/4,z;\ \bar{x},3/4,\bar{z};\ 1/2-x,3/4,1/2+z;\ 1/2+x,1/4,1/2-z.$, where x = 0.00 and z = 0.700.

The aim of this experiment was therefore to confirm previous X-ray data [Rossi *et al* (1985)] at room temperature, and to determine the magnetic structure below the transition temperature, reported by B. Chevalier *et al* (1996) to be T_N = 3.1 K.

5.1.1 Experimental procedure

The sample was prepared by arc melting the constituent elements under an argon atmosphere. The purity was 99.999% for Ni and Sn and 99.9% for Nd. The mixture was melted several times to achieve homogeneity, with a small percentage (<1%) of extra Sn to account for any mass loss. The buttons were then annealed at 500°C and P $\approx 5\times10^{-6}$ Torr for 7 days. The mass of sample used in the experiment was approximately 10g, filled in a vanadium can and mounted in an orange cryostat. The D20 high intensity two-axis powder diffractometer provided neutrons with a wavelength of $\lambda = 2.4$ Å and with a Roots pump attached we were able to achieve temperatures of 1.7 K. The counting time for each data file is 90 minutes, with $10 \leq 2\theta \leq 160$. The data was analysed by the Rietveld method using the Fullprof98 program, which is based on a least squares refinement.

5.1.2 Results

Neutron powder diffraction data was taken at 30 K and at a range of temperatures from 8 K to 2 K. At each temperature the data is indexed by assuming the system was of the TiNiSi-type. The initial parameters are taken from Rossi *et al*'s paper that gave the above structure. The calculated parameters for 2 K and 30 K are given in Table 5.1 and the corresponding plots showing the raw data, Rietveld fit and difference are shown in Figures 5.1 and 5.2. The peaks are fitted to a pseudo-Voigt shape, which is a weighted mixture of Gaussian and Cauchy profiles. Table 5.1 gives the lattice parameters and atomic positions determined from the Rietveld fit.

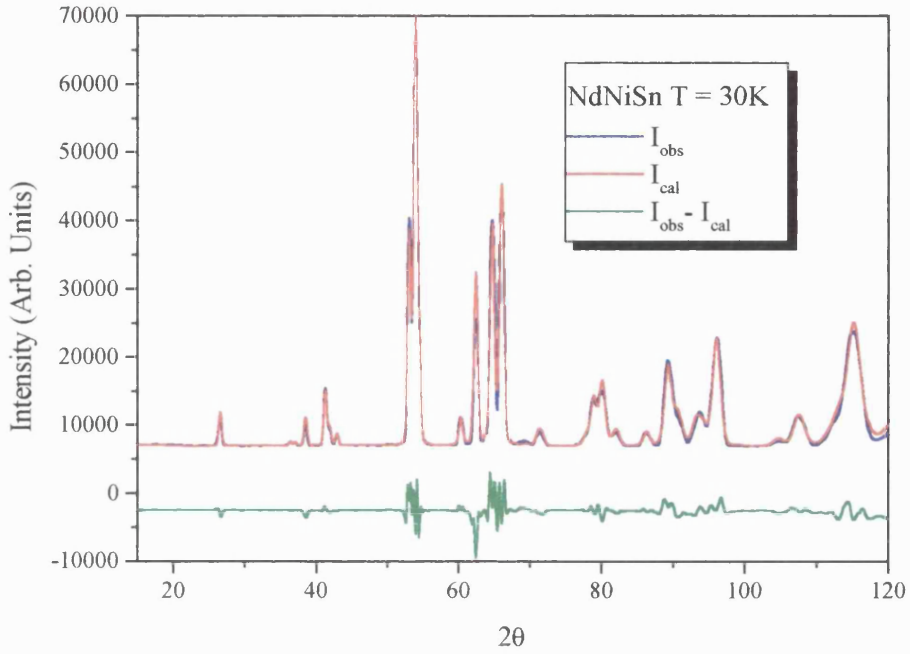

Figure 5.1: T = 30 K powder diffraction pattern with Rietveld refinement obtained using Fullprof98.

	30K	2K
A (Å)	7.32457 ± 0.00091	7.32431 ± 0.00107
B (Å)	4.50071 ± 0.00050	4.50044 ± 0.00059
C (Å)	7.61335 ± 0.00088	7.61514 ± 0.00105
V ($Å^3$)	250.980 ± 0.051	251.015 ± 0.060
Nd		
x	-0.01622(99)	-0.01600(116)
Z	0.69937(50)	0.69936(57)
Ni		
x	0.19512(56)	0.19552(62)
Z	0.08653(77)	0.08671(90)
Sn		
X	0.31637(92)	0.31738(101)
Z	0.41448(139)	0.41468(162)
R_{Bragg}(%)	7.42	8.54

Table 5.1: Lattice parameters and atomic positions for NdNiSn obtained from the Rietveld fitting to the Pnma space group (TiNiSi-type structure) at T = 30K and 2K.

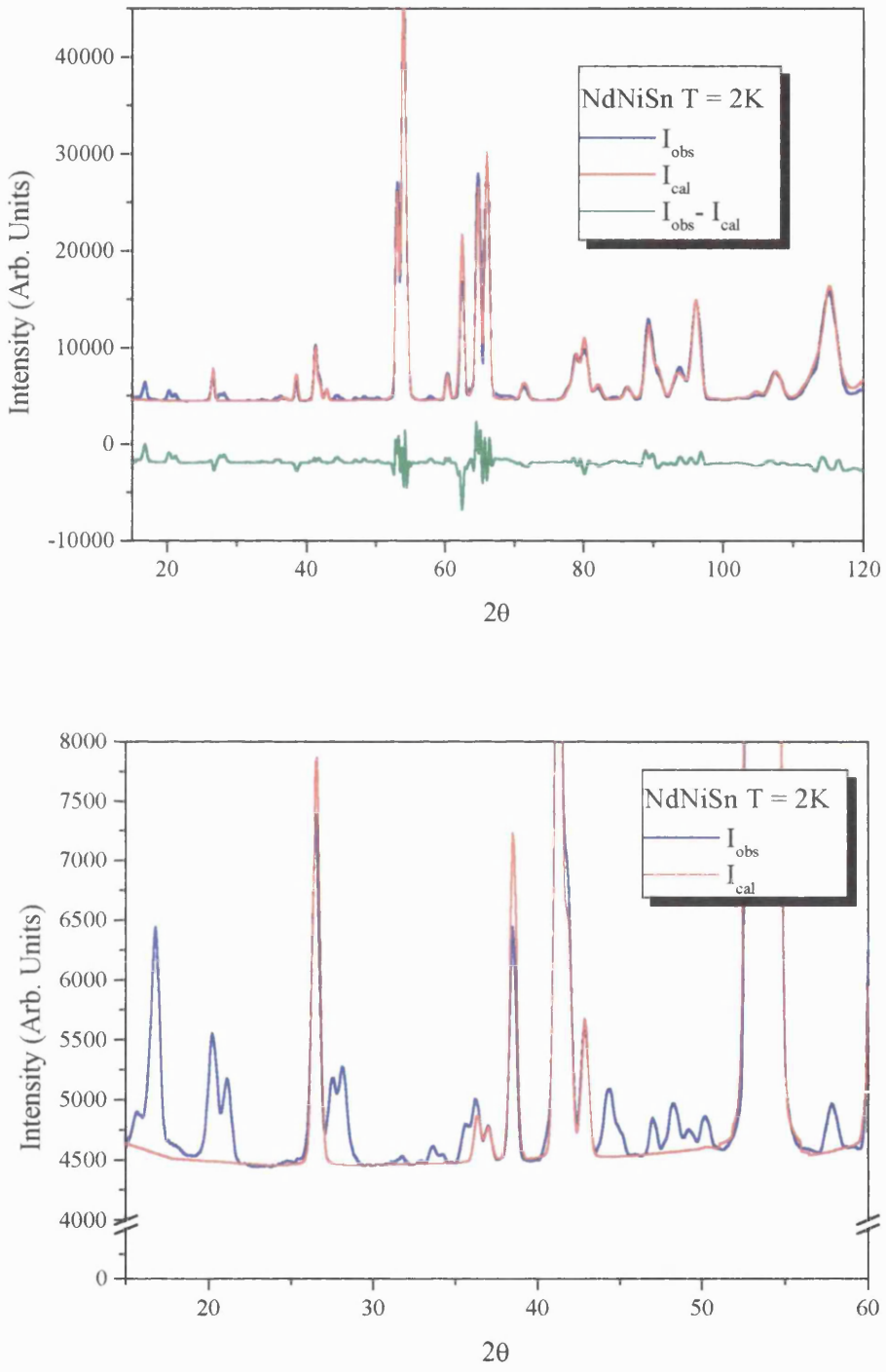

Figure 5.2: T = 2 K powder diffraction pattern with Rietveld refinement obtained using Fullprof 98. The first picture shows the fit and the difference plot. The second figure depicts the low angle data, showing the antiferromagnetic peaks that have not been fitted.

It is clear from the extra peaks seen in Figure 5.2 that at T = 2 K the compound is antiferromagnetic. This is also reflected in the parameters shown in Table 5.1. Because the fit to the data has only taken account of the crystal structure, the R_{Bragg} factor is higher for the fit at this temperature.

Figure 5.3 depicts the difference in the diffraction patterns at T = 8 K and T = 2 K. What is immediately evident is that the magnetic peaks are doubled up. This indicates that the antiferromagnetic structure is not a simple one. This was borne out in the attempted fit to the magnetic structure. Starting from antiferromagnetic structures seen in other RNiSn compounds, such as the squared incommensurate structure of DyNiSn [S. Kawano *et al* (1998)] $\mathbf{q}$ = (0.641, 0.340, 0), and a sine-modulated magnetic structure for TbNiSn [J.K Yakinthos *et al* (1995)] $\mathbf{q}$ = (0.311, 0.325, 0), it was impossible to fit to the available data. This was also the case for simple anitferromagnetic structures.

It is very clear that a diffraction experiment needs to be carried out at a higher resolution on this compound, or a diffraction experiment using the single crystal.

It was possible however, to observe the intensity of the magnetic peaks with temperature. Taking the peak at $2\theta = 58°$, and fitting to a single Gaussian for each temperature scan between 2 K and 8 K, the area under the graph (Intensity) may be plotted as a function of temperature [Figure 5.4]. It is clear that as the system approaches T_N = 3.1 K from T = 2 K, the intensity of the magnetic peak decreases.

This peak was chosen because it is in a region of the scan where no other peaks are visible. Thus, the tails from any other peaks nearby do not affect the Gaussian fit to the peak.

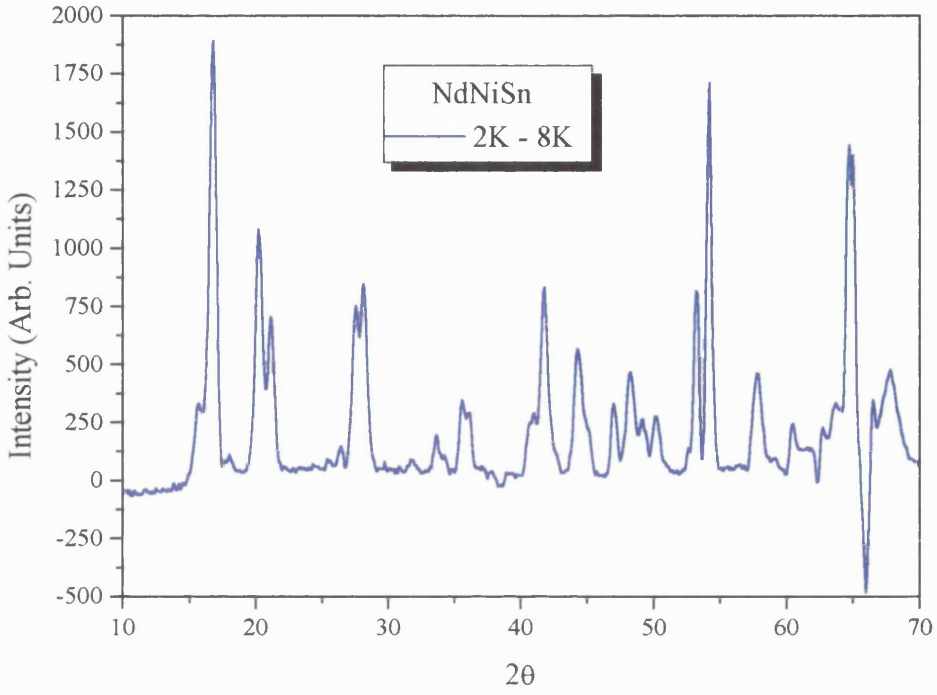

Figure 5.3: Difference plot between the antiferromagnetic regime (T = 2 K) and the paramagnetic phase (T = 8 K). Note that the peaks all consist of 2 or more individual peaks.

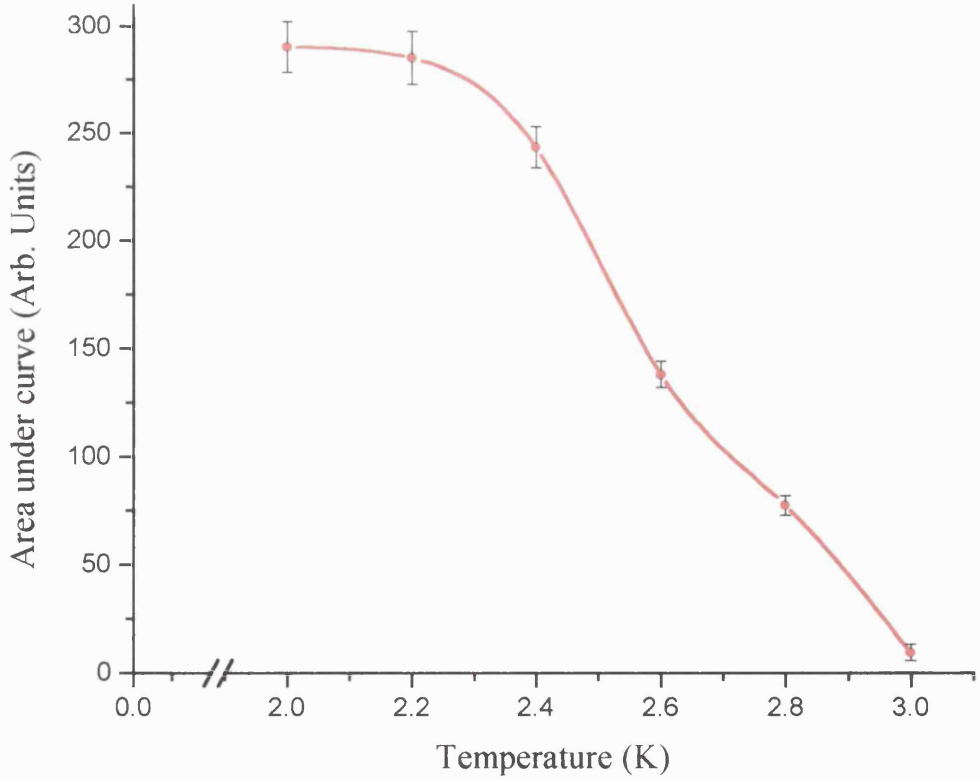

Figure 5.4: A plot of T v A for the antiferromagnetic peak at 2 θ = 58°.

5.2 Polycrystalline powder inelastic neutron scattering (HET, ISIS)

5.2.1 Experimental procedure.

Inelastic neutron scattering has been carried out on a 20g NdNiSn powder sample on the HET chopper spectrometer at ISIS, Didcot. The set up for the experiment was identical to that used in the inelastic neutron scattering experiment on powder PrNiSn [Chapter 4.2].

5.2.2 CEF excitation results.

Inelastic measurements were taken at 5 different incident energies: E_i = 23, 35, and 60 meV. The specifications for each run are shown in Table 2 below.

E_i (meV)	μAhr	Chopper Frequency (Hz)	T_{head} (K)	T_{sample} (K)
23	367	150	1.9	1.66
23	500	150	4.42	4.43
23	500	150	24.6	25.0
35	500	200	4.42	4.44
60	500	200	4.50	4.50

Table 5.2: Specifications of the data runs for NdNiSn on HET, showing the incident energy E_i, μAhrs, chopper frequency, and the average temperature of the CCR head and sample.

Like PrNiSn, NdNiSn has the TiNiSi-type structure and the crystal field experienced by the Nd-ion is approximately the same (taking account of the lattice parameter differences) as that experienced by the Pr-ion. Unlike Pr however, Nd

has J = 9/2. Because the ground state multiplet splitting depends upon J and the point symmetry of the crystal field, we do not expect 9 singlet states as in PrNiSn. The point group D_{2h}, when designated to a system with J = 9/2 such as NdNiSn, gives rise to 5 doublets (J+1/2 doublets) [O. Moze, (1998)].

This is clearly demonstrated in the system $NdCu_2$, which has the orthorhombic $CeCu_2$-type structure. As covered in Chapter 3, this structure is very similar to the TiNiSi-type. Inelastic neutron scattering [Gratz, E *et al* (1991)] shows 4 CEF excitations from the ground state doublet to the 4 excited doublet levels, showing an overall splitting of 14 meV.

Analysis of the results was carried out in the same way as PrNiSn. The low angle:high angle ratio of 1:4 was used to estimate the phonon background.

From the 23, 35 and 60 meV spectra [Figures 5.6 – 5.10], we can clearly see 4 CEF excitations, at E ≈ 5.4, 11.7, 16.3 and 24 meV, no doubt from the ground state doublet to the excited doublet levels. Thus the overall splitting is approximately 24 meV. If we assume each excitation is from the ground state to the excited doublets, we can propose a simple level scheme [Figure 5.5]

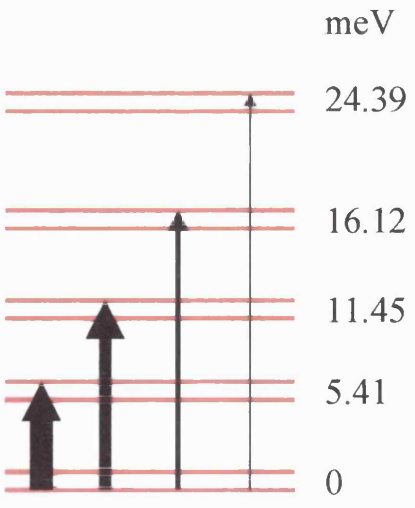

Figure 5.5: Proposed CEF level from the fits [Figures 4, 5, 7 - 11] to the T = 4.5 K and E_i = 23, 35 and 60 meV.

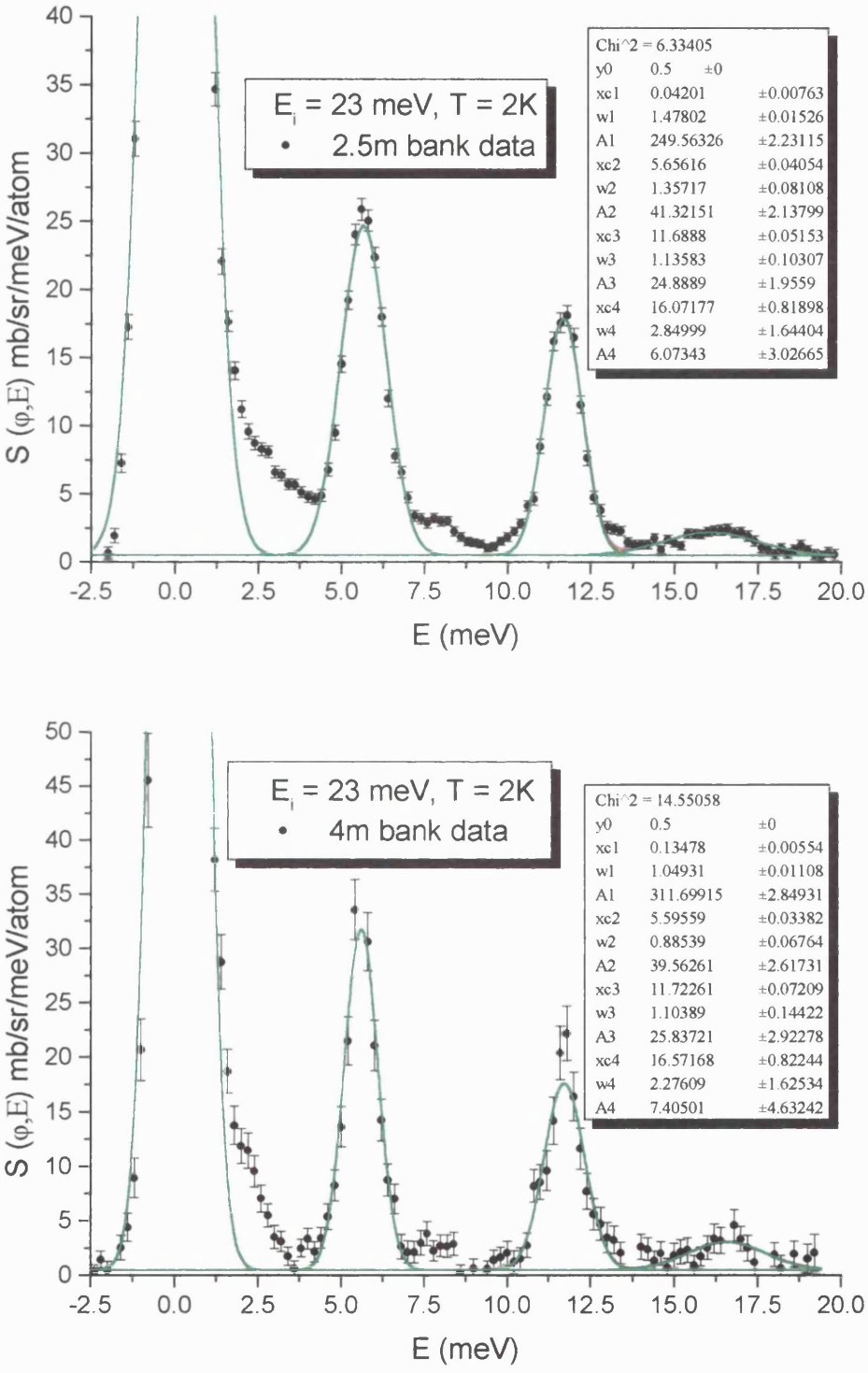

Figure 5.6: Gaussian fit to the proposed 3 lowest CEF peaks seen in the 2.5m and 4m banks E_i = 23 meV T = 2 K spectra, minus the phonon contribution. Parameters for each peak are shown in the inserts.

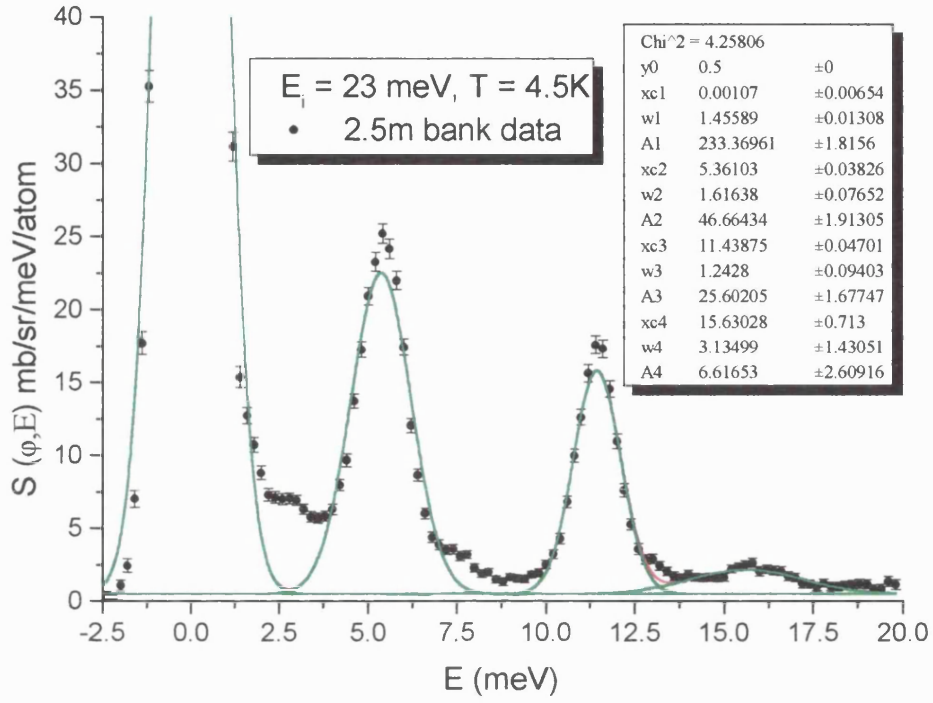

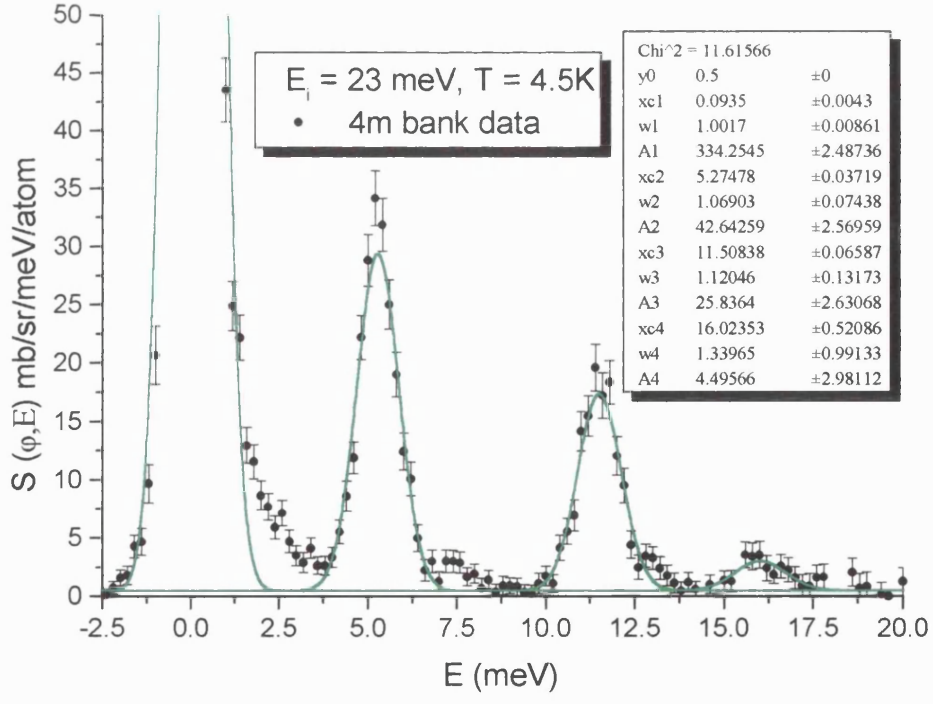

Figure 5.7: Gaussian fit to the proposed 3 lowest CEF peaks seen in the 2.5m and 4m banks E_i = 23 meV T = 4.5 K spectra, minus the phonon contribution. Parameters for each peak are shown in the inserts.

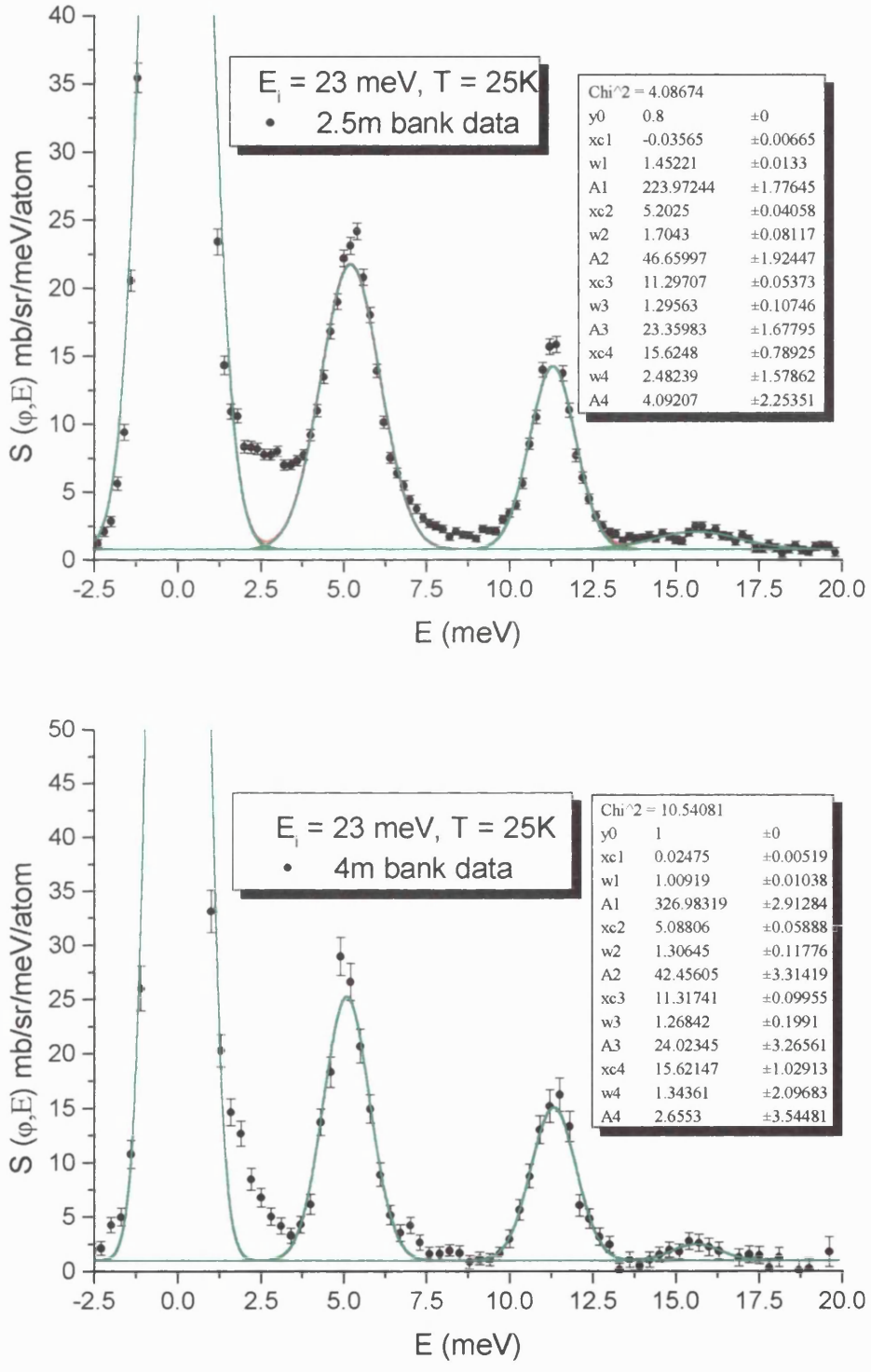

Figure 5.8: Gaussian fit to the proposed 3 lowest CEF peaks seen in the 2.5m and 4m banks E_i = 23 meV T = 25 K spectra, minus the phonon contribution. Parameters for each peak are shown in the inserts.

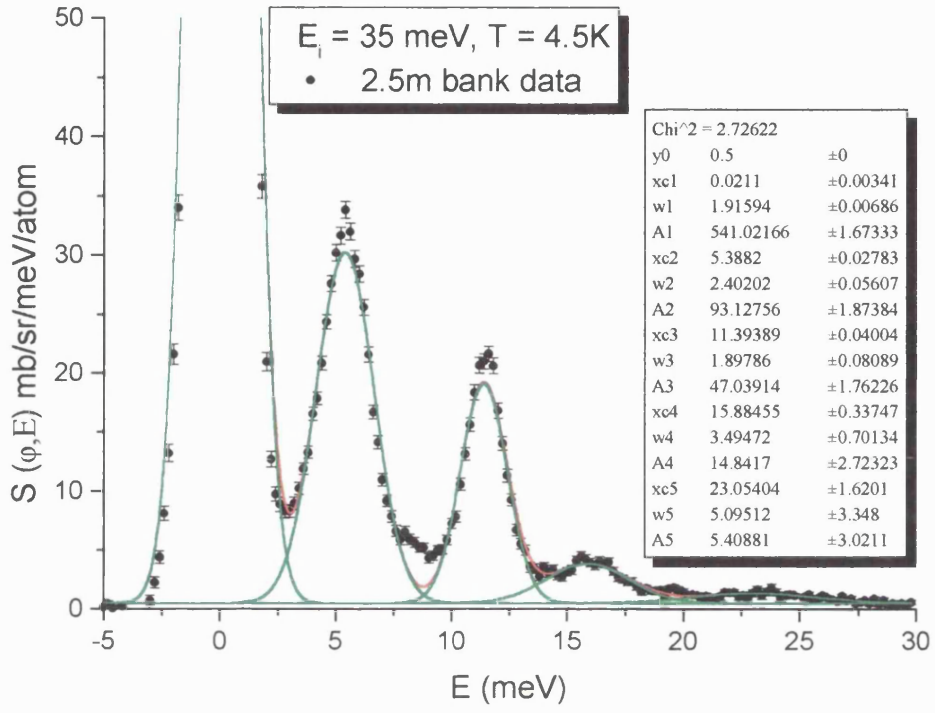

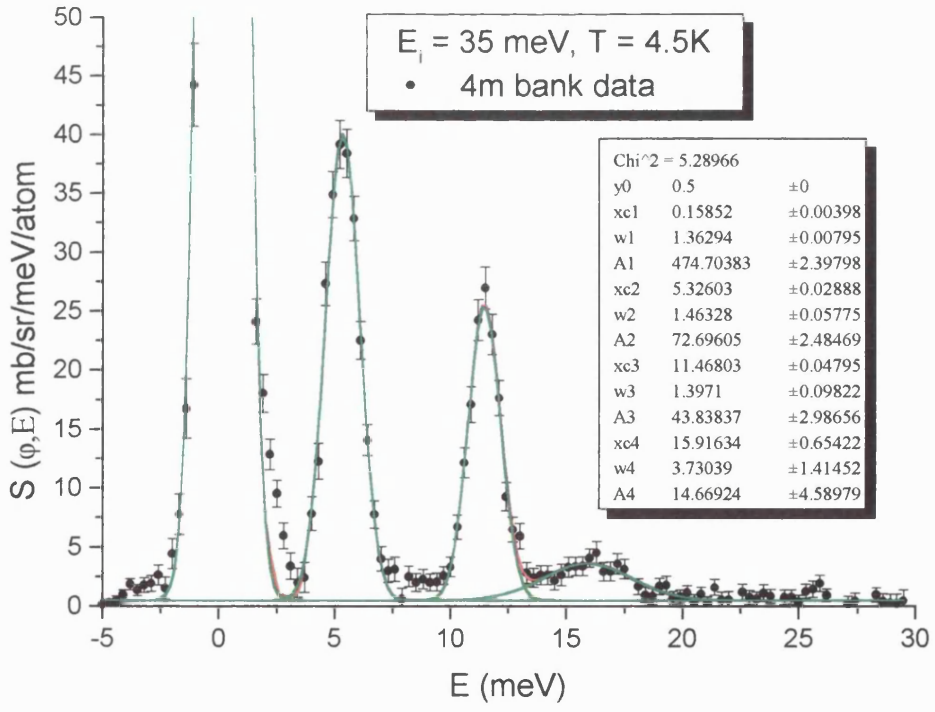

Figure 5.9: Gaussian fit to the proposed 3 lowest CEF peaks seen in the 2.5m and 4m banks E_i = 35 meV T = 4.5 K spectra, minus the phonon contribution. Parameters for each peak are shown in the inserts.

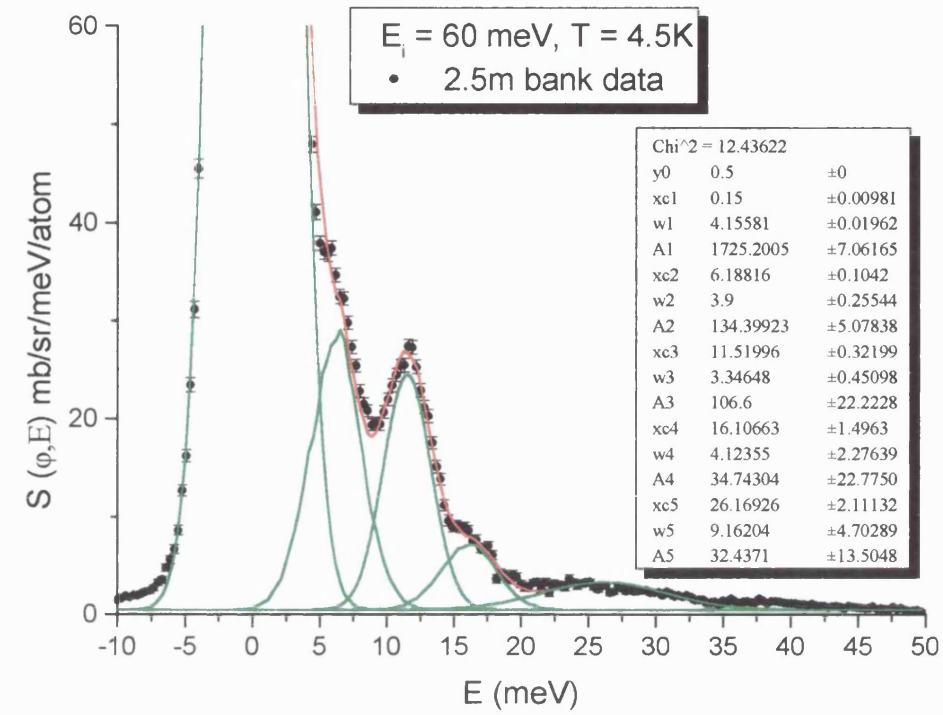

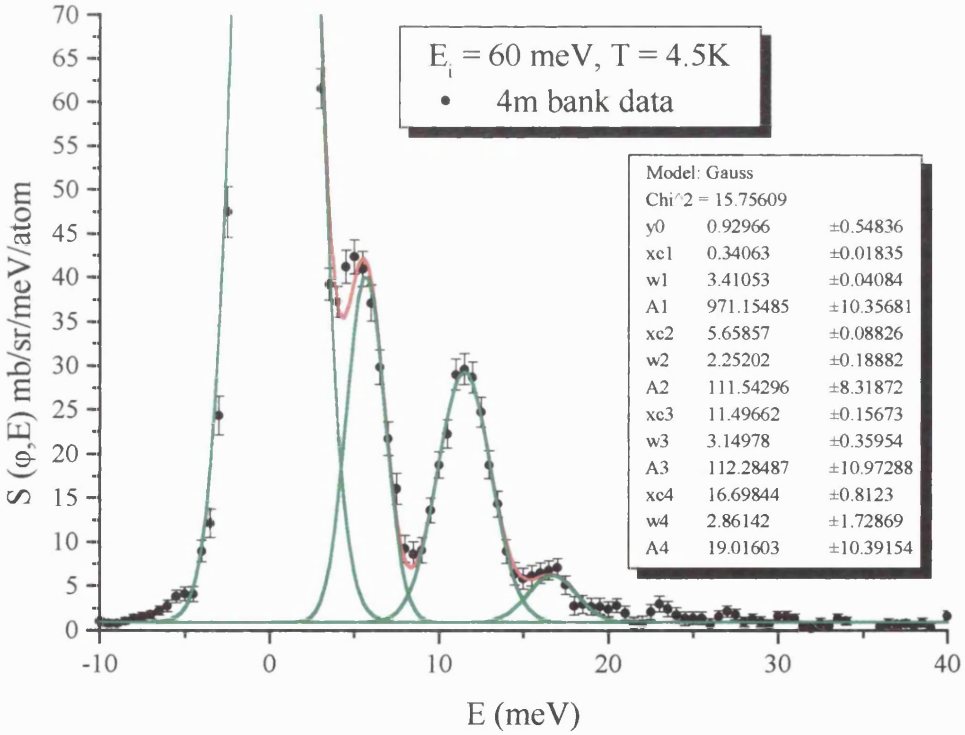

Figure 5.10: Gaussian fit to the proposed 4 CEF peaks seen in the 2.5m bank E_i = 60 meV T = 4.5 K spectra, minus the phonon contribution, and to the 3 lowest CEF peaks in the 4m bank E_i = 60 meV T = 4.5 K. Parameters for each peak are shown in the inserts.

Simple analysis of the available data has yielded a possible level scheme of 5 doublets, based on point group theory and the data scans.

If we firstly concentrate on the behaviour of the two main CEF peaks seen in the $E_i = 23$ meV data [Figures 5.6 – 5.8] we can see a change in energy from the 2 K, 4.5 K and 25 K data. Between 2 K and 4.5 K (the antiferromagnetic state and the paramagnetic state) there is an average energy shift of 0.33 meV, and between 2 K and 25 K, an average shift of 0.52 meV. Accurate values of the shifts in energy are shown in Table 5.3.

Table 5.4 shows the peak positions, widths and intensities for each excitation at T = 4.5 K. The average energy positions of the excitations at this temperature have been calculated and they are also shown in Table 5.4. These are E = 5.38, 11.44, 15.95 and 24.2 meV.

E_i = 23 meV											
2K			4.5K			25K					
2.5m	4m	$\bar{E}_{2K}$	2.5m	4m	$\bar{E}_{4.5K}$	2.5m	4m	$\bar{E}_{25K}$	$\bar{E}_{2K}$- $\bar{E}_{25K}$	$\bar{E}_{4.5K}$- $\bar{E}_{25K}$	$\bar{E}_{2K}$- $\bar{E}_{4.5K}$
5.66±0.04	5.60±0.03	5.62±0.02	5.36±0.04	5.27±0.04	5.31±0.03	5.20±0.04	5.09±0.06	5.17±0.03	0.45±0.05	0.14±0.06	0.31±0.05
11.69±0.05	11.72±0.07	11.70±0.04	11.44±0.05	11.51±0.07	11.46±0.04	11.30±0.05	11.32±0.10	11.30±0.04	0.40±0.08	0.16±0.08	0.24±0.08
16.07±0.82	16.57±0.82	16.32±0.58	15.63±0.71	16.02±0.52	15.88±0.42	15.62±0.79	15.62±1.03	15.62±0.63	0.70±1.21	0.26±1.05	0.44±1.00

Table 5.3: The Gaussian fits to the three excitations observed in the E_i = 23 meV spectra, at T = 2 K, 4.5 K and 25 K. Also shown is the average difference between each temperature of the peak centres for each of the excitations.

E_i=23meV						E_i=35meV					
2.5m bank			4m bank			2.5m bank			4m bank		
E(meV)	W(meV)	A	E(meV)	W(meV)	A	E(meV)	W(meV)	A	E(meV)	W(meV)	A
5.36 ±0.04	1.62 ±0.08	46.66 ±1.91	5.27 ±0.04	1.07 ±0.07	42.64 ±2.57	5.39 ±0.03	2.40 ±0.06	93.13 ±1.87	5.33 ±0.03	1.46 ±0.06	72.70 ±2.48
11.44 ±0.05	1.24 ±0.09	25.60 ±1.68	11.51 ±0.07	1.12 ±0.13	25.84 ±2.63	11.39 ±0.04	1.90 ±0.08	47.04 ±1.76	11.47 ±0.05	1.40 ±0.10	43.84 ±2.99
15.63 ±0.71	3.13 ±1.43	6.62 ±2.61	16.0 ±0.52	1.34 ±0.99	4.50 ±2.98	15.88 ±0.34	3.49 ±0.70	14.84 ±2.72	15.92 ±0.65	3.73 ±1.41	14.67 ±4.59
						23.05 ±1.62	5.10 ±3.35	5.41 ±3.02			

E_i=60meV						E(meV)
	2.5m bank			4m bank		
E(meV)	W(meV)	A	E(meV)	W(meV)	A	
6.19 ±0.10	3.9±±0.26	134.40 ±5.08	5.66 ±0.09	2.25 ±0.19	111.54 ±8.32	5.38 ±0.02
11.52 ±0.32	3.35 ±0.45	106.60 ±22.22	11.5 ±0.16	3.15 ±0.36	112.28 ±10.97	11.44 ±0.02
16.11 ±1.50	4.12 ±2.28	34.74 ±22.78	16.70 ±0.81	2.86 ±1.73	19.02 ±10.39	15.95 ±0.23
26.17 ±2.11	9.16 ±4.70	32.44 ±13.50	-	-	-	24.21 ±1.28

Table 5.4: The peak positions, widths and intensities for each excitation for each of the scans at T = 4.5 K, and the average energy position of the CEF excitations at this temperature.

5.3 Susceptibility and Magnetisation.

The magnetic susceptibility and magnetisation of polycrystalline and single crystal NdNiSn has been carried out on the Quantum design SQUID at UCL. The experimental set-up is the same as specified for the PrNiSn SQUID experiment [Chapter 4.4].

5.3.1 Polycrystalline results.

Rousti *et al* (1992a) have previously determined the magnetic susceptibility down to T = 4.2 K, with no evidence of a magnetic transition. Their results show a Curie Weiss temperature of θ_{CW} = -4 K and an effective moment of μ_{eff} = 4.2μ_B/Nd, which is substantially larger than the free ion moment of Nd^{3+} (3.68μ_B/Nd). Chevalier *et al* (1996), in their study of Nd_2Ni_2Sn, have shown an antiferromagnetic (AF) transition at T = 3.0 K for NdNiSn, and this is confirmed at T = 3.0 K in our results [Figure 5.11].

Chevalier *et al*'s results show a Curie Weiss temperature of θ_{CW} = -12 K and an effective moment of μ_{eff} = 3.74μ_B/Nd, which is closer to the free ion value then that reported by Routsi *et al.* NdNiSn does indeed follow the Curie Weiss law, the polycrystalline data giving θ_{CW} = -17.7 K and μ_{eff} = 3.66μ_B down to 50 K. It is clear the polycrystalline results are closer to the results from Chevalier *et al* than Routsi *et al.* Like PrNiSn, the calculated effective moment is very close to the free-ion moment, indicating the nickel and tin contribute little or nothing to the overall magnetisation and the majority of the magnetic moment is situated on the Nd ions.

Figure 2 depicts the field dependence of the magnetisation at 4 different temperatures: in the antiferromagnetic state at T = 2.0 K, T_N = 3.0 K, just above the transition temperature at T = 5.0 K, and T = 10 K in the paramagnetic regime. At T = 10 K the data is linear up to 4.5 T, but in the AF state (T = 2 K) the magnetisation appears to have almost saturated at H = 7 T, and also demonstrates a tendency towards a metamagnetic transition between 1 T and 3 T [Figure 5.12, Inset]. The data at T = T_N = 3.0 K also curves towards saturation, but slightly lower then that at T = 2 K. It is interesting to note the crossover of these 2 curves at H = 2.25 T, as well as a low-field linearity, an indication of antiferromagnetic behaviour.

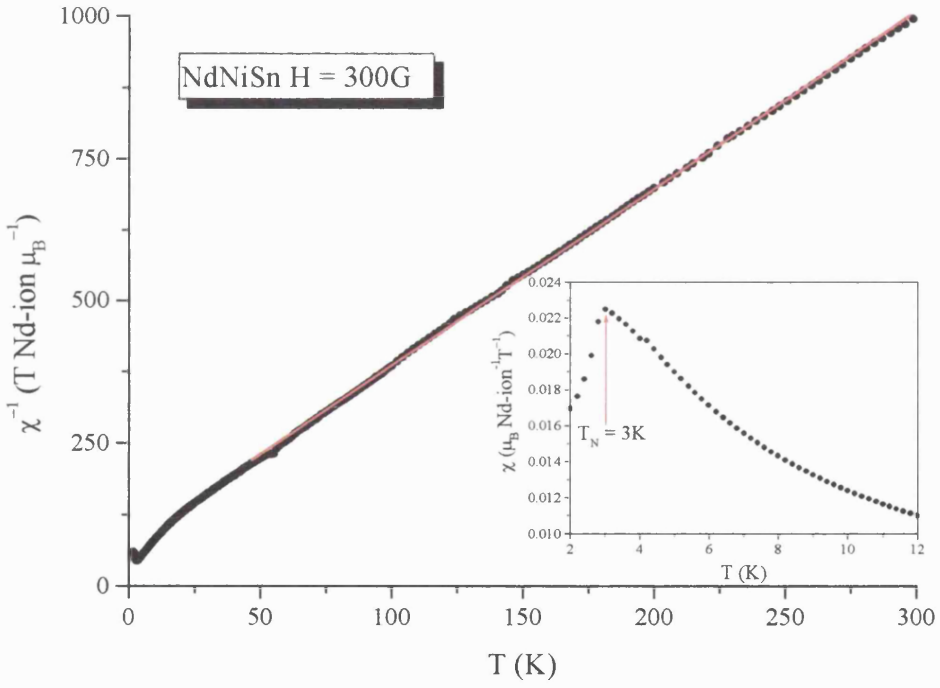

Figure 5.11: Temperature dependence of the inverse susceptibility of polycrystalline NdNiSn in an applied field of 300 G, with the red line a Curie Weiss fit down to 50 K. The inset shows the low temperature susceptibility at the same applied field. The AF transition is clearly visible at T_N = 3.0 K.

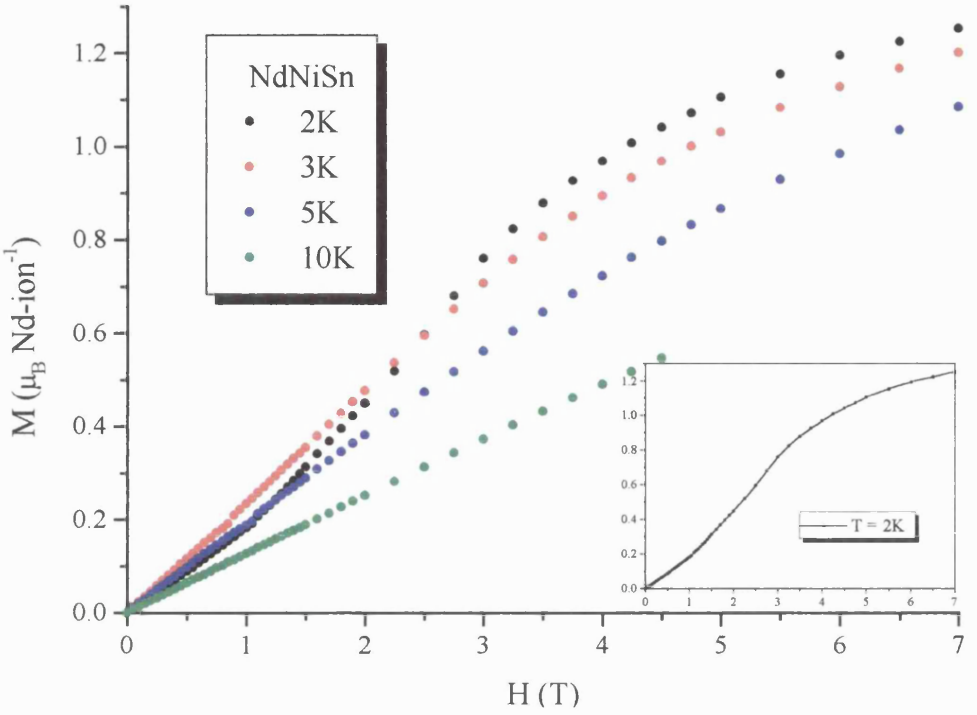

Figure 5.12: Field dependence of the magnetisation of polycrystalline NdNiSn at 4 different temperatures. The inset shows the M v H data at T = 2 K (in the AF state) more clearly.

5.3.2 Single Crystal results.

5.3.2.1 Magnetic susceptibility.

Single crystal measurements have been carried out along all principal axes. The antiferromagnetic transition at T_N = 3.0 K is observed in each axis [Figure 5.13, Inset], with **b** the easy axis and **c** the hard axis. NdNiSn shows strong anisotropy at T = 2 K, with $\chi_b \approx 4.5\chi_c$ and $\approx 1.8\chi_a$. At T_N = 3.0 K the anisotropy is even larger, with $\chi_b \approx 8\chi_c$ and $\approx 2.9\chi_a$. The strong anisotropy is present up to room temperature.

As in the polycrystal, each axis demonstrates Curie Weiss-like behaviour down to 50 K. The Curie Weiss temperatures and effective moments are tabulated in Table 5.5. Unlike PrNiSn [Chapter 4.4], each axis has a negative Curie Weiss temperature, but the difference in magnitude is still evident between axes.

Like in PrNiSn, the hard axis (**c**) shows the largest negative value (θ_{CW} = -44.4 K), while the **a** and **b** axes show relatively small values (θ_{CW} = -6.8 K and –1.0 K respectively), again a result of the large splitting due to crystal field effects. If one assumes that $\chi_p = 1/3\ (\chi_a+\chi_b+\chi_c)$, the single crystal data fits the polycrystalline Curie-Weiss temperature perfectly. The effective moments of each axis are all close to the free-ion moment of Nd, indicating the Ni carries no magnetic moment in the paramagnetic state, as we expected from the polycrystalline results.

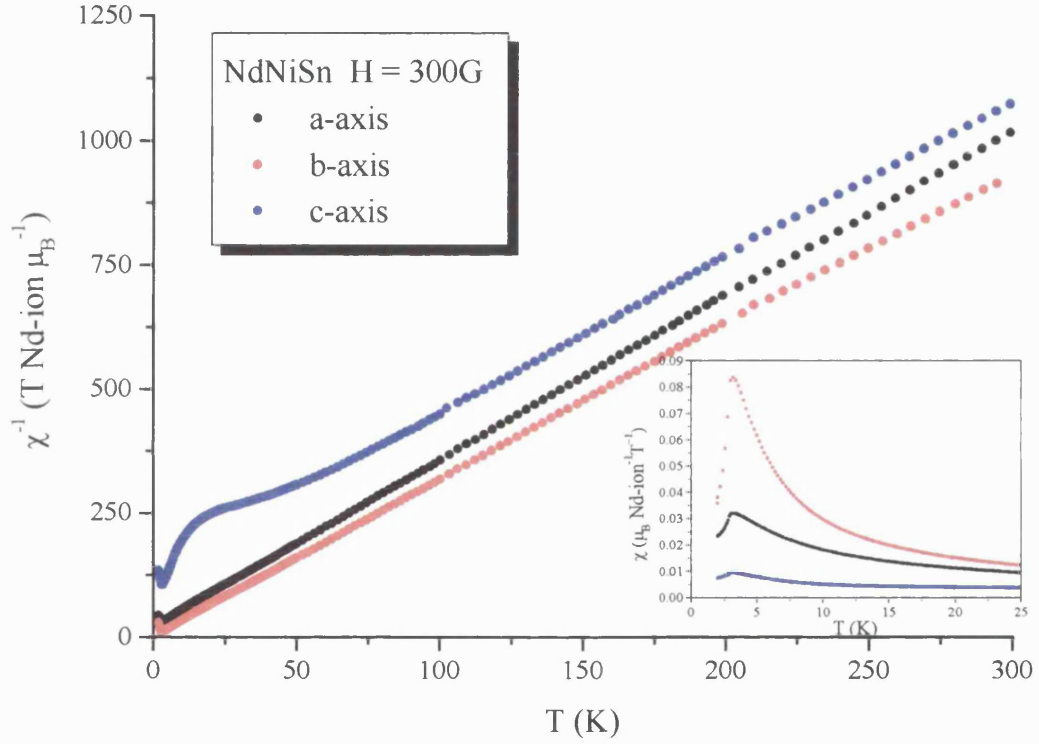

Figure 5.13: Temperature dependence of the inverse susceptibility of NdNiSn single crystal, measured along the main axes in a field of 300 G. The inset shows the low temperature susceptibility for each axis at the same applied field. The AF transition is clearly visible at T_N = 3.0 K in all axes.

	A	B	c	polycrystalline
θ_{CW} (K)	-6.8	-1.0	-44.4	-17.7
μ_{eff} (μ_B/Nd-ion)	3.54	3.65	3.65	3.66

Table 5.5: Summary of the values for the Curie Weiss temperatures and effective moments calculated from the magnetic susceptibility data.

5.3.2.1.1 Low temperature magnetic susceptibility with various fields.

Figure 5.14 depicts the low temperature (2 K – 10 K) magnetic susceptibility along the **a** axis for three different applied fields, H = 0.03 T, 0.3 T and 1 T. The transition temperature T_N does not change with field (up to 1 T), and the maximum susceptibility at T_N scales linearly with field.

Figure 5.15 shows the same effect for 2 applied fields along the **b** axis. The transition temperature does not shift with applied field and the magnitude of the susceptibility scales linearly with field according to the data shown.

The magnitudes of the susceptibility for T_N at these fields for both axes are depicted in Table 5.6, as well as the susceptibility at T_N and H = 0.03 T for the **c** axis.

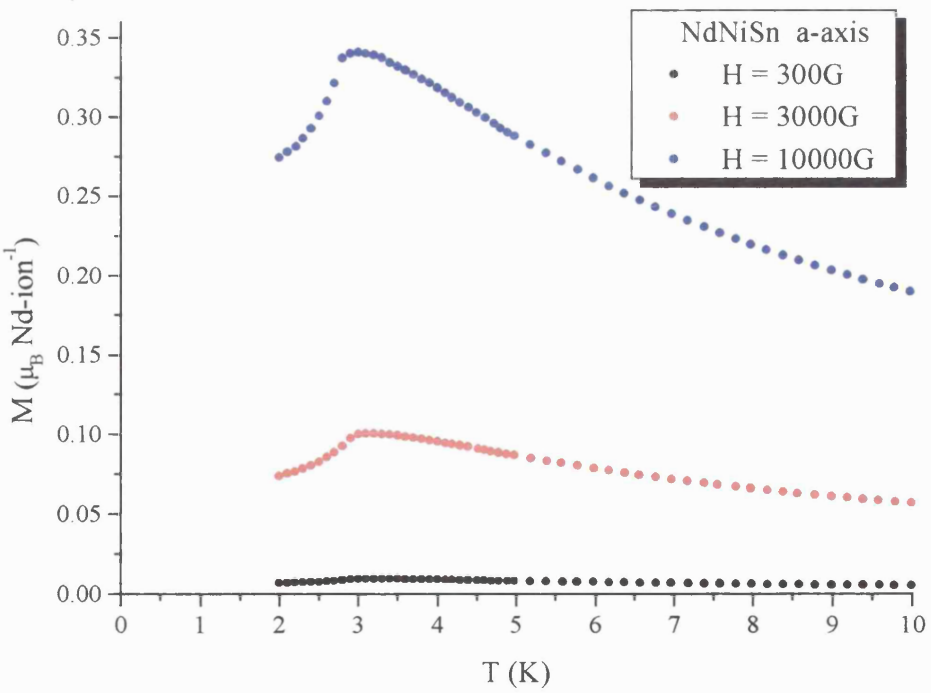

Figure 5.14: The transition at T_N = 3 K at different applied fields along the **a** axis.

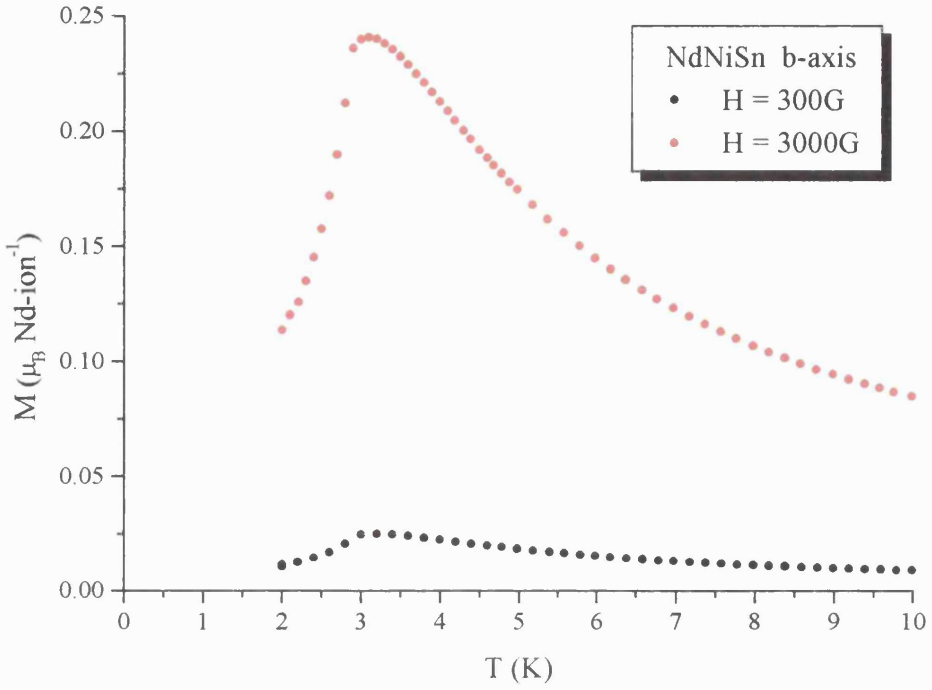

Figure 5.15: The transition at T_N = 3 K at different applied fields along the **b** axis.

H (T)	M (μ_B/Nd-ion)	M (μ_B/Nd-ion)	M (μ_B/Nd-ion)
0.03	0.010	0.025	0.0029
0.3	0.10	0.24	-
1	0.34	-	-

Table 5.6: The Magnetisation at T_N for different fields along the three principal axes, taken from the data shown in Figures 5.14 and 5.15.

5.3.2.2 Magnetisation.

The magnetisation data for each principal axis at the temperatures 2, 3, 5 and 10 K, in the field range 1 T to 7 T, are presented in Figures 5.16 – 5.18. Figure 5.16 is the magnetisation along the **a** axis at these 4 temperatures. As in the polycrystalline data, the four temperatures are in different phases, or close to the transition temperature, of NdNiSn.

The inset to Figure 5.16 shows the data at T = 2 K (AF phase) more clearly. At all temperatures the magnetisation increases smoothly and linearly up to 1 T. As is very clear in the insert, the 2 K data shows a peak at 1.5 T, before increases steadily to 3 T, where the magnetisation begins to saturate. At 7 T, the full moment is approximately $1.70\mu_B$/Nd-ion. The peak at 1.5 T may be interpreted as a metamagnetic transition at this field along the **a** axis. The T = 3 K curve does not show this transition at all, but does saturate just below the saturation moment of T = 2 K at about $1.67\mu_B$/Nd-ion (at H = 7 T). At T = 5 K the magnetisation follows a linear response up to 3.5 T, before showing a curved increase. The 10 K data has a linear increase up to 7 T, as expected in the paramagnetic regime.

Along the **b** axis [Figure 5.17] the T = 2 K (AF regime) data has a clear spin flop transition at H = 0.85 T and saturates at H = 7 T with a moment of $1.92\mu_B$/Nd-ion. The transition is also evident in the $T = T_N$ data, but is not as sharp. The saturation moment at H = 7 T is very close to the same value, as is the T = 5 K saturation at this point. The curve to the 5 K (paramagnetic phase) data does not show the spin flop transition, as expected, but has a linear response up to H = 1.5 T before curving to the saturation moment.

Of all the axes, **c** shows the smallest magnetisation at any temperature and field [Figure 5.18]. The T = 3, 5 & 10 K data all show a linear response up to H = 7 T, with a moment of $0.59\mu_B$/Nd-ion at H = 7 T, T = 3 K. In the AF phase (T = 2 K) however, there is a metamagnetic transition at H = 4.5 T. Up to H = 4 T the response is linear, and after the transition the data follows a curve up to a moment of $0.65\mu_B$/Nd-ion at H = 7 T.

The different response of each principal axis in the AF phase is quite interesting. Figure 5.19 depicts each axis at T = 2 K, allowing us to see the three transitions at H = 0.85 T (**b** axis), H = 1.5 T (**a** axis) and H = 4.5 T (**c** axis). What is also very clear is the size of the moment at H = 7 T for the three axes: $\mu_b \approx 1.1\mu_a$ and $\approx 3\mu_c$. Comparing this to the anisotropy at H = 0.03 T, the anisotropy has decreased by a factor of approximately 1/3.

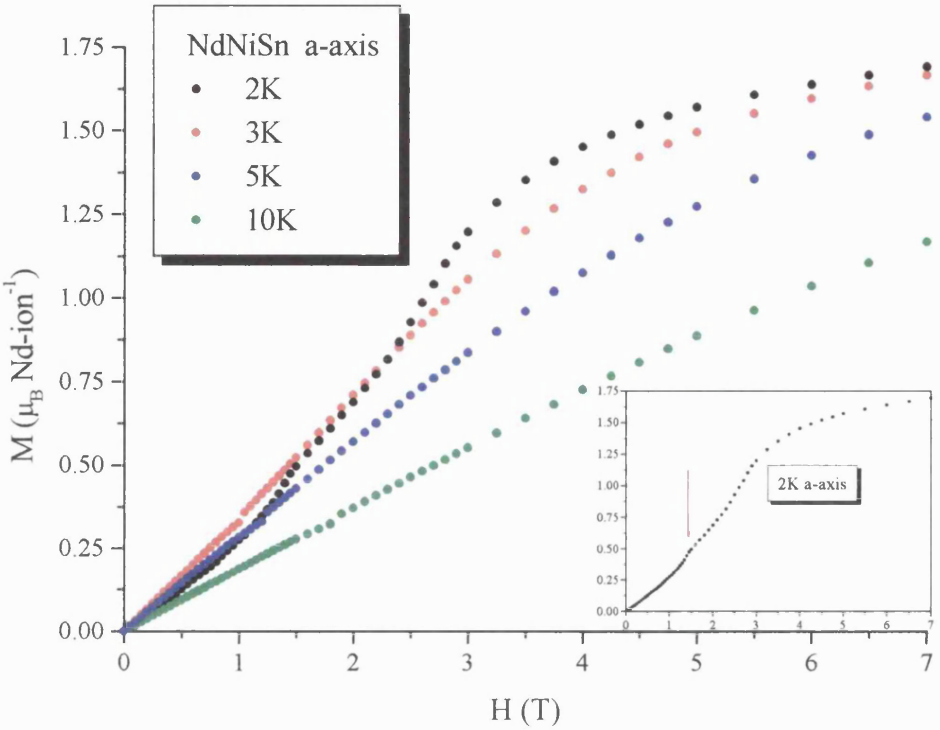

Figure 5.16: Field dependence of the magnetisation of polycrystalline NdNiSn along the **a** axis at 4 different temperatures. The inset shows the M v H data at T = 2 K (in the AF state) more clearly, with the red arrow indicating the possible transition at 1.5 T.

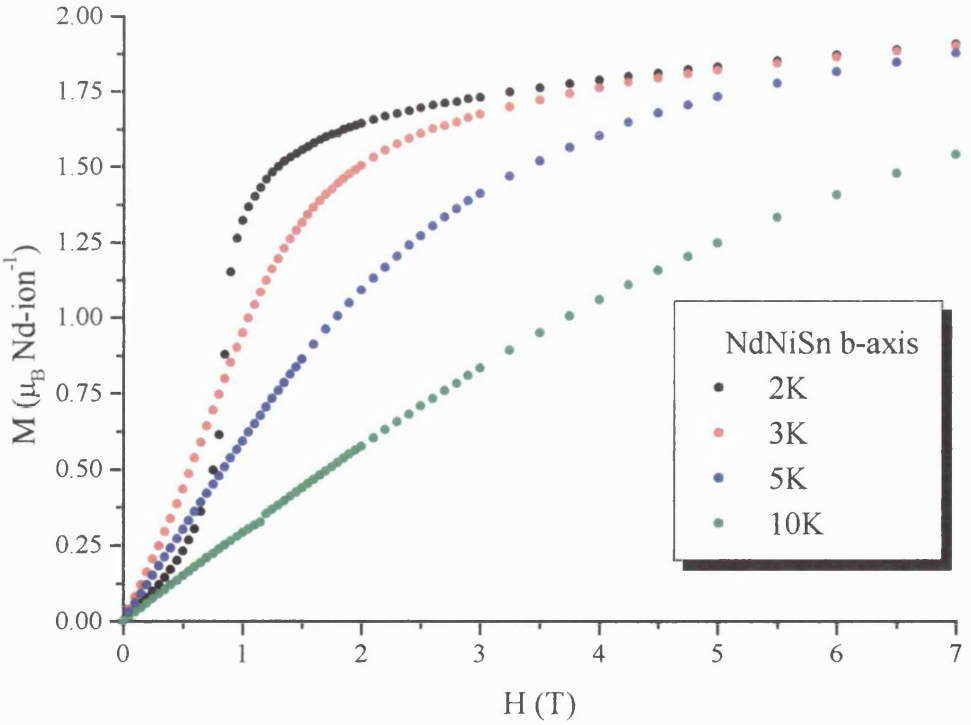

Figure 5.17: Field dependence of the magnetisation of polycrystalline NdNiSn along the **b** axis at 4 different temperatures. In the AF state (T = 2 K) a spin-flip transition is seen at 0.85 T.

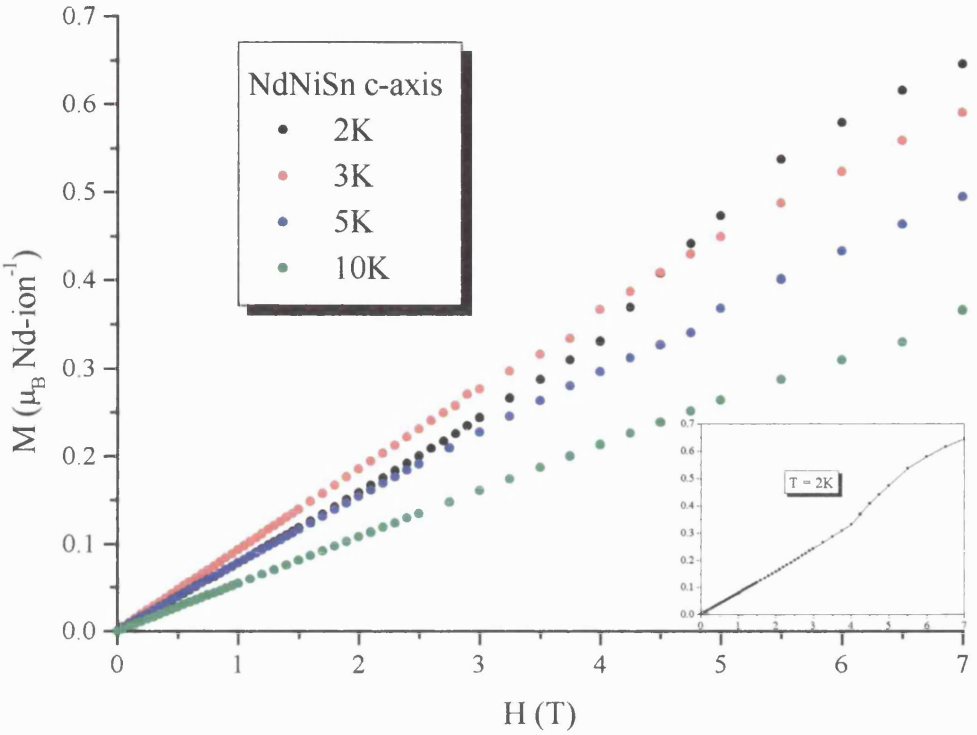

Figure 5.18: Field dependence of the magnetisation of polycrystalline NdNiSn along the **c** axis at 4 different temperatures. Note the small change between 4 T and 5 T that causes the 2 K data to cross the 3 K.

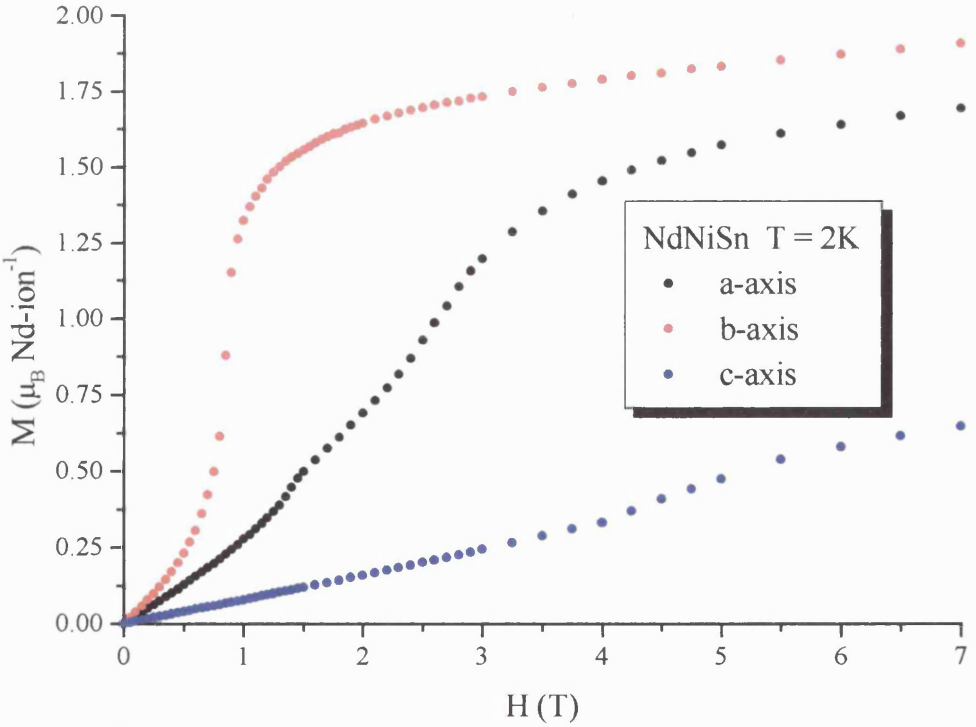

Figure 5.19: Field dependence of the magnetisation of polycrystalline NdNiSn along each principal axis at T = 2 K (AF state). The spin-flip transition in the **b** axis (0.85 T), and the steps at 1.5 T (**a** axis) and 4.5 T (**c** axis) are clearly shown.

CHAPTER 6

Conclusion and further work.

6.1 Summary.

The structural and magnetic properties of PrNiSn and NdNiSn have been investigated using a variety of techniques. Within this thesis, the first results of the single crystal inelastic neutron scattering data for both PrNiSn and NdNiSn have been published, and the first detailed studies of the magnetisation for both samples. The key findings from this work may be summarised as follows:

1. No magnetic ordering is found down to T = 1.7 K for PrNiSn, and antiferromagnetic ordering is confirmed at T_N = 3.1 K for NdNiSn. The magnetic structure for NdNiSn could not be determined due to its complex nature.

2. The single crystal magnetic susceptibility for both compounds has been determined down to 2K, and the Curie Weiss temperatures and effective moments determined.

3. The E = 3.5 meV excitation seen in single crystal PrNiSn has 4 modes, corresponding to the 4 Pr ions in the unit cell.

4. From the analysis of the data detailed in Chapters 4 and 5, I propose the levels schemes depicted in Figures 6.1 and 6.2 for paramagnetic PrNiSn and NdNiSn respectively.

The level scheme for PrNiSn has been determined using FOCUS to fit to the inelastic neutron scattering data from HET, and comparing the magnetic susceptibility calculated from the generated CEF parameters to the SQUID data. The wave function for each level is also proposed.

The level scheme for NdNiSn has been proposed directly from the observed peaks in the HET data. It was attempted by the author to analyse the HET data using the FOCUS program, but was not able to produce a level scheme in the available time. Two methods were tried for the starting CEF parameters of NdNiSn: (a) the CEF parameters for PrNiSn from Method 2 were used to produce starting parameters for NdNiSn, by converting using the Stevens Factors (as detailed in Section 4.2.5.1) and (b) starting values from the susceptibility data were calculated.

When these values were inputted into FOCUS, the two lowest excitations seen in the HET data could be fitted to extremely well. However, FOCUS found it very difficult to fit to the two highest excitations, due to their intensities, and tended to place the two excitations higher than observed. Given more time, and perhaps better statistics, a good fit maybe produced.

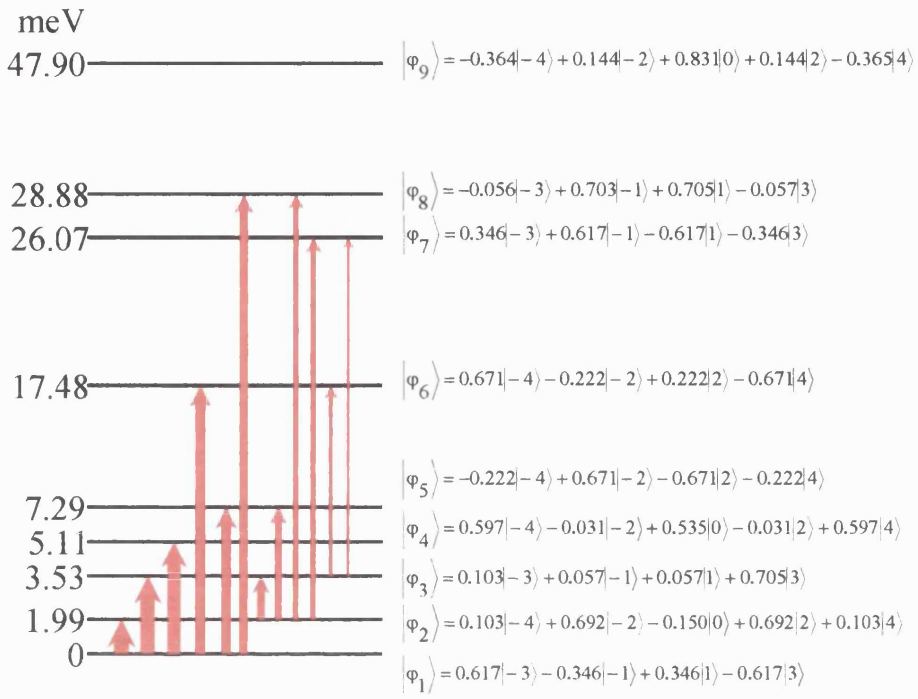

Figure 6.1: The proposed level scheme and wave functions for each level for PrNiSn, proposed Method 2.

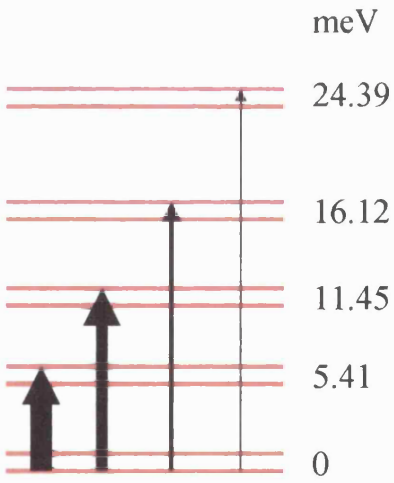

Figure 6.2: The proposed level scheme for NdNiSn, with approximate intensities depicted by arrow width. The scheme is proposed from the excitations observed in the HET experiment.

6.2 Further Work on PrNiSn and NdNiSn.

There is still much to be done for these two compounds. For PrNiSn, the single crystal specific heat and resistivity must be determined. From the program written by J. Allen, I have predicted the specific heat using the level scheme proposed in this work [Figure 6.3]. The experimental data may then be compared to the predicted data.

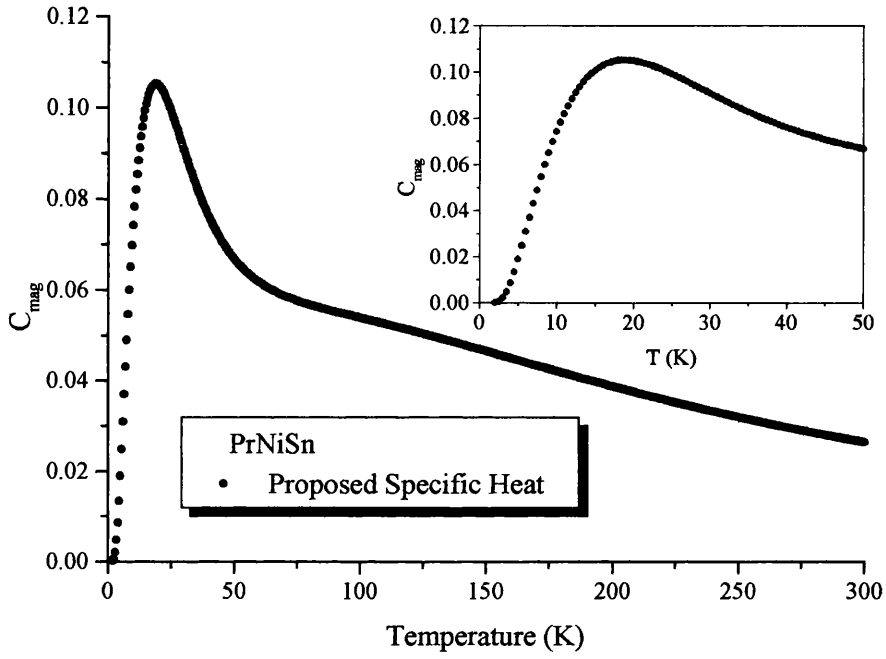

Figure 6.3: Proposed specific heat v temperature for PrNiSn, using the Fortran program written by J. Allen, to be published. The y axis is in arbitrary units.

The magnetic excitations seen in the PrNiSn single crystal must also be investigated under an applied field. The change in the energy levels and their intensity will give a good indication as to the validity of the proposed level scheme. Putting a compound under a field in this way is a sensitive test on the proposed wavefunctions

The question also remains as to how close to magnetic ordering PrNiSn is. A series of experiments should be set up to look at the properties of the series $(Pr_{1-x}Nd_x)NiSn$. This is possible because the crystal structures of both compounds are identical, so no changes in structure should be seen. The introduction of Nd with J = 9/2 should force the compound to order, pushing T_N into an accessible region.

On a similar vein, a pressure experiment could be carried out to look for the same effect. Because introducing Nd on the Pr may introduce disorder, placing PrNiSn under pressure should produce the same effect without any disorder occurring. This is because the lattice parameters of NdNiSn are smaller than PrNiSn, due to the Lanthanide contraction effect.

Further analysis needs to be carried out on NdNiSn to determine the crystal field parameters and level wavefunctions, as has been done for PrNiSn. This must then be used to calculate the magnetic susceptibility and compared to the data. The single crystal that has been used for the experiments detailed in this work was found to contain several crystallites. A better quality crystal needs to be used to investigate the magnetic excitations in a triple axis spectrometer, such as V2. The $4f$ level scheme may then be investigated in detail above T_N and below T_N. Splitting of the doublets below T_N should be observed, along with any spin wave excitations. Placing the crystal under an applied field will also split the doublets, and would be a test of the validity of any wavefunctions calculated for each level.

The crystal structure of NdNiSn needs to be determined using a good single crystal, perhaps on D10 at ILL. Beam time for this experiment was requested, but not given.

6.3 Further work in general.

There is still a lot of work to be carried out for CeNiSn, but the results we have achieved through this work may be of benefit to understanding CeNiSn. As is very clear from the HET experiment, the crystal field excitations for PrNiSn are well defined. As far as the author determined, no experiment has been carried out, apart from $(Ce_{1-x}La_x)NiSn$, where the Ce ion is doped with another Lanthanide. Again, this is feasible because the structures of CeNiSn and PrNiSn are the same, so no structural changes should be evident. Given that the lifetimes of the crystal field excitations for PrNiSn are small, but for CeNiSn the widths are very broad, doping the Ce site with Pr may reduce the width of the CEF excitations for CeNiSn.

References

- Abazawa, T, *et al,* Physica B **223-224** (1996) 218-221
- Adroja, D T, *et al,* Physica B **223-224** (1996) 275-278
- Adroja, D T, *et al,* Physica B **253** (1998) 269-277
- Adroja, D, *et al,* Physica B **253** (1998) 269-277
- Ahmet, P, *et al,* J. Phys. Soc. Jpn. **65** (1996) 1077-1082
- Akazawa T, *et al,* J Phys. Soc. Japan **67** (1998) 3256-3260
- Akazawa T, *et al,* Physica B. **259-261** (1999) 248-249
- Akazawa, T *et al,* J Phys. Soc. Japan **65** (1996) 3661-3665
- Akazawa, T, *et al,* Physica B **259-261** (1999) 248-249
- Aliev, F G, *et al,* J Mag. Mag. Mat. **76-77** (1988) 295-296
- Andoh, Y *et al,* Physica B **237-238** (1997) 575-576
- Andoh, Y, *et al,* J. Mag. Mag. Mat. **177-181** (1998) 1063-1064
- Aoki, Y *et al,* J Mag. Mag. Mat. **90-91** (1990) 496-498
- Aoki, Y *et al,* Phys. Rev. B **47** (1993) 15060-15067
- Bando, Y, *et al,* Physica B **194-196** (1994) 1179-1180
- Baran, S, *et al,* J. Phys, Condens. Matter **10** (1998) 2107-2114
- Baran, S, *et al,* J. Phys. Condens. Matter **8** (1996) 8397-8405
- Bonville, P, *et al,* Physica B **182** (1992) 105-117
- Boothroyd, A T, *et al,* Phys. Rev. Lett. **86** (2001) 2082-2085
- Bull, M *et al,* Phys. Rev. **57** (1998) 3850-3862
- Chevalier, B, *et al,* Physica B **226** (1996) 283-292
- Cox, D and Jarrell, M, J. Phys. Condens. Matter **8** (1996) 9825-9853
- D'Onfofrio, L D, *et al,* Physica B **171** (1991) 266-268
- Dwight, A E, *et al,* J. Less. Comm. Metals **93** (1983) 411
- Ellerby, M *et al,* J Phys Condens. Matter **13** (2001) 4221-4238
- Fujita, T *et al,* Physica B **246-247** (1998) 445-447
- Fujita, T, *et al,* J Mag. Mag. Mat. **108** (1992) 35-39
- Fujji, H *et al,* J Phys. Soc. Japan **58** (1989) 2495-2500
- Fujji, H *et al,* Physica B. **192** (1993) 219-227

- Furusawa, M, *et al,* J. Mag. Mag. Mat. **140-144** (1995) 877-878
- Gratz, E, *et al,* J. Phys. Condens. Matter **43** (1991) 9297
- Gulay, L D, and Hiebl, K, J. Alloys Comp. **339** (2002) 46-53
- Gulay, L D, *et al,* J. Alloys Comp. **313** (2000) 42-46
- Hashimoto, Y, *et al,* J. Phys. Soc. Jpn. **47** (1979) 73-76
- Hashimoto,Y, *et al,* J. Phys. Soc. Jpn. **47** (1979) 67-72
- Hicks, T J, Aust. J. Phys. **50** (1997) 1119-1126
- Hidenobu, H *et al,* Phys. Lett. A **224** (1997) 293-297
- Hiroaki, I, Physica B **281-282** (2000) 183-184
- Houmann, J G *et al,* Phys. Rev. B **20** (1979) 1105-1118
- Inada, Y, *et al,* J Phys. Soc. Japan **65** (1996) 1158-1161
- Isoda, M and Takahashi Y, J. Phys. Soc. Japan **66** (1997) 3224-3230
- Isoda, M *et al,* J Mag. Mag. Mat. **140-144** (1995) 1385-1386
- Jensen, J and Mackintosh, A R, **Rare Earth Magnetism** Oxford Press (1991)
- Kagan, Y, *et al,* Phys. Rev. B **55** (1997) 12348-1161
- Kalvius, G M, *et al,* Physica B **186-188** (1993) 412-415
- Karla, I, *et al,* Physica B **253** (1998) 215-221
- Karla, I, *et al,* Physica B **271** (1999) 294-303
- Kasaya, M, *et al,* J. Phys. Soc. Japan **60** (1991) 2542-2545
- Kasaya, M, *et al,* J. Mag. Mag. Mat. **104-107** (1992) 665-666
- Kasaya, M, *et al,* J. Phys. Soc. Japan **60** (1991) 3145-3149
- Kasaya, M, *et al,* J. Phys. Soc. Japan **61** (1992) 4187-4192
- Katsuhiko, T and Kasuya, T, Solid State Communications **74** (1990) 243-248
- Kawano, S, *et al,* J. Mag. Mag. Mat. **182** (1998) 393-395
- Kaysuya, T, Prog. Theor. Phys. **16** (1956) 45
- Koghi, M, *et al,* Physica B **186-188** (1993) 409-411
- Koghi, M, *et al,* J Mag. Mag. Mat. **108** (1992) 187-189
- Kolenda, M, *et al,* J. Alloys Comp. **269** (1998) 25-28
- Kotsanidis, P A, *et al,* J. Mag. Mag. Mat. **124** (1993) 51-54
- Kotsanidis, P A, *et al,* J. Mag. Mag. Mat. **131** (1994) 139-147
- Kurisu, M, *et al,* Physica B **201** (1994) 107

- Lebech, B, *et al,* J. Mag. Mag. Mat. **70** (1987) 97-101
- Lebech, B, Physica B **318** (2002) 251-260
- Mähl, S, *et al,* Phys. Rev. B **56** (1997) 7245-7254
- Malik, S K, and Adroja, D T, J. Mag. Mag. Mat. **102** (1991) 42-46
- Malik, S K, *et al,* J. Alloys Comp. **207-208** (1994) 237-240
- Manon, L and Malik, S K, Phys. Rev. B **55** (1997) 14100-14102
- McCusker, L B, *et al,* J. Appl. Cryst. **32** (1999) 36-50
- McEwen, K *et al,* Physica B **281-282** (2000) 600-601
- McEwen, K, *et al,* J. Phys. Soc. Jpn. **70** (2001) 18-21
- Misawa, S, J Mag. Mag. Mat. 177**-181** (1988) 325-326
- Moreno, J and Coleman, P, Phys. Rev. Lett. **84** (2000) 342-345
- Moze, O **Handbook of Magnetic Materials Volume II** (1998) 493-624
- Mukhin, A A, *et al,* J Mag. Mag. Mat. **226-230** (2001) 1139-1141
- Noce, E *et al,* Europhys. Lett. **51** (2000) 195-201
- Nowotny, H and Zajac, Š, Physica B **130** (1985) 228-230
- Oki, A, *et al,* J. Mag. Mag. Mat. **171-181** (1998) 1089-1090
- Oppeneer, P M, *et al,* Phys. Rev. B **54** (1996) 3706-3709
- Palstra, T T M, *et al,* J Mag. Mag. Mat. **67** (1987) 331-342
- Park, J G, *et al,* Phys. Rev. B **58** (1998) 3167-3171
- Paschen, S, *et al,* Phys. Rev. B **62** (2000) 14912-14919
- Pierre, J and Karla, I J. Mag. Mag. Mat. **217** (2000) 74-82
- Prots' Y M, *et al,* J. Solid State Chemistry **142** (1999) 400-408
- Reiffers, M *et al,* Solid State Communications **103** (1997) 179-183
- Reitveld, H M, J Appl. Cryst. **2** (1969) 65-71
- Riseborough, P, Physica B **246-247** (1998) 378-381
- Rodriguez-Carvajal, J Physica B. **192** (1993) 55-69
- Rossi, D *et al,* J. Less-Common Metals **107** (1985) 99-104
- Routsi, Ch. D, and Yakinthos, J K, J. Mag. Mag. Mat. **110** (1992b) 317-322
- Routsi, Ch. D, and Yakinthos, J K, J. Mag. Mag. Mat. **117** (1992a) 79-82
- Routsi, Ch. D, *et al,* J. Mag. Mag. Mat. **98** (1991) 257-260
- Ruderman, M A. and Kittel, C, Phys. Rev. **96** (1954) 94

- Sakurai, J, *et al,* J. Mag. Mag. Mat. **140-144** (1995) 875-876
- Shannon, N, J. Phys. Condens. Matter **13** (2001) 6371-6386
- Shohata N, J. Phys. Soc. Japan **42** (1977) 1873-1880
- Stunault, A, *et al,* J. Mag. Mag. Mat. **226-230** (2001) 1116-1117
- Sugiyama, K *et al,* J Mag. Mag. Mat. **226-230** (2001) 142-144
- Suzuki, T *et al,* Physica B **199-200** (1994) 483-485
- Szytula, A, *et al,* J. Alloys Comp. **259** (1997) 36-41
- Szytula, A, *et al,* J. Mag. Mag. Mat. **222** (2000) 47-53
- Szytula, A, Solid State Phenomena **61-62** (1998) 27-36
- Takabatake, T, *et al,* Phys. Rev. B **41** (1990a) 9607-9610
- Takabatake, T, *et al,* Phys. Rev. B **59** (1999) 13878-13881
- Takabatake, T, *et al,* Physica B. **223-224** (1996) 413
- Takabatake, T, *et al,* J Phys. Soc. Japan **59** (1990b) 16-19
- Taylor, A D, *et al,* Phys. Rev. Letters **61** (1998) 1309-1312
- Terashima, T, *et al,* Physica B **294-295** (2001) 245-248
- Vettier, C, J Mag. Mag. Mat. **226-230** (2001) 1053-1057
- Watanabe, S and Kuramoto, Y, Z Phys B **104** (1997) 535-540
- Yakinthos, J K, and Routsi, Ch. J. Mag. Mag. Mat. **149** (1995) 273-278
- Yeresko, A N, *et al,* Physica B **230-232** (1997) 513-515
- Yethiraj, M *et al,* J Mag. Mag. Mat. **79** (1989) 355-357
- Yosida, K, Phys. Rev. **106** (1957) 893
- Yuen, T *et al,* Physica B **171** (1991) 362-366